A search for quantum gravity motivated decoherence in atmospheric neutrinos using IceCube DeepCore

M.Sc. project

Written by *Martin Langgård Ravn*

May 20, 2022

Supervised by
Thomas Simon Stuttard
D. Jason Koskinen

Niels Bohr Institute

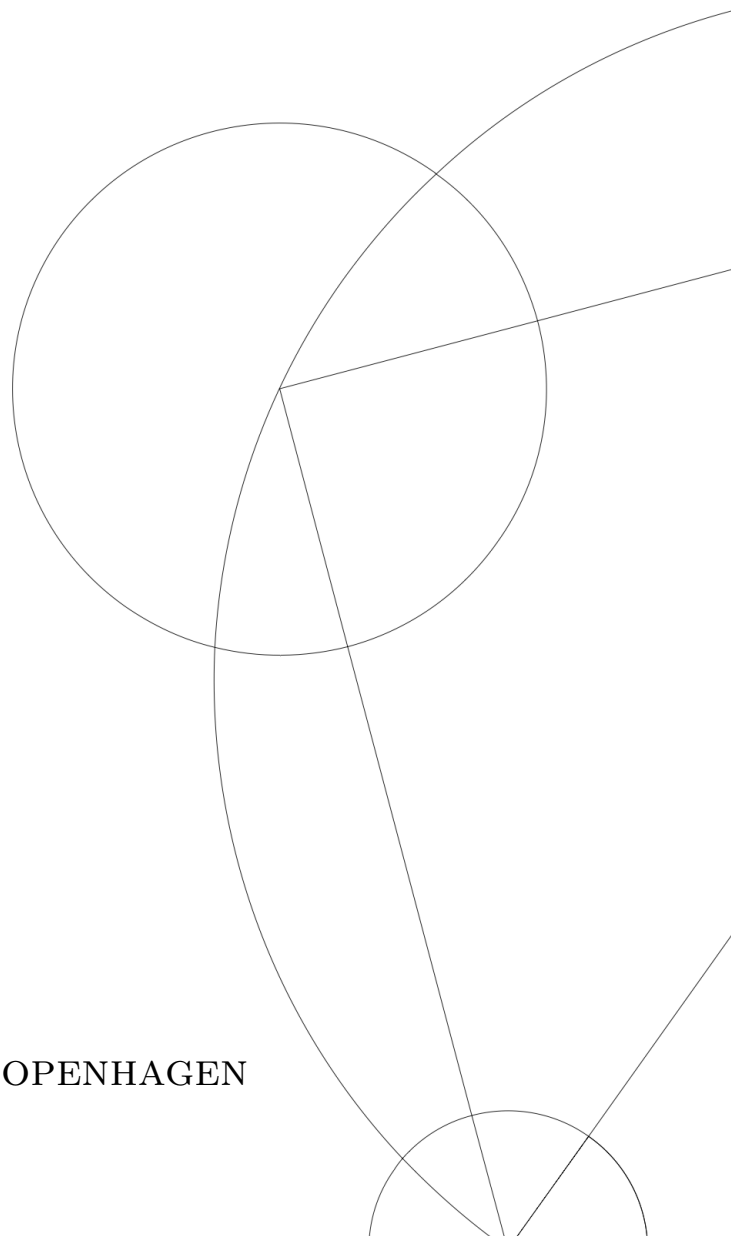

University of Copenhagen

Abstract

Quantum-mechanical phenomena and the force of gravity are each well-described by quantum field theory and general relativity, respectively. If however one attempts to formulate gravity as a quantum force, quantum field theory breaks down. As a result, a unified theory of quantum mechanics and gravity, called quantum gravity, is highly sought after in theoretical physics. Although we do not yet have an accepted theory of quantum gravity, some of its features can be predicted. One such prediction is that space-time fluctuates at tiny distances, perhaps even producing microscopic short-lived 'virtual' black holes. These effects are difficult to probe experimentally, because they are only expected to be large at energies and distances approaching the Planck scale. However, a promising candidate for where sensitivity to quantum gravity signals might be achievable is in neutrino oscillations. This is due to the long travel distances of neutrinos, where tiny perturbations to their propagation might have accumulated to a measurable signal as they reach a detector. Specifically, fluctuations of space-time and interactions with virtual black holes lead to loss of coherence and damping of neutrino oscillations.

In this project we search for such a signal in atmospheric neutrino data from the IceCube Neutrino Observatory. Recently developed phenomenological models of neutrino oscillations with lightcone fluctuations and virtual black hole interactions are implemented in the neutrino propagation code nuSQuIDS. Furthermore, the models are included in a `python` statistics framework named PISA, used for analyzing IceCube data. This allows us to carry out a statistical analysis of an IceCube DeepCore data sample. The analyzed data is called the oscNext sample, which is a high statistics sample of $\mathcal{O}$(10-300 GeV) atmospheric neutrinos recorded during 9.3 years of detector livetime. The sensitivity of the oscNext sample to the considered models is found and compared to both 'natural' Planck scale expectations and bounds set by previous studies of decoherence using neutrinos. We find that the oscNext sample is sensitive to natural Planck scale expectations of virtual black hole scenarios for the energy-dependence power-law index of $n < 2.58$ at 90% confidence. Together with a planned analysis using IceCube, this will be the most sensitive measurement to date on neutrino decoherence resulting from quantum gravity effects.

Acknowledgments

I have been very happy with the last nine months I have spent as a master student in the IceCube group at NBI. The entire group has always always been welcoming and helpful, and I have enjoyed working here on a day-to-day basis. I feel privileged for having had this opportunity.

I would like to thank my supervisors, Jason and Tom, for making this project possible, always pushing me to do my best, and having plenty of confidence in me. I appreciate that Tom has let me work on a topic as fascinating and difficult as this, and providing me with plenty of useful help and feedback. I also specifically want to thank Jason for encouraging me to present my project at the 1st Annual NBI MSc. Student Symposium in front of 150 fellow students and scientists. That is an experience I will not forget soon.

I also want to thank my office mates, Kevin and Marc, for keeping me company during many long workdays. The last nine months would not have been the same without you. Additionally, I have been happy to have great next door office mates, James, Kaare, Leon, and Tania, who have given me a social life that extents beyond my own office.

Finally, I want to thank Marie for always being there when I need you.

Author's contribution

The main part of the work presented in this thesis is the development of the oscNext decoherence analysis, which is an IceCube collaboration analysis. To work on the analysis I bacame part of the IceCube collaboration in August 2021, and has developed this analysis during my MSc. project.

Prior to this project, the ν-VBH interaction models were implemented in `nuSQuIDS` by Tom Stuttard. I have used this code as a framework to implement the lightcone fluctuation models in `nuSQuIDS` as described in Section 4.2, which currently work in vacuum. In matter however, unexpected challenges have arisen, which have been outlined but not yet solved. Additionally, many robustness tests have been carried out in Section 4.3 to verify that the `nuSQuIDS` calculations agree with the simulations.

Similarly, the `nuSQuIDS` implementation of the ν-VBH state selected model was integrated in PISA already. The other ν-VBH and lightcone fluctuation models were however added by me, which is described in Section 5.2 and allows us to perform statistical analyses using them.

An important part of the analysis is the minimizer used to fit the models and all of the nuisance parameters to the data. A considerable amount of work went into finding a robust minimizer strategy with good stability, high precision, and a manageable runtime. This is shown in Section 5.8.

I have developed the oscNext decoherence analysis to include the new models in a way that makes it easy to run various statistical tests in PISA for any combination of model and parameters. In section 5.10 and onwards, this was used to calculate the sensitivity of the oscNext sample to five different models and many values of the energy-dependence parameter, n. Additionally, the results have been thoroughly compared to both Planck scale expectations and previous studies of decoherence with neutrinos in Section 6. The oscNext decoherence analysis is now almost ready to be applied to real data.

Contents

1 Introduction

Finding a unified theory of quantum mechanics and gravity is one of the most fundamental problems in theoretical physics remaining to be solved. Both of these fields are well-understood on their own and can be described by separate theories. The underlying theories; quantum field theory and general relativity, are however not compatible with each other and provide conflicting results. They are for instance unable to explain the center of a black hole or the early universe. Furthermore, gravity, as described by general relativity, can not be formulated as a force in quantum field theory. This is a clear indication that there is more to the fundamental laws of the universe than just these two theories. Despite many years of research, no complete theory describing both quantum mechanics and gravity has been put forth. The field of research that seeks to unify these theories is called quantum gravity.

Even though no complete and accepted theory exists, some general behavior of quantum gravity is expected, and certain effects are predicted by many different quantum gravity models. One main prediction is that space-time itself adheres to Heisenberg's uncertainty principle, causing its curvature to fluctuate [1, 2, 3, 4, 5]. The scale at which this takes place is at microscopic distances approaching the Planck length ($L_{\text{Planck}} = 1.6 \times 10^{-35}$ m) or at extreme energies approaching the Planck energy ($E_{\text{Planck}} = 1.2 \times 10^{19}$ GeV), collectively called the Planck scale. The fluctuations of space-time results in an intrinsic uncertainty in travel distances, times, and velocities of particles traversing this medium. This is known as *lightcone fluctuations* [6, 7]. In addition, if the fluctuations of space-time are extreme enough, the space-time itself can collapse into a singularity. This creates a microscopic black hole [8, 9] which almost immediately evaporates via Hawking radiation. Since such black holes are created in quantum fluctuations, and only exist temporarily violating conservation of energy, they are often referred to as *virtual black holes* (VBH). They can be thought of as a quantum gravity equivalent of the electron-positron pairs in quantum electrodynamics responsible for the phenomenon known as vacuum polarisation. This means that everywhere in space a sea of VBHs exist that other types of particles can interact with if they couple to the VBHs. The question is then if particles far below the Planck scale experience the effects of both lightcone fluctuations and VBHs.

Both lightcone fluctuations and the exisistence of VBHs can in principle be tested experimentally. The energies and distances at which these effects are expected to be strong are however far out of reach of any current experiment. At lower energies and larger distances such effects are expected to be heavily supressed, and they can thus not be measured directly. If however a quantum gravity effect is allowed to accumulate, a measurable signal might be achieved. Quantum gravity predictions are thus ideally searched for in places where the given effects have had time to build up.

A promising candidate to test for quantum gravity phenomena is the neutrino. Neutrinos couple only extremely weakly to other particles, allowing neutrinos to travel far without interacting with anything. They thus evolve as pure quantum states over large distances. consequently, neutrinos are generally considered to evolve coherently, meaning that the wavefunctions of neutrinos traveling the same path evolve identically. One consequence of the quantum nature of neutrinos at macroscopic distances is neutrino oscillations, i.e. the flavor of a neutrino changing as it propagates [10, 11, 12]. Neu-

trino oscillations arise from the fact that neutrinos propagate as superpositions of several underlying mass states, adding a time dependence to the superposition of the neutrino states. To experimentally observe this phenomenon, it is necessary that the superposition principle is upheld over the entire travel distance. Additionally, neutrinos emitted from the same source must have oscillated equally when they are observed. However, if neutrinos are actually coupled to their environment, for instance if they interact with VBHs; or the medium they travel in behaves stochastically, like with lightcone fluctuations, coherence is lost during travel. This is called decoherence and ultimately leads to damping of neutrino oscillations [13, 14], which can be searched for experimentally. Because of the long travel distances of neutrinos (atmospheric, galactic or even cosmological baselines), these otherwise small effects can accumulate into sizable signals, once they have reached a detector. Hence, the neutrino is an ideal candidate to search for a signal like this.

In this project, we test three neutrino-virtual black hole (ν-VBH) interaction scenarios which are as described in [13] and lightcone fluctuations models described in [14]. Their impact on neutrino oscillations are investigated through simulations and corresponding analytical formulations are implemented in numerical calculations of neutrino oscillations. The implementations are employed to perform a full statistical analysis to estimate the sensitivities of an IceCube DeepCore dataset called the oscNext sample. Previous decoherence studies have used very general formulations, which makes it difficult to connect the results to underlying models. The phenomenology used in our analysis however, makes it possible to interpret the results to directly constrain parameters of heuristic quantum gravity scenarios. In addition to this, we compare the sensitivity of the oscNext sample to constraints of decoherence parameters found in previous neutrino studies.

Natural units are used in this project, except when explicitly stated otherwise. Specifically, we choose the reduced Planck constant, $\hbar$, and the speed of light, c, to be equal to one, i.e. $\hbar = c = 1$. This allows us to omit these constants from mathematical expressions and formulate them more concisely.

2 Neutrino phenomenology and detection

2.1 The Standard Model and neutrinos

The Standard Model describes the smallest constituents of the universe and their interactions. It is depicted in Figure 1. The particles of the model are divided into three main types; fermions, which constitutes the matter of the universe, gauge bosons, which carry the forces between the fermions, and the Higgs scalar boson, which is responsible for the mass of the particles. The three forces of the Standard Model are the electromagnetic force, carried by the photon, the strong force, carried by the gluon, and the weak force, carried by the W and Z bosons. The fermions are further divided into two subcategories; the quarks and the leptons, where mainly the latter are of interest in this project. The leptons consist of three electrically charged particles with three different flavors; the electron, the muon, and the tauon, and the corresponding neutrally charged leptons; the neutrinos. In addition to this, corresponding antiparticles to all of the aforementioned particles exist.

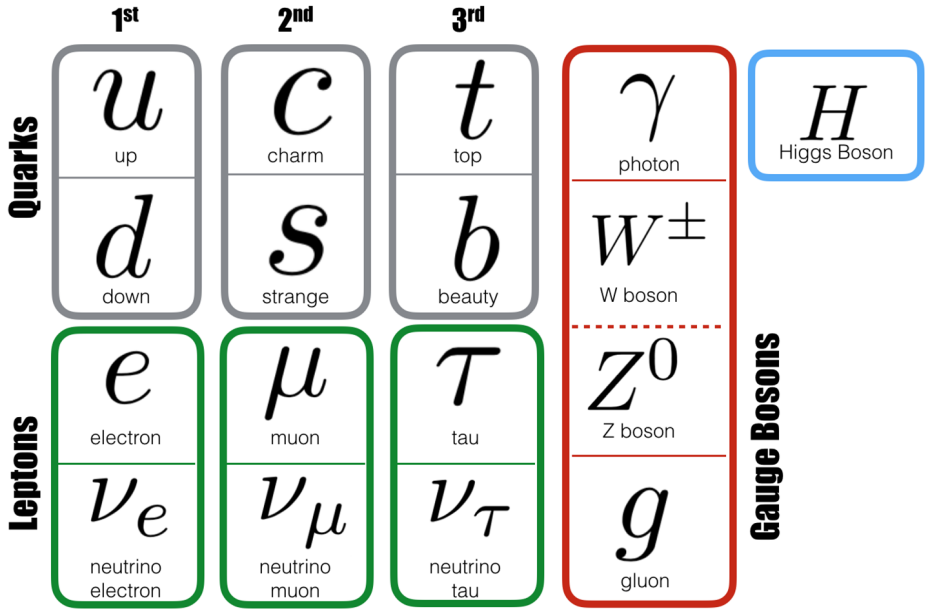

FIGURE 1: The particles of the Standard model [15].

The main focus of this project is the neutrino. Three generations of neutrinos exist; the electron neutrino (ν_e), the muon neutrino (ν_μ), and the tau neutrino (ν_τ). In the Standard Model, they are assumed to be massless [16]. However, due to the observation of neutrino oscillations the neutrino masses must be non-zero, although tiny (see Section 2.2).

Neutrinos have no color charge, and thus they do not interact with the strong force. In addition to this, they are electrically neutral and do not couple to the electromagnetic force. The only force they can interact with is the weak force, which couples to the flavor of the fermions. The weak force is strongly suppressed at long distances, and thus

it is in general orders of magnitude weaker than the electromagnetic and strong force. This means that neutrinos interact only very rarely with other particles, which allows for long travel distances. In low density environments, like intergalactic space, they can propagate more or less indefinitely, resulting in cosmological baselines. Even inside matter they travel almost freely. Thus neutrinos can traverse through the Earth with only a small probability of interacting.

Many different sources of neutrinos exist. Nuclear reactors based on β decay produce low-energy electron antineutrinos isotropically as a by-product. Detectors can then be stationed close to the reactors and observe the emitted neutrinos and probe particle physics theories [17, 18, 19]. It is also possible to create neutrino beams, and thus accelerator experiments can be set up [20, 21, 22]. A typical energy range of such experiments is 0.5 GeV to 10 GeV and the neutrinos can reach travel distances of up to several hundred kilometers [23]. Even longer baselines can be reached by neutrinos produced in the atmosphere and observed in neutrino observatories. These neutrinos are the focus of this project and are elaborated on in Section 2.4. The Sun also produces a large amount of electron neutrinos through fusion processes which can be detected on the Earth. These have been extensively researched in the past. The final major category of neutrino sources is astrophysical sources. These include supernovae, active galactic nuclei, gamma-ray bursts, binary star mergers and more [24], which could emit neutrinos through many different processes. Neutrinos observed from such sources provide vital information about the sources themselves and are especially important from an astrophysical perspective.

2.2 Neutrino oscillations

An important attribute of neutrinos is that their flavors change as they travel through space [10]. Thus a neutrino emitted as one flavor can later be observed as any other flavor. This is a quantum-mechanical phenomenon known as neutrino oscillations and is caused by mixing between the weak and mass eigenstates of neutrinos. Consequently, the neutrino states which participate in weak interactions are not the same as the mass states. Instead, the three weak (also called flavor) eigenstates, ν_e, ν_μ, and ν_τ, are different superpositions of three mass eigenstates, ν_1, ν_2, and ν_3. The flavor and mass eigenstates can be seen as two different bases and any neutrino state can be expressed in either one of these. A unitary transformation between the two bases can be expressed via a 3x3 matrix called the Pontecorvo–Maki–Nakagawa–Sakata (PMNS) [25] matrix

$$\begin{pmatrix} \nu_e \\ \nu_\mu \\ \nu_\tau \end{pmatrix} = \begin{pmatrix} U_{e1} & U_{e2} & U_{e3} \\ U_{\mu 1} & U_{\mu 2} & U_{\mu 3} \\ U_{\tau 1} & U_{\tau 2} & U_{\tau 3} \end{pmatrix} \begin{pmatrix} \nu_1 \\ \nu_2 \\ \nu_3 \end{pmatrix}. \tag{1}$$

The PMNS matrix describes the relation between the flavor and mass eigenstates. For instance, the three matrix elements squared $|U_{e1}|^2$, $|U_{e2}|^2$, and $|U_{e3}|^2$, parameterize how much of each mass state constitutes an electron neutrino. A neutrino state which starts as any of the three flavors, denoted α, at $t = 0$ can be expressed as:

$$|\nu_\alpha, 0\rangle = \sum_j U^*_{\alpha j} |\nu_j, 0\rangle, \tag{2}$$

where j can take the values 1, 2, and 3 which refer to the three mass eigenstates. To inspect how this state evolves, the time evolution operator e^{-iHt} is applied:

$$|\nu, t\rangle = \sum_j U^*_{\alpha j} e^{-iHt} |\nu_j, 0\rangle. \tag{3}$$

In vacuum the Hamiltonian is diagonal in the mass basis with energy $E_j = \sqrt{p^2 + m_j^2}$. The time evolution of the state is then:

$$|\nu, t\rangle = \sum_j U_{\alpha j} e^{-i\sqrt{p^2+m_j^2}t} |\nu_j, 0\rangle. \tag{4}$$

From this expression it can be seen that each mass state constituting the flavor state at $t = 0$ propagates with a different phase, if their masses are different. This leads to the mass states going in and out of phase with each other as the neutrino propagates, and thus the composition of mass states of the neutrino changes. In turn, the flavor composition of the neutrino also changes, and thus a neutrino which is produced as one flavor can later be observed as a different flavor. The transition and survival probabilities of a neutrino can be derived by going to the highly relativistic limit (thus assuming $m_j \ll p$ and $t \approx L$), evolving the state in the mass basis, and projecting it onto the flavor basis via the PMNS matrix. The probability of af a neutrino transitioning from flavor α to β is:

$$P(\nu_\alpha \to \nu_\beta) = \delta_{\alpha\beta} - \sum_{i<j} \Re(U^*_{\alpha i} U_{\beta i} U_{\alpha j} U^*_{\beta j}) \sin^2\left(\frac{\Delta m^2_{ji} L^*}{4E}\right) \tag{5}$$

$$\begin{aligned} = \delta_{\alpha\beta} - 4\Bigg[& U^*_{\alpha 1} U_{\beta 1} U_{\alpha 2} U^*_{\beta 2} \sin^2\left(\frac{\Delta m^2_{21} L}{4E}\right) \\ & + U^*_{\alpha 1} U_{\beta 1} U_{\alpha 3} U^*_{\beta 3} \sin^2\left(\frac{\Delta m^2_{31} L}{4E}\right) \\ & + U^*_{\alpha 2} U_{\beta 2} U_{\alpha 3} U^*_{\beta 3} \sin^2\left(\frac{\Delta m^2_{32} L}{4E}\right)\Bigg], \end{aligned} \tag{6}$$

where $\Delta m^2_{ij} = m^2_j - m^2_i$ are the differences between the squared of the masses of the mass eigenstates states. From this expression it can be seen that the transition probabilities have oscillation like patterns with wavelengths defined by $\lambda_{ij} = 4\pi E/\Delta m^2_{ij}$ and magnitudes related to the matrix elements.

The PMNS matrix, as expressed in Equation 1, has many free parameters. They can however be reduced to only four by assuming unitarity. If the PMNS matrix is unitary, a neutrino state in one basis will transform to a state in the other basis with the same normalization, i.e. no neutrinos are lost or gained by changing basis. This is a reasonable assumption if there is no mixing of the known neutrinos with some yet unknown states. In this case, the PMNS matrix is just a rotation defined by three angles θ_{ij}, which parameterize the mixing between mass and flavor states, and a complex phase δ_{CP}, which allows for CP violation i.e. differences between neutrinos and antineutrinos.

The unitary PMNS matrix is by convention defined like this:

$$U_{\text{PMNS}} = \begin{pmatrix} c_{12}c_{13} & s_{12}c_{13} & s_{13}e^{-i\delta_{\text{CP}}} \\ -s_{12}c_{23} - c_{12}s_{23}s_{13}e^{i\delta_{\text{CP}}} & c_{12}c_{23} - s_{12}s_{23}s_{13}e^{i\delta_{CP}} & s_{23}c_{13} \\ s_{12}s_{23} - c_{12}c_{23}s_{13}e^{i\delta_{\text{CP}}} & -c_{12}s_{23} - s_{12}c_{23}s_{13}e^{i\delta_{CP}} & c_{23}c_{13} \end{pmatrix}, \tag{7}$$

where $s_{ij} = \sin\theta_{ij}$ and $c_{ij} = \cos\theta_{ij}$. With this parameterization, the oscillation amplitudes depend non-trivially on θ_{ij}.

The oscillation patterns are expected to extend indefinitely if neutrinos do not interact with their environment. This project however explores modifications to standard oscillations resulting from quantum gravity effects, which are applied to neutrinos produced in the atmosphere and detected in IceCube.

2.3 NuFit results

A large number of neutrino experiments are aimed at measuring the oscillation parameters. Different experiments are however optimized for specific parameters or only able to measure some of them. The most accurate estimations of the oscillation parameters are thus obtained from combining many different measurements in a global fit. One such analysis is named NuFit [26, 27], which will be used throughout this analysis. Specifically, we use the NuFit 4.0 (2018) results assuming normal mass ordering (i.e. $m_1 < m_2 < m_3$) with Super-Kamiokande atmospheric data included. These are shown in Table 1.

Parameter	Best fit
θ_{12} [°]	$33.82^{+0.78}_{-0.76}$
θ_{23} [°]	$49.7^{+0.9}_{-1.1}$
θ_{13} [°]	$8.61^{+0.12}_{-0.13}$
Δm_{12} [eV]	$7.39^{+0.21}_{-0.20} \times 10^{-5}$
$\Delta m_{23} \approx \Delta m_{13}$ [eV]	$2.525^{+0.033}_{-0.031} \times 10^{-3}$
δ_{CP} [°]	$217^{+0.40}_{-0.28}$

TABLE 1: NuFit results of oscillation parameters assuming normal mass ordering ($m_1 < m_2 < m_3$).

2.4 Atmospheric neutrino production

The Earth is constantly bombarded with particles from outer space. The most energetic of these are cosmic rays; primarily protons and atomic nuclei reaching Earth from our own and far away galaxies. When a cosmic ray enters the atmosphere, it quickly collides with the nucleus of an atom in an air molecule. This breaks the nucleus apart violently, producing many new, highly energetic particles in the process. Such an event is called a cascade. The heavy particles created in a cascade quickly decay to lighter stable particles., resulting in an air shower as shown in Figure 2. Specifically, a large number of pions are created in the initial cascade [28]. The main decay channels of charged pions, $\pi^{\pm}$, are

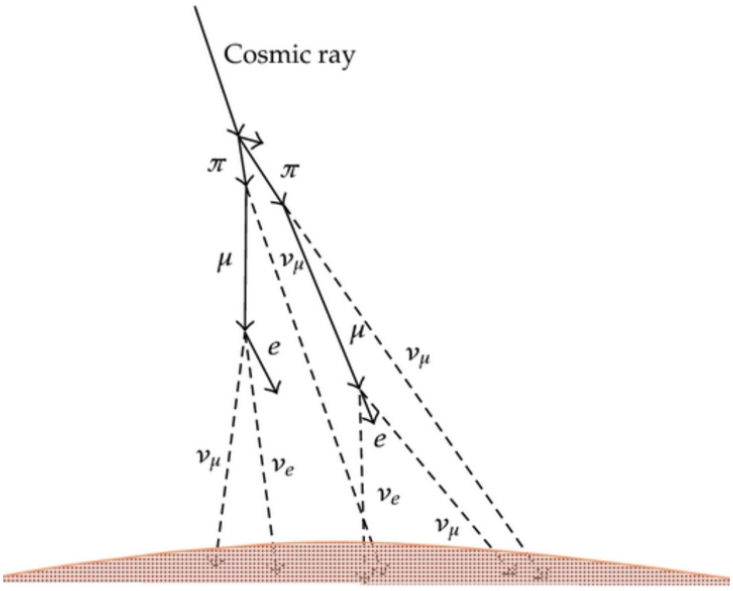

FIGURE 2: An illustration of an air shower caused by a cosmic ray [28].

$\pi^- \to \mu^- + \nu_\mu$ and $\pi^+ \to \mu^+ + \bar{\nu}_\mu$. Charged pions can also decay via the channels $\pi^- \to e^- + \bar{\nu}_e$ and $\pi^+ \to e^+ + \nu_e$, however this process happens only rarely due to helicity suppression [29].

The muons created in the charged pion decays are unstable and have a lifetime of ~ 2.2 μs [30]. If a muon has sufficiently high energy, it can reach a detector before it decays. In this case both a muon neutrino and a muon can be observed. This is especially likely to happen if they are created in the atmosphere directly above the detector, where the travel distance is short.

If however the muon decays before it reaches the detector, it can happen via two channels; $\mu^- \to e^- + \bar{\nu}_e + \nu_\mu$ and $\mu^+ \to e^+ + \nu_e + \bar{\nu}_\mu$. Adding these processes together with the neutrinos from the charged pion decay, we see that the flavor composition is roughly $\nu_e : \nu_\mu : \nu_\tau = 1 : 2 : 0$. We thus expect to observe a large number of both electron and muon neutrinos produced in the atmosphere.

The energy spectrum of atmospheric neutrino flux follows roughly a power-law, which decreases rapidly with energy.

2.5 Matter effects

The cross section of a neutrino interacting with any other particle is tiny. A neutrino produced in the atmosphere (or any other neutrino) can thus propagate more or less freely through the Earth. There is however a modification to how they oscillate in matter compared to vacuum [31]. Two types of neutrino interactions with charged leptons exist: neutral currents (NC) and charged currents (CC). Their Feynman diagrams are shown in Figure 3.

NC interactions are exchanges of a neutral Z boson and can happen for any neutrino

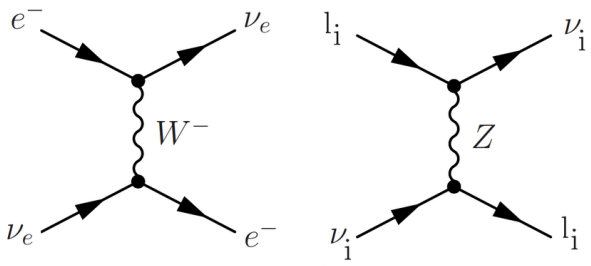

FIGURE 3: Charged and neutral current neutrino interactions with charged leptons [32].

flavor interacting with any charged lepton. This adds a potential to the Hamiltonian which is equal for all neutrino flavors and can be expressed in the flavor basis as:

$$H_{NC,f} = V_{NC} \begin{pmatrix} 1 & 0 & 0 \\ 0 & 1 & 0 \\ 0 & 0 & 1 \end{pmatrix}, \tag{8}$$

where V_{NC} is the strength of the potential and f denotes that it is expressed in the flavor basis. Since this affects all flavors equally, the NC potential does not modify the oscillations. It is only the differences between the eigenvalues of the Hamiltonian that cause neutrino oscillations. In CC interactions however, neutrinos interact with their charged counterparts through a W^+ boson, or a W^- boson for antineutrinos. Because there are in general no muons and taus but a lot of electrons in the Earth, this potential only affects electron neutrinos. Since the first matrix element on the diagonal in the flavor basis corresponds to ν_e, the CC Hamiltonian can be expressed as:

$$H_{CC,f} = V_{CC} \begin{pmatrix} 1 & 0 & 0 \\ 0 & 0 & 0 \\ 0 & 0 & 0 \end{pmatrix}. \tag{9}$$

Here the strength of the potential is $V_{CC} = \sqrt{2} G_F n_e$ [31], where G_F is the Fermi constant, and n_e is the electron number density. Since this potential only applies to electron neutrinos, it changes the differences between the eigenvalues of the Hamiltonian. In turn, it modifies the neutrino oscillations, resulting in different oscillation wavelength and amplitudes. These effects have to be taken into account when calculating transition probabilities of neutrinos traveling through the Earth.

2.6 Neutrino interactions in matter

The detector of interest in this project is the IceCube Neutrino Observatory (see Section 2.7 for details). It is located inside the ice sheet at the South Pole, and neutrinos are observed through interactions with ice molecules. Although the vast majority of neutrinos pass directly through the detector, many different types of interactions exist. The category of interactions which dominate at the energies considered in this project (E_ν ~1-1000 GeV) is deep inelastic scatterings (DIS) [33, 34]. In a DIS event a neutrino hits a nucleon of an atom in a water molecule. The neutrino interacts via the weak force with one of the

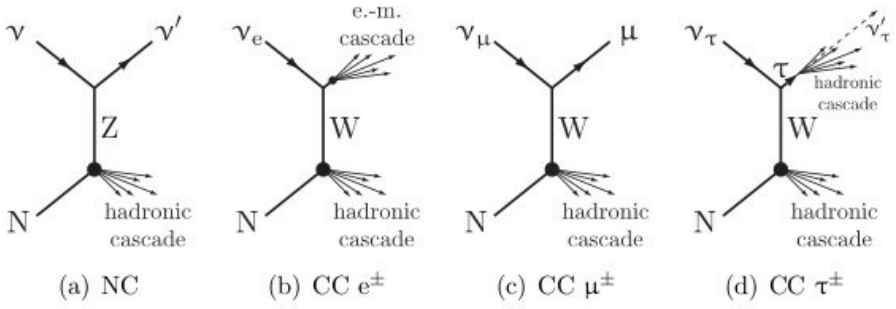

FIGURE 4: Main neutrino interaction types in ice [35].

quarks of the nucleon. At this high energy range, this process breaks apart the nucleon, creating a hadronic cascade of particles. The particles created in the cascade lead to a lot of photons being emitted, which can be observed as light by a detector.

DIS events can be further subdivided into several categories, depending on the interacting neutrino type and the exchanged boson. All possible scenarios are shown in Figure 4. In each case a hadronic cascade is created originating at the nucleon. In addition to this, different processes will occur, depending on the outgoing lepton.

In NC DIS the neutrino survives. Since the neutrino is (almost) invisible to detectors, only the hadronic cascade is observed in these events.

In CC DIS events a charged lepton of the same flavor as the initial neutrino is emitted. If the initial neutrino is an electron neutrino, an electron is emitted. The dominant process of energy loss for a high-energy electron traveling in matter is bremsstrahlung [29]. In this process, the electron emits a high-energy photon, which in turn produces an electron positron pair. The process can then repeat itself for many iterations until the energy of the individual electrons and positrons are below a critical energy, E_c, specific to the matter. An electromagnetic cascade of particles is thus created by the electron, which is brighter than a hadronic cascade with the same energy. This means that two overlapping cascades are created in this event type.

If the CC DIS event is caused by a muon neutrino, a highly relativistic muon is produced. The muon traverses the ice more freely than the electron, because bremsstrahlung is inversely proportional to the square of the mass of the lepton, and is thus suppressed for muons. Instead, the dominant process of energy loss is Cherenkov radiation [29]. This phenomenon occurs when a charged particle travels faster than the speed of light in a medium. Since this is the case for muons created in this process, they emit Cherenkov light in a cone, which can be seen as a long track in a detector. A muon neutrino CC DIS event thus produces a cascade with a long track traveling away from it. Finally, if the incoming neutrino is a tau neutrino, a tau is emitted. Since the tau lifetime is short, it will often decay inside a detector. Taus have several decay channels and most of these include pions. The decay results in a hadronic cascade in addition to the one originating from the initial CC interaction. At the energies considered here, the two hadronic cascades are however overlapping and will look the same as a single cascade in a detector. In addition to this, muons and electrons can also be created in a tau decay.

2.7 The IceCube Neutrino Observatory

The IceCube Neutrino Observatory is the largest neutrino observatory in the world [36]. It is located at the geographic South Pole, deep inside the ice sheet, and spans an entire cubic kilometer. It is an ideal place to build a neutrino observatory for many reasons. One main reason is that the ice layers in the detector are (for the most part) transparent, allowing the light produced in neutrino interactions to reach the sensors. In addition, it is dark at the depth where the detector is located, which lowers the observed noise. Furthermore, an attractive feature of the ice is that it is stationary once it is frozen. Thus the geometry of the detector remains constant, as opposed to an observatory located in water (which otherwise has similar properties to ice). Finally, the depth of the ice sheet allows for the sensor to be placed far below the surface. The ice above the sensors then acts as a shield from muons coming from the atmosphere above the detector.

A diagram of the IceCube facility is depicted in Figure 5. The detector consists of 78 strings laid out in a hexagonal grid with 125 meters spacing and lowered almost 3 kilometers into the ice sheet. On the bottom kilometer of each string 60 Digital Optical Modules (DOMs) are attached 17 meters vertically apart from each other. The total number of active DOMs is 5,484 [37].

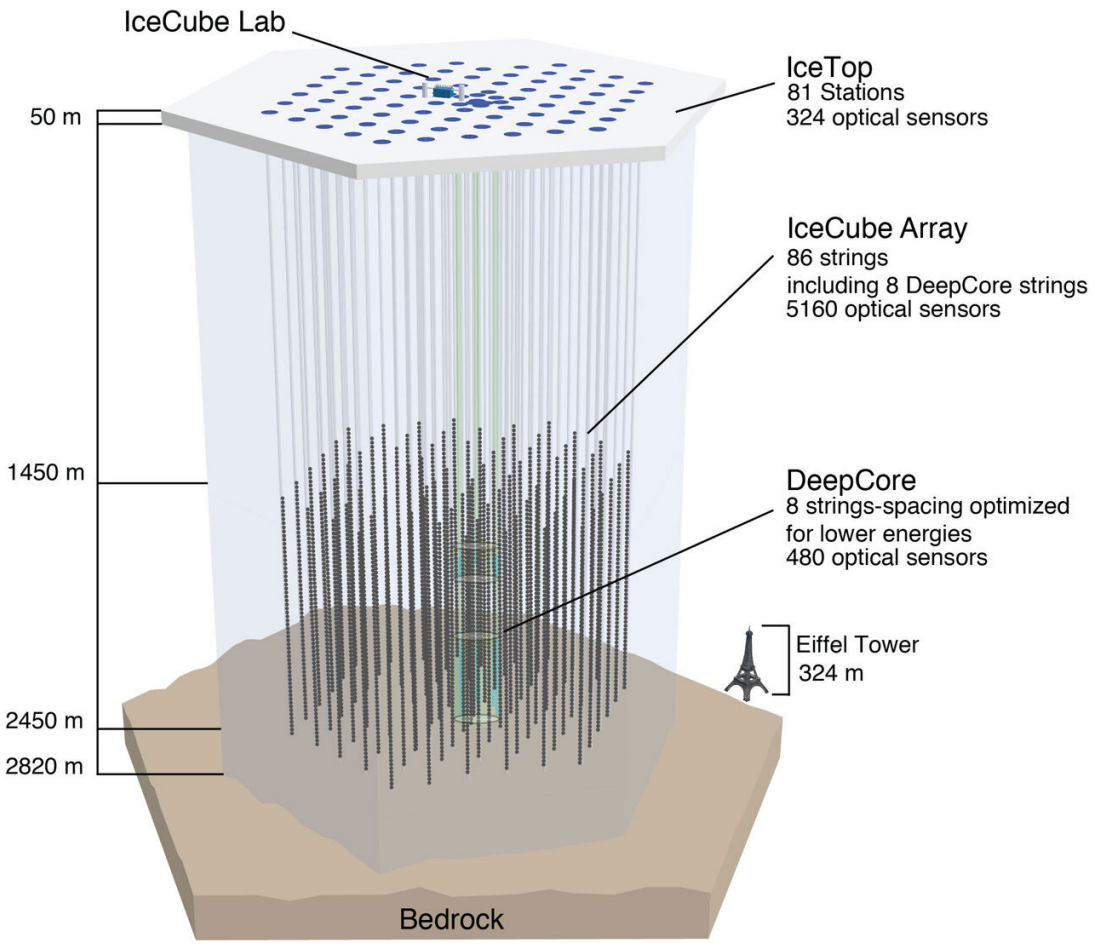

FIGURE 5: Diagram of the IceCube Neutrino Observatory [36].

A DOM is a 30 cm diameter spherical detector with a housing made of pressure-resistant glass. In the bottom half of the shell, a large photomultiplier tube (PMT) is situated pointing downwards, which is responsible for observing the incoming light produced in neutrino interactions. When a photon enters a PMT it strikes a cathode where electrons are released, because of the photoelectric effect [38]. The electrons travel through the PMT where dynodes amplify the number of electrons. An anode then collects this signal and transfers it to the rest of the DOM. Thus a PMT transforms an observed photon signal into an electrical signal. The PMT is connected to the electronics placed in the top half of the DOM, which consist of various circuit boards and a CPU. These are responsible for triggering, timestamping signals, calibration, and turning the electrical signal into a digital signal, among other things [39, 36]. Every DOM is also connected to its neighbors, and the information about coincident signals are used for triggering. This greatly reduces the amount of noise that gets registered and the amount of data needing to be processed. Finally, the digital signal is send out through a cable, along the string, and up to the facility at the surface.

The main IceCube array is optimized for detecting astrophysical neutrinos in the energy range TeV to PeV [36]. Close to the center of the array however, eight additional strings are placed which are optimized for lower energy events of 10 GeV to 100 GeV. This sub-array is called DeepCore. The strings of DeepCore are placed closer together than the grid of the main array, with an average horizontal spacing of only 75 meters. The vertical spacing of the DOMs is also only 7 meters. Low-energy events generally produce less light and thus create a smaller bright volume in the ice, needing smaller distances between DOMs to register. Thus, the dense spacing of DOMs allows DeepCore to measure lower energy events better than the main IceCube array. This makes it ideal for observing atmospheric neutrinos [40]. The top 10 DOMs on each DeepCore string are also used to improve filtering out vertically traveling muons.

In addition to these two arrays, an array of 81 stations are located at the surface. This array is called IceTop and focuses on measuring cosmic ray air showers initiated above the detector. Since atmospheric neutrinos are produced in air showers, IceTop is used as a partial veto for downgoing neutrinos [36].

All the different arrays of IceCube are connected to the IceCube Laboratory (ICL). The data collected from the DOMs is sent to the server room where the IceCube online systems are located, which is responsible for data filtering, triggering, monitoring, event selection, and more [36].

2.8 Event reconstruction and identification

The data collected by IceCube, from electrical signals in individual DOMs to reconstructed neutrino events, goes through many layers of processing. An important step in this process is when coincident DOM hits are sorted into individual events. At this stage every event is represented by series of pulses; one for each triggered DOM, labeled with time and deposited charge [41]. Here additional filters and event selections are applied to reject noise and extract actual physics event candidates. A high-energy and a low-energy event are shown in Figure 6.

The event-level information is used to reconstruct interaction types and other relevant

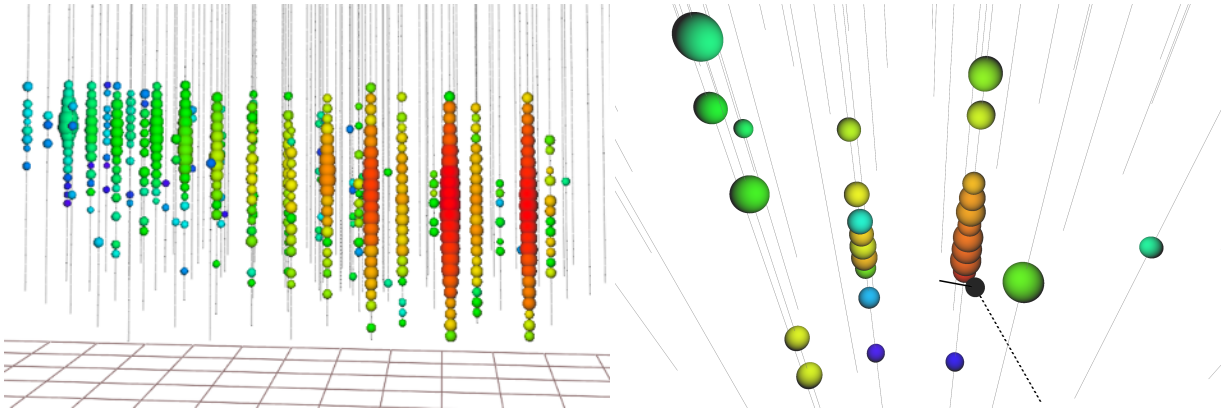

(A) (B)

FIGURE 6: Left: An example of a 290 TeV muon neutrino event named IceCube-1170922A. Every sphere is a DOM hit where the color indicates time (red is early and blue is late) and the size represents deposited charge. [42, 41]. Right: A simulated 25 GeV muon neutrino event inside the dense array in DeepCore. The dotted line represents the true direction of the incoming neutrino and the solid black line indicates the direction of the outgoing muon [41].

observables. In DeepCore, events can generally only be sorted into two types; cascade-like events and track-like events [33, 43]. In cascade-like events, only a cascade is seen in the detector as a somewhat spherical distribution of DOM hits originating from the center. These events can be caused by all neutrino flavors. In track-like events however, both the cascade and an elongated track originating from it is seen in the detector. This type of event is caused by muon neutrinos. The muon neutrino events are thus easy to individually tag. The information about whether the event is cascade-like or track-like is included in a reconstructed parameter called PID. This has a value between zero and one, where zero means that the event is cascade-like and one means that it is track-like. It thus informs us about the likelihood of an event being a muon neutrino CC interaction, and in turn holds information on the flavor composition.

The reconstructed observables relevant to this project are the neutrino energy and incident angle. The energy is mainly reconstructed from the magnitude of the charge deposited in the triggered DOMs and the angle is determined from the shape (in both space and time) of the signal. Due to the elongated shape of track-like events, their angles are reconstructed better than for cascades.

The tool used for reconstruction of the data-sample used in this project is called `Retro` [41]. It relies on pre-calculated tables to estimate the hypothesis with the maximum likelihood. It fits each event with both a track and cascade hypothesis and eight parameters: interaction point (x, y, z, and t), incident angles (azimuth $\phi_{azimuth}$ and zenith θ_{zenith}), the energy of the outgoing muon, and energy deposited in the cascade. By maximizing the likelihood it finds the event type and set of parameters which fit the data best.

3 Quantum gravity and neutrino oscillations

On microscopic scales, particles behave quantum-mechanically. This behavior is well-described by the theory of quantum field theory, which also takes special relativity into account. In this theory, the known particles of the Standard Model are excitations of quantum fields and the three forces; the strong, weak, and electromagnetic force, are interactions with the force carriers. On macroscopic scales however, gravity is a dominant force. This is well-described by the theory of general relativity, in which gravity is a consequence of the curvature of space-time. This curvature is caused by the mass and energy of matter. Thus both quantum field theory and general relativity are widely accepted and experimentally tested theories. However, if one attempts to combine these two theories, problems arise and they turn out not to be compatible with each other.

There are many examples of the incompatibility of quantum mechanics and general relativity, like the singularity in the center of a black hole, the black hole information paradox [44], and the Big Bang. In general however, quantum field theory is unable to explain gravity. Complications arise when gravity, as described in general relativity, is attempted to be expressed as a quantum force in a quantum field theory framework. Quantum field theory is formulated on a fixed background of space-time. It is thus static and does not change. However, we know from general relativity that space-time is dynamic, and that particles in space-time affect the curvature of space-time itself. It is when this effect is introduced in quantum field theory that the theory breaks down. The result is that the gravitational force becomes non-renormalizeable.

The topic of Renormalization [45] is very complex, and thus a simple qualitative picture is given here. Renormalization is an important mathematical technique in quantum field theory. It allows us to treat the infinities which arise in calculations, and replace them with quantities that are measurable by experiments. This can for instance be the mass or charge of an electron, and it specifically compensates for the self interactions of particles. That the gravitational force in quantum field theory is non-renormalizeable means that this technique can not be applied and the infinities can not be replaced. As a result of this, gravity can not be described in a way consistent with other forces in quantum field theory. The theories of quantum field theory and general relativity are thus not compatible.

Instead, a new theory is needed to describe the force of gravity in a quantum-mechanical framework. This field of theoretical physics is called quantum gravity, however no accepted theory has yet been found. Two proposed solutions are string theory [46] and loop quantum gravity [47], which are very complex fields and only described on a qualitative, surface level here. String theory describes the known particles and the force-carrying bosons as strings with vibrational modes. The vibrations of the strings determine the known properties of the particles; like mass, charge etc. The theory is able to describe the graviton; a boson which carries the gravitational force, thereby unifying all the four fundamental forces. On the other hand, loop quantum gravity assumes that space-time itself is quantized and consists of loops. This allows for gravity to be described as a curvature of this space-time, like in general relativity. Additionally, the theory also incorporates the fundamental quantum forces of the Standard Model. It is thus a theory of quantum gravity, which does not unify gravity with the other forces. The two mentioned theories are not widely accepted, primarily due to their lack of testable predictions, which is a

consequence of the weakness of gravity.

Despite the difficulties in forming a rigorous theory of quantum gravity, potential characteristics of a quantum-mechanical space-time are commonly proposed by quantum gravitational theories. This allows us to formulate heuristic models of quantum gravity effects, so that they can be searched for experimentally. Specifically, in this chapter we present phenomenologically how neutrino oscillations are affected by two effects predicted by quantum gravity: lightcone fluctuations, and neutrino - virtual black hole interactions. Additionally, a mathematical framework is given, in which oscillation probabilities with quantum gravity effects can be calculated.

3.1 The Planck scale

Although problematic, directly combining quantum mechanics and general relativity can yield remarkable results. An example of this is if the formulas for the De Broglie wavelength and the Schwarzschild radius are combined. The De Broglie wavelength relates the energy, E, of a massless particle to its wavelength, λ, and is given by:

$$\lambda = \frac{hc}{E}, \tag{10}$$

where h is the Planck constant and c is the speed of light (hence natural units are not used here). The De Broglie wavelength is derived from quantum mechanics. On the other hand the Schwarzschild radius is derived from general relativity and is the radius of a black hole with mass m:

$$r_s = \frac{2Gm}{c^2} = \frac{2GE}{c^4}, \tag{11}$$

where G is the gravitational constant and the relation $E = mc^2$ is used. Now these two equations can be combined to determine how energetic a massless particle should be, for its wavelength to become smaller than two times the Schwarzschild radius (which gives a diameter):

$$\frac{\hbar c}{E} = \frac{4GE}{c^4} \quad \Rightarrow \quad E = \sqrt{\frac{hc^5}{4G}} \tag{12}$$

If we assume that all the energy of a massless particle is confined inside one wavelength, exceeding this energy would create a black hole. It can thus be thought of as a rough energy limit of a massless particle. The diameter of a black hole with this energy is then $d = \sqrt{4hG/c^3}$, and can in turn be seen as the smallest possible wavelength of a massless particle.

This example illustrates that approaching such energies or distances, both quantum mechanics and gravity become important. The assumptions which go into this calculation are not necessarily robust, and it should not be seen as a strict proof that particles turn into black holes at the Planck energy. Rather, it should be seen as a scale at which our current theories are not sufficient to explain what happens. By ignoring numerical constants, we can thus define an energy and a length scale where a theory of quantum gravity is needed and its effects are expected to be strong. This is known as the Planck energy $E_{\text{Planck}} = \sqrt{\hbar c^5/G} \sim 1.2 \times 10^{19}$ GeV and the Planck length $L_{\text{Planck}} = \sqrt{\hbar G/c^3} = 1.6 \times 10^{-25}$ m, where $\hbar = h/2\pi$ is the reduced Planck constant.

Quantum gravity effects are expected to be weak at low energies and strong for particles approaching the Planck energy. The highest energy particle ever observed however is a cosmic ray that had an energy of $(320 \pm 90) \times 10^9$ GeV [48]. Although this energy is extreme, it is many orders of magnitude below the Planck energy. We thus have to search for traces of quantum gravity at lower energies. In the absence of an accepted theory of quantum gravity, the nature of this energy supression is not known. A common phenomenological approach is to represent the suppression via a power-law [13, 14, 49, 50, 51, 52, 53]. If the strength of a quantum gravity effect is represented by a parameter, Γ, then the power-law energy-dependence can be expressed as:

$$\Gamma \propto \left(\frac{E}{E_0}\right)^n, \tag{13}$$

where E_0 can be seen as a pivot energy, and n controls to which power the strength of the effect grows or is suppressed relative to this energy. The value of n is thus normally positive for quantum gravity models. The value of E_0 is arbitrary, because it is often absorbed by other parameters of the models (see e.g. Equation 14 or 15). It is however commonly set to $E_0 = E_{\text{Planck}}$, which makes it easy to relate other parameters of a model to Planck scale expectations.

3.2 Lightcone fluctuations

A common expectation of quantum gravity is that Heisenberg's uncertainty principle applies to space-time itself. As a result of this, the curvature of space-time fluctuates on microscopic distances [3, 4, 5]. Space-time is thus not smooth and flat, as assumed in classical physics, but is instead often said to have a foam-like structure [1, 2]. Particles traveling in such an environment experience random fluctuations to their travel distances, times, and velocities. This phenomenon is known as *lightcone fluctuations* [6, 7]. Effects as these can accumulate over time or distance and are preferably searched for in particles which travel far.

Some of the furthers-travelling particles come from astrophysical objects. Our ability to see clear pictures of extremely distant objects can put strong constrains the strength of lightcone fluctuations. Studies of photons from events like gamma ray bursts and quasars, have been carried out previously in [54, 55, 56, 57, 58].

Another candidate of particles which travel far is neutrinos. High-energy neutrinos can travel much further than high-energy photons, due to their weekly interacting nature. This opens a different energy range at which these these effects can be studied. Specifically for neutrinos, fluctuations of travel distances, times, and velocities also result in particles emitted from the same source, not having evolved equally once they reach a detector. For instance, muon neutrinos emitted from the same part of the atmosphere will not be in the exact same superposition of neutrino flavors as they arrive at IceCube. In a neutrino observatory, the flavor composition of individual neutrinos is not observed. Instead, the observed number of neutrinos depends on the average flavor composition of all neutrinos reaching the detector. Fluctuations of space-time are thus expected to result in modifications to the oscillation patterns observed in neutrino experiments. This is also a signature which does not exist for photons and allows for additional experimental ways of testing quantum gravity theories.

In this project, we mainly consider distance fluctuations. The main consequence of the fluctuations is an intrinsic uncertainty in travel distance, δL, which is expected to accumulate as a function of distance, L. Together with the energy-dependence of Equation 13, the accumulation of distance uncertainty can be expressed as [14]:

$$\delta L(E, L) = \delta L_0 \left(\frac{L}{L_0}\right)^m \left(\frac{E}{E_0}\right)^n, \tag{14}$$

where δL_0 controls the strength of the effect and L_0 is a reference distance. The parameter m controls how the uncertainty accumulates with distance. A 'natural' expectation is that space-time fluctuations are uncorrelated and thus the uncertainty grows as $\sqrt{L}$, which corresponds to $m = 0.5$. A value of $m < 0.5$ represents anti-correlated fluctuations.

If $m = 0$ the fluctuations are fully anti-correlated, which will result in a distance independent effect. This can be interpreted as measurements of distance having a fundamental uncertainty. For most Planck scale predictions however, the intrinsic distance uncertainty is essentially unmeasurable because the effect does not accumulate. The $m = 0$ scenario is thus not considered any further in this project.

Conversely, a value of $m > 0.5$ represents correlated fluctuations, where $m = 1$ is fully correlated. It has been shown that distance fluctuations with $m = 1$ can be interpreted as velocity fluctuations [14]. In this case, velocity fluctuations refer to the velocity of neutrinos being fluctuated at emission. Thus, the velocity is only perturbed once at the point of production and not continually as a particle travels.

3.3 Neutrino-virtual black hole interactions

If the fluctuations of the curvature of space-time are extreme enough, space-time might collapse and form a singularity. When space-time forms a singularity, a black hole is created, and hence the existence of microscopic black holes is often postulated by quantum gravity theories [8, 9]. Due to their small mass, they will evaporate almost immediately via Hawking radiation and are thus expected to be extremely short-lived. Additionally, microscopic black holes should be treated quantum-mechanically and can exist as virtual particles temporarily violating conservation of energy. They are thus often refered to as *virtual black holes* (VBHs). Consequently, they can be created in quantum fluctuations and will constantly appear and disappear in vacuum. This can be thought of as the virtual electron positron pairs in quantum electrodynamics responsible for vacuum polarization.

As particles travel through space, they will interact with VBHs, if they couple to them. Specifically, VBHs are expected to couple to the mass of particles. Since we know that neutrinos are massive, they could potentially interact with VBHs. The theoretical framework of the neutrino-virtual black hole (ν-VBH) interaction is still unknown, and hence we explore several heuristic scenarios as proposed in [13].

The three ν-VBH interaction models considered are depicted in Figure 7 and are as follows:

- **Phase pertubation:** The incoming neutrino interacts with the VBH and its wave-function undergoes a large, random phase perturbation. Otherwise the neutrino is unchanged. This may result from extreme local space-time curvature around the VBH.

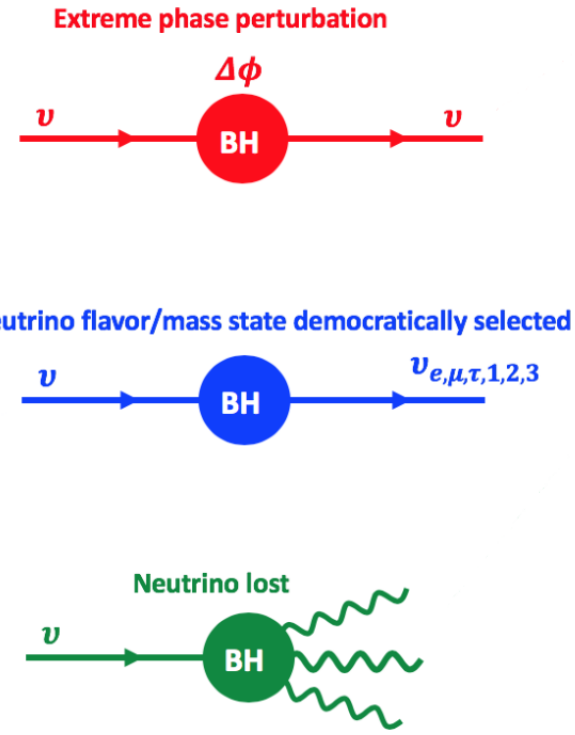

FIGURE 7: The three considered scenarios of what happens when a neutrino interacts with a virtual black hole. Figure provided by supervisor.

- **State selected:** VBHs are not expected to conserve global quantum numbers [52]. As a result of this, the flavor of the neutrino might be randomized as it interacts with the VBH. The VBH essentially collapses the wavefunction to a randomly chosen flavor states, violating conservation of flavor. Alternatively, since VBHs couple to the mass of particles, the neutrino might be emitted as one of the mass states, which also does not conserve flavor.

- **Neutrino loss:** The incoming neutrino is either lost completely or it is emitted via Hawking radiation as a different particle or in a different direction. In any case, the neutrino is not observed. This process thus potentially violates particle number conservation laws or even conservation of momentum.

In general these scenarios result in loss of information, since the initial states can not be determined from the final states. Especially in the neutrino loss scenario, the overall probability is not conserved. The quantum information is thus lost behind the event horizon of the VBH, and the time evolution of the system is non-unitary. It is also apparent that these models should affect the observed neutrino oscillation patterns. For instance, in the neutrino loss model both survival and transition probabilities should go to zero as travel distance increases.

In addition to the energy-dependence in Equation 13, the ν-VBH interaction models depend only on one parameter; the mean free path of a neutrino interacting with a VBH. The mean free path can also be seen as a coherence length, $L_{\text{MFP}} = L_{\text{coh}}$, because all information about the initial state is lost when a neutrino interacts with a VBH. We can

define the energy-dependent strength of the considered effect, Γ, as the inverse of the coherence length [13]:

$$\Gamma(E) = (L_{\text{coh}})^{-1} = \Gamma_0 \left(\frac{E}{E_0} \right)^n, \tag{15}$$

where Γ_0 is the value of Γ at $E = E_0$ and controls the overall strength of the effect. The value of Γ_0 thus depend on E_0 and will be written as $\Gamma_0(E_0)$ where relevant. It is also important to note that the coherence length is a very general metric for characterizing any kind of decoherence effect. It can be used to compare the models discussed here to other decoherence models, even from non-quantum gravitational sources.

3.4 Simulations of models

We can use sumulations to explore how lightcone fluctuations and ν-VBH interactions modify neutrino oscillations. Simulations of the three ν-VBH interaction scenarios described in Section 3.3 have been performed in [13] and lightcone fluctuations have been performed in [14]. These simulations are repeated for this project and agreement has been verified. This section describes the methods and results of the two aforementioned papers.

By solving the Schrödinger equation of a neutrino, it can be propagated through space. In vacuum the evolution of a neutrino mass state is then a plane wave:

$$|\nu_j, L\rangle = e^{-i\frac{m_j^2 L}{2E}} |\nu_j, 0\rangle. \tag{16}$$

The probabilities of going from state α to β can then be found by projecting these states onto the flavor basis via the PMNS matrix like in Equation 2:

$$\begin{aligned} P(\nu_\alpha \to \nu_\beta) &= |\langle \nu_\beta, 0 | \nu_\alpha, L \rangle|^2 \\ &= |\langle \nu_\beta, 0 | \sum_{jk} U_{\beta k} U^*_{\alpha j} e^{-i\frac{m_j^2 L}{2E}} |\nu_j, 0\rangle|^2 \\ &= |\sum_j U_{\beta j} U^*_{\alpha j} e^{-i\frac{m_j^2 L}{2E}}|^2. \end{aligned} \tag{17}$$

Now a large ensemble of neutrinos can be simulated by propagating them according to Equation 16 and 17. If no perturbations are applied they will all evolve equally, which is the standard expectation for neutrinos traveling in vacuum. However, scenarios involving ν-VBH interactions and lightcone fluctuations can be simulated by applying perturbations, which will be discussed in Section 3.4.1 and 3.4.2, according to the models described in Section 3.3 and 3.2.

3.4.1 ν-VBH models

As stated, the $\nu-$VBH interaction models are described by one free parameter: the mean free path of a neutrino interacting with a VBH. The phase pertubation scenario can then be simulated by stochastically injecting large phase perturbations to the ensemble

at random distances according to the mean free path. The phase perturbations, $\delta\phi$, are applied to Equation 16 like:

$$|\nu_j, L\rangle = e^{-i\left(\frac{m_j^2 L}{2E}+\delta\phi\right)}|\nu_j, 0\rangle, \tag{18}$$

where $\delta\phi$ is chosen randomly in the interval $[0, 2\pi]$. The observed neutrino flux in an experiment depends on the average survival/transition probabilities of the neutrinos passing the detector. Thus, the average of the simulated ensemble is calculated to determine the resulting oscillation pattern. The corresponding simulation performed for this project is shown in Figure 8.

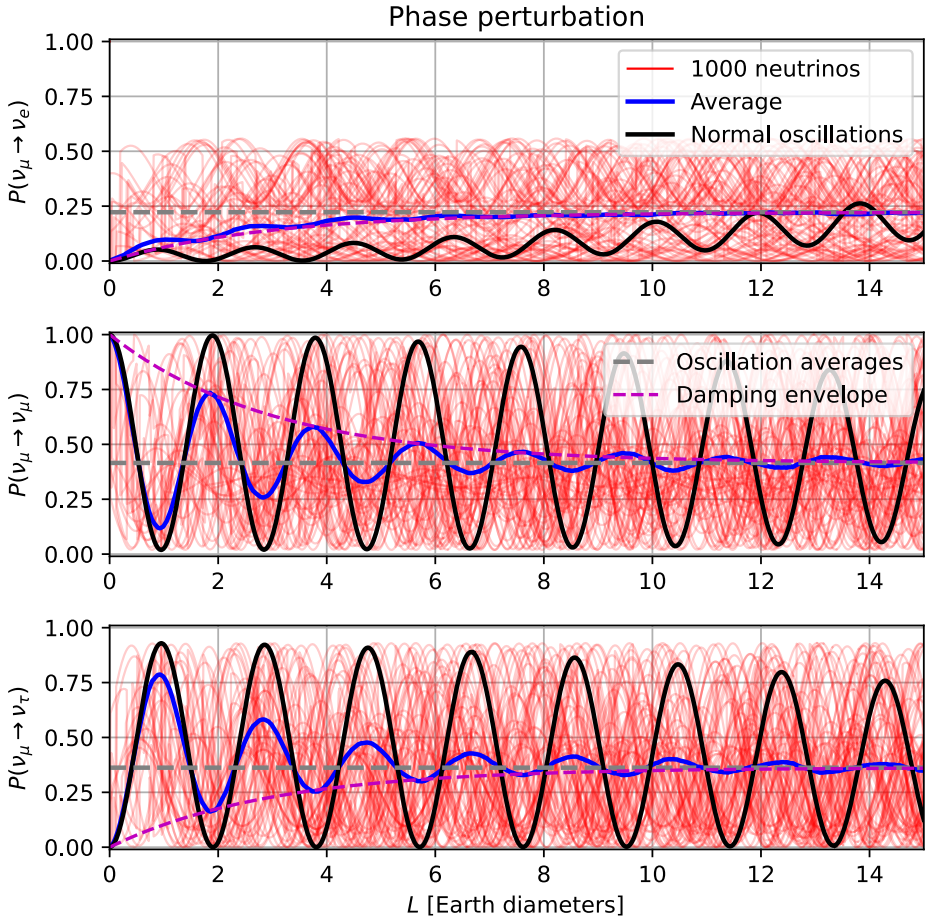

FIGURE 8: Simulations of neutrino oscillations in vacuum with ν-VBH interactions phase perturbation scenario for a 25 GeV neutrino starting as a muon neutrino. The mean free path is chosen to be three Earth diameters. This is similar to the simulations carried out in [13]. In beginning of the simulation ($L = 0$), all the 1000 red lines (individual neutrinos) are behind the black line (normal oscillations). Gradually as distance increase, more and more of the neutrinos undergo a phase perturbation, and the distribution gets increasingly spread out. The average of the individually simulated neutrinos are shown in blue alongside the exponential damping envelope. Here an exponential damping which converges toward the oscillation averages is seen.

From the simulation it is found that oscillations are dampened in the ν-VBH phase perturbation scenario. The damping envelope is exponential and of the form $e^{-\alpha L}$, and both the survival and transition probabilities converge toward the oscillation averages.

To simulate the state selected model, the wavefunctions of the neutrino ensemble are at random distances (according to the mean free path) changed to a random flavor state. The result is shown in Figure 9. This scenario also results in exponential damping of the oscillations, but here the oscillation probabilities converge toward equal population of the three flavor states ($P(\nu_\mu \rightarrow \nu_\beta)$=1/3). It is shown in [13] that collapsing the wavefunctions to one of the mass states instead gives the same overall behavior of the oscillation probabilities. Hence, both the 'flavor state selected' and 'mass state selected' cases are treated simultaneously in this project as the 'state selected' model.

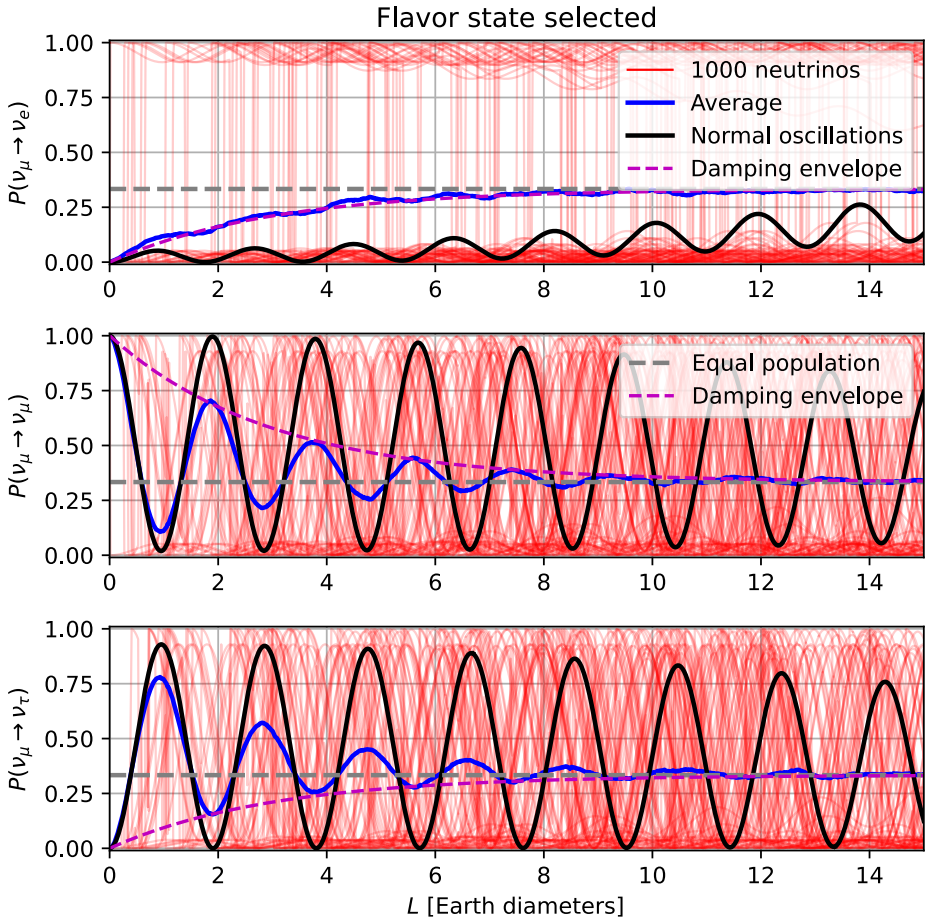

FIGURE 9: Simulations of the flavor state selected scenario. See Figure 8 for more details. Here an exponential damping which converges toward equal population (1/3) is seen.

Finally, in the neutrino loss simulation, individual neutrinos are removed from the ensemble at random distances according to the mean free path. Removing a neutrino is done by setting its survival and transition probabilities to zero from the point where it is removed and onward. The result is shown in Figure 10, where an exponential damping of the oscillations is seen. Here the oscillation probabilities for all flavors go to zero.

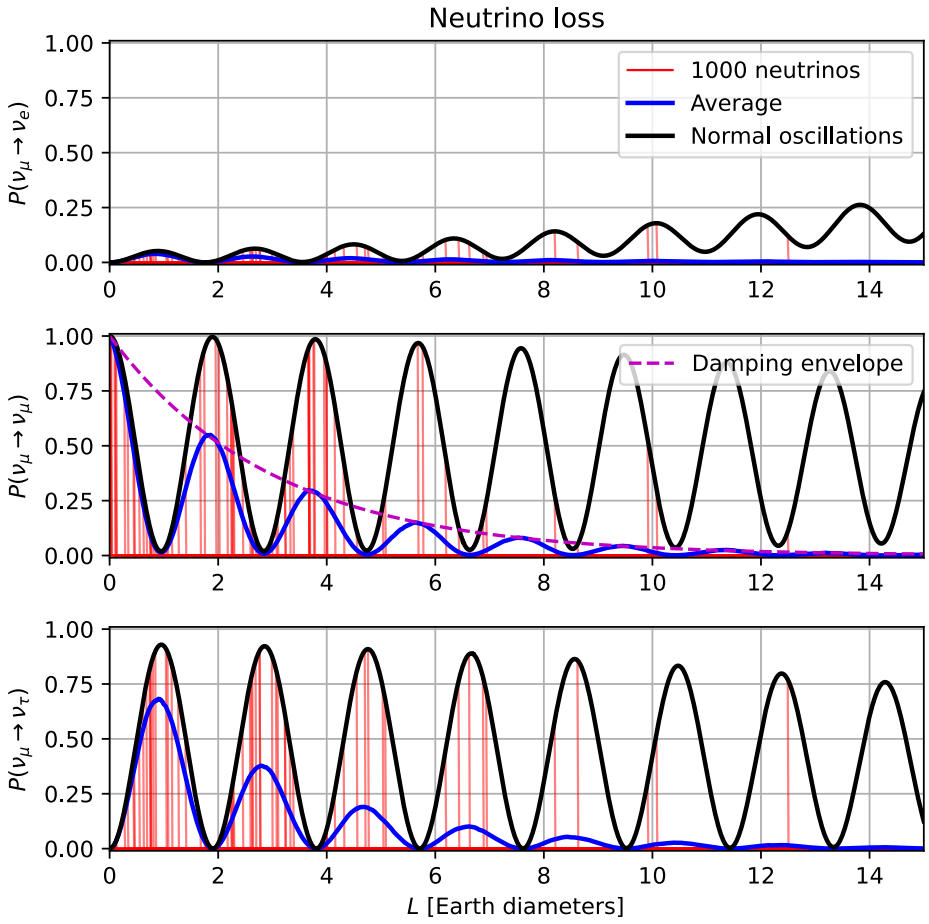

FIGURE 10: Simulations of the neutrino loss scenario. See Figure 8 for more details. Here an exponential damping which converges toward zero is seen.

3.4.2 Lightcone fluctuation models

Neutrino propagation with lightcone fluctiuations are simulated in the form of distance fluctuations. The neutrinos are evolved in discrete distance steps of $L_0 + \delta L_0'$, where L_0 is constant and $\delta L_0'$ is a random distance drawn from a Gaussian distribution with width δL_0. The accumulated distance perturbation is then $\Delta L(L) = \sum \delta L_0'$, where δL_0 controls the strength of this effect and represents the same paramter as δL_0 in Equation 14. The evolution of individual neutrinos can then be expressed as:

$$|\nu_j, L\rangle = e^{-i\frac{m_j^2}{2E}(L+\Delta L(L))}|\nu_j, 0\rangle. \tag{19}$$

Two distinct values of the parameter m (described in Section 3.2) are tested. In the uncorrelated $m = 0.5$ case, the value of $\delta L_0'$ is randomized for every distance step for every neutrino in the ensemble. The result is shown in Figure 11. In this scenario the oscillations are exponentially dampened, e^{-L}, like in the ν-VBH cases. However, the fast oscillations (related to the large mass splittings, Δm_{23}^2 and Δm_{13}^2) are dampened faster than the slow oscillation (related to the small mass splitting, Δm_{12}^2). The damping is

thus dependent on the wavelength, λ_{ij}, of the oscillation.

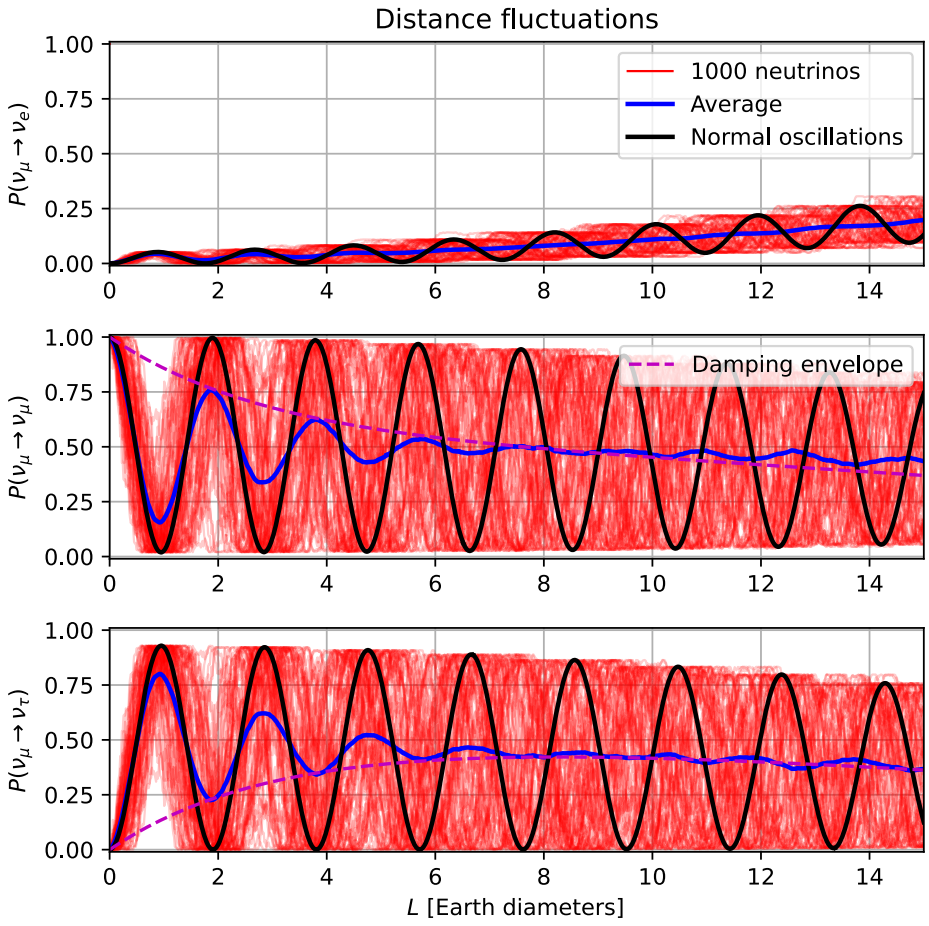

FIGURE 11: Simulations the lightcone fluctuations scenario with $m = 0.5$ (uncorrelated distance fluctuations). See Figure 8 for more details. The damping envelope here is simplified which might cause the deviation for $P(\nu_\mu \to \nu_\mu)$ at large distances.

For the fully correlated, $m = 1$, scenario, the value of $\delta L_0'$ is only chosen randomly for the first distance step. For every subsequent step, the same $\delta L_0'$ is applied, making the fluctuations fully correlated. Here it is also apparent why this scenario can be interpreted as velocity fluctuations. The result of this simulation is shown in Figure 12. The resulting damping has the same wavelength dependence as the $m = 0.5$ case, but the damping envelope goes like e^{-L^2}.

Using Equation 14, the full form of the damping, unified for all m, can then be expressed as [14]:

$$\exp\left\{-\left[\frac{\delta L}{\eta\lambda_{ij}}\right]^2\right\} = \exp\left\{-\left[\frac{\delta L_0}{\eta\lambda_{ij}}\left(\frac{L}{L_0}\right)^m\left(\frac{E}{E_0}\right)^n\right]^2\right\}, \tag{20}$$

where η is a constant that depends on the distribution that $\delta L_0'$ is pulled from. In [14] the value of the parameter is found to be $\eta \sim 0.23$ for a Gaussian distribution, by fitting the

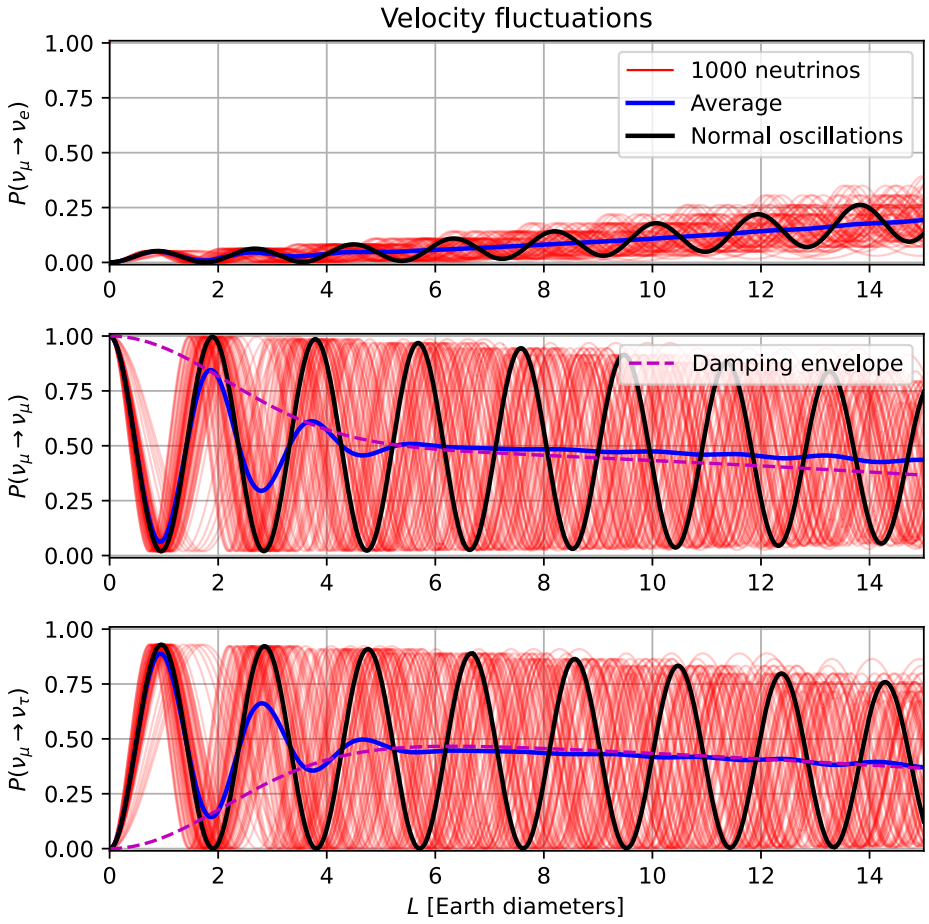

FIGURE 12: Simulations of the lightcone fluctuations scenario with $m = 1$ (velocity fluctuations). See Figure 8 for more details. The damping envelope here is simplified which might cause the discrepancy for $P(\nu_\mu \to \nu_\mu)$ at large distances.

damping envelope to the resulting oscillations. The coherence length can then be defined similar to the ν-VBH cases as the distance at which the oscillations are dampened with e^{-1}:

$$L_{\text{coh}} = L_0 \left(\frac{\eta \lambda_{ij}}{\delta L_0} \right)^{\frac{1}{m}} \left(\frac{E_0}{E} \right)^{\frac{n}{m}}, \tag{21}$$

Using Equation 21, the energy-dependence of the damping caused by ligthcone fluctuations can also be assessed. The coherence length includes a factor of $E^{-n/m}$, however it also has an intrinsic dependence on the oscillation wavelengths, which in vacuum are $\lambda_{ij} = 4\pi E/\Delta m^2_{ij}$. The resulting energy-dependence of the effect of lightcone fluctuations in vacuum is $E^{1/m-n/m}$. This is contrary to the energy-dependence of the coherence lengths resulting from the ν-VBH interactions which is E^{-n}.

3.5 Open quantum system

As shown in the simulations described in Section 3.4, neutrino oscillations are dampened for both the lightcone fluctuations described in Section 3.2 and all ν-VBH interaction scenarios described in Section 3.3. This can be seen as a loss of coherence of the neutrino ensemble. We now present an analytical framework derived in [13] and [14], which can describe the behavior observed in the simulations.

Neutrino propagation with ν-VBH interaction and lightcone fluctuations can be formulated as an open quantum system. This formalism is very general and describes a quantum system which is in contact with its environment and can lose information to it. As a result, any kind of decoherence can be treated using this formalism. In this analysis the quantum system is a propagating neutrino which interacts with either an environment consisting of VBHs or a fluctuating spacetime. The challenge is then to figure out exactly how to parameterize the models in this framework to obtain the specific decoherence observed in the simulations.

In an open quantum system, the time evolution is found by solving the Lindblad master equation [59], given by:

$$\dot{\rho} = -i[H, \rho] - \mathcal{D}[\rho]. \tag{22}$$

Here ρ is the density matrix, which for a three neutrino system can be represented by a 3x3 matrix:

$$\rho = \sum_j p_j |\psi_j\rangle \langle\psi_j| \doteq \begin{pmatrix} \rho_{11} & \rho_{12} & \rho_{13} \\ \rho_{21} & \rho_{22} & \rho_{23} \\ \rho_{31} & \rho_{32} & \rho_{33} \end{pmatrix}, \tag{23}$$

where $\rho_{ij} = \rho^*_{ji}$ because ρ is Hermitian. By $\mathcal{D}[\rho]$ in Equation 20, what is left is just the Schrödinger equation written in density matrix form. Thus, by solving the Lindblad master with $\mathcal{D}[\rho] = 0$, normal neutrino oscillations with no damping are obtained (Equation 6 for the vacuum Hamiltonian).

The operator $\mathcal{D}[\rho]$ is often called the decoherence operator/matrix and characterizes the coupling of the system to its environment. In a three neutrino case, $\mathcal{D}[\rho]$ is represented by a 3x3 matrix and is hermitian. It is however allowed to be non-unitary, which means that the system loses information/neutrinos to the environment.

The specific forms of the decoherence operator resulting in the behavior observed in the simulations described in Section 3.4 have been identified in [13] and [14]. Thus each of the three ν-VBH scenarios and lightcone fluctuations have been paired with a decoherence matrix. Expressed in the 3x3 form these are:

$$\mathcal{D}_{\text{phase}}[\rho] = \Gamma_0 \left(\frac{E}{E_0}\right)^n \begin{pmatrix} 0 & \rho_{21} & \rho_{31} \\ \rho_{21} & 0 & \rho_{32} \\ \rho_{31} & \rho_{32} & 0 \end{pmatrix}, \tag{24}$$

$$\mathcal{D}_{\text{state}}[\rho] = \Gamma_0 \left(\frac{E}{E_0}\right)^n \begin{pmatrix} \frac{1}{3}(2\rho_{11} - \rho_{22} - \rho_{33}) & \rho_{21} & \rho_{31} \\ \rho_{21} & \frac{1}{3}(-\rho_{11} + 2\rho_{22} - \rho_{33}) & \rho_{32} \\ \rho_{31} & \rho_{32} & \frac{1}{3}(-\rho_{11} - \rho_{22} + 2\rho_{33}) \end{pmatrix}, \tag{25}$$

$$\mathcal{D}_{\text{loss}}[\rho] = \Gamma_0 \left(\frac{E}{E_0}\right)^n \begin{pmatrix} \rho_{11} & \rho_{21} & \rho_{31} \\ \rho_{21} & \rho_{11} & \rho_{32} \\ \rho_{31} & \rho_{32} & \rho_{33} \end{pmatrix}, \tag{26}$$

$$\mathcal{D}_{\text{lightcone}}[\rho] = \frac{2m(\delta L_0)^2 L^{2m-1}}{L_0^{2m}} \left(\frac{E}{E_0}\right)^{2n} \begin{pmatrix} 0 & \frac{\rho_{21}}{(\eta\lambda_{21})^2} & \frac{\rho_{31}}{(\eta\lambda_{31})^2} \\ \frac{\rho_{21}}{(\eta\lambda_{21})^2} & 0 & \frac{\rho_{32}}{(\eta\lambda_{32})^2} \\ \frac{\rho_{31}}{(\eta\lambda_{31})^2} & \frac{\rho_{32}}{(\eta\lambda_{32})^2} & 0 \end{pmatrix}. \tag{27}$$

3.5.1 *SU(N)* representation

Decoherence matrices are commonly expanded in terms of the $SU(N)$ generators. This often gives more convenient expressions of the matrices. For a three neutrino system the basis is the $SU(3)$ generators called the Gell-Mann matrices:

$$\begin{gathered} b_0 = \begin{pmatrix} 1 & 0 & 0 \\ 0 & 1 & 0 \\ 0 & 0 & 1 \end{pmatrix}, b_1 = \begin{pmatrix} 0 & 1 & 0 \\ 1 & 0 & 0 \\ 0 & 0 & 0 \end{pmatrix}, b_2 = \begin{pmatrix} 0 & -i & 0 \\ i & 0 & 0 \\ 0 & 0 & 0 \end{pmatrix}, \\ b_3 = \begin{pmatrix} 0 & 0 & 0 \\ 0 & 1 & 0 \\ 0 & 0 & 1 \end{pmatrix}, b_4 = \begin{pmatrix} 0 & 0 & 1 \\ 0 & 0 & 0 \\ 1 & 0 & 0 \end{pmatrix}, b_5 = \begin{pmatrix} 0 & 0 & -i \\ 0 & 0 & 0 \\ i & 0 & 0 \end{pmatrix}, \\ b_6 = \begin{pmatrix} 0 & 0 & 0 \\ 0 & 0 & 1 \\ 0 & 1 & 0 \end{pmatrix}, b_7 = \begin{pmatrix} 0 & 0 & 0 \\ 0 & 0 & -i \\ 0 & i & 0 \end{pmatrix}, b_8 = \frac{1}{\sqrt{3}} \begin{pmatrix} 1 & 0 & 0 \\ 0 & 1 & 0 \\ 0 & 0 & -2 \end{pmatrix}, \end{gathered} \tag{28}$$

The density matrix and decoherence matrices can then be expressed as:

$$\rho = \rho_\mu b^\mu \text{ and } \mathcal{D}[\rho] = c_\mu b^\mu, \tag{29}$$

where ρ_μ and c_μ are the coefficients of the density and decoherence matrices in the Gell-Mann basis, respectively. Since the decoherence matrices depend on the density matrix, they can be expanded further:

$$\mathcal{D}[\rho] = (D_{\mu\nu}\rho^\nu)b^\mu. \tag{30}$$

Here $D_{\mu\nu}$ is the indicies of a 9x9 matrix, where ν picks an element of the density matrix and μ picks one of the gell matrices. The components of D determines the respective decoherence matrix. The D matrices corresponding to the decoherence matrices in Equation 24-27 are then:

$$D_{\text{phase}} = \left(\frac{E}{E_0}\right)^n \begin{pmatrix} 0 & 0 & 0 & 0 & 0 & 0 & 0 & 0 \\ 0 & \Gamma_0 & 0 & 0 & 0 & 0 & 0 & 0 \\ 0 & 0 & \Gamma_0 & 0 & 0 & 0 & 0 & 0 \\ 0 & 0 & 0 & 0 & 0 & 0 & 0 & 0 \\ 0 & 0 & 0 & 0 & \Gamma_0 & 0 & 0 & 0 \\ 0 & 0 & 0 & 0 & 0 & \Gamma_0 & 0 & 0 \\ 0 & 0 & 0 & 0 & 0 & 0 & \Gamma_0 & 0 \\ 0 & 0 & 0 & 0 & 0 & 0 & 0 & \Gamma_0 \end{pmatrix}, \tag{31}$$

$$D_{\text{state}} = \left(\frac{E}{E_0}\right)^n \begin{pmatrix} 0 & 0 & 0 & 0 & 0 & 0 & 0 & 0 \\ 0 & \Gamma_0 & 0 & 0 & 0 & 0 & 0 & 0 \\ 0 & 0 & \Gamma_0 & 0 & 0 & 0 & 0 & 0 \\ 0 & 0 & 0 & \Gamma_0 & 0 & 0 & 0 & 0 \\ 0 & 0 & 0 & 0 & \Gamma_0 & 0 & 0 & 0 \\ 0 & 0 & 0 & 0 & 0 & \Gamma_0 & 0 & 0 \\ 0 & 0 & 0 & 0 & 0 & 0 & \Gamma_0 & 0 \\ 0 & 0 & 0 & 0 & 0 & 0 & 0 & \Gamma_0 \end{pmatrix}, \tag{32}$$

$$D_{\text{loss}} = \left(\frac{E}{E_0}\right)^n \begin{pmatrix} \Gamma_0 & 0 & 0 & 0 & 0 & 0 & 0 & 0 \\ 0 & \Gamma_0 & 0 & 0 & 0 & 0 & 0 & 0 \\ 0 & 0 & \Gamma_0 & 0 & 0 & 0 & 0 & 0 \\ 0 & 0 & 0 & \Gamma_0 & 0 & 0 & 0 & 0 \\ 0 & 0 & 0 & 0 & \Gamma_0 & 0 & 0 & 0 \\ 0 & 0 & 0 & 0 & 0 & \Gamma_0 & 0 & 0 \\ 0 & 0 & 0 & 0 & 0 & 0 & \Gamma_0 & 0 \\ 0 & 0 & 0 & 0 & 0 & 0 & 0 & \Gamma_0 \end{pmatrix}, \tag{33}$$

$$D_{\text{lightcone}} = \frac{2m(\delta L_0)^2 L^{2m-1}}{L_0^{2m}} \left(\frac{E}{E_0}\right)^{2n} \begin{pmatrix} 0 & 0 & 0 & 0 & 0 & 0 & 0 & 0 \\ 0 & \frac{1}{(\eta\lambda_{21})^2} & 0 & 0 & 0 & 0 & 0 & 0 \\ 0 & 0 & \frac{1}{(\eta\lambda_{21})^2} & 0 & 0 & 0 & 0 & 0 \\ 0 & 0 & 0 & 0 & 0 & 0 & 0 & 0 \\ 0 & 0 & 0 & 0 & \frac{1}{(\eta\lambda_{31})^2} & 0 & 0 & 0 \\ 0 & 0 & 0 & 0 & 0 & \frac{1}{(\eta\lambda_{31})^2} & 0 & 0 \\ 0 & 0 & 0 & 0 & 0 & 0 & \frac{1}{(\eta\lambda_{32})^2} & 0 \\ 0 & 0 & 0 & 0 & 0 & 0 & 0 & \frac{1}{(\eta\lambda_{32})^2} \end{pmatrix}. \tag{34}$$

These formulations of the decoherence matrices are important for the implementations of the different models in nuSQuIDS described in Section 4.2.

3.6 'Natural' expectations

We ultimately want to relate the parameters of the considered models to expectations from quantum gravity theories. By setting $E_0 = E_{\text{Planck}}$ in the ν-VBH interaction case, Equation 15 can be re-expressed relative to the Planck scale as:

$$\Gamma(E) = \Gamma_0 \left(\frac{E}{E_{\text{Planck}}}\right)^n = \zeta_{\text{Planck}} \frac{E^n}{E_{\text{Planck}}^{n-1}}, \tag{35}$$

where $\zeta_{\text{Planck}} = \Gamma_0 / E_{\text{Planck}}$ and is a dimensionless constant. Since $L_{\text{Planck}} = (E_{\text{Planck}})^{-1}$ in natural units, the coherence length (mean free path) is then:

$$L_{\text{coh}}(E) = (\Gamma(E))^{-1} = \frac{L_{\text{Planck}}}{\zeta_{\text{Planck}}} \left(\frac{E_{\text{Planck}}}{E}\right)^n. \tag{36}$$

A rough 'natural' estimate from Planck scale theories, is that a Planck energy neutrino encounters a VBH every time it travels one Planck length [60, 13]. This implies that ζ_{Planck} is of $\sim \mathcal{O}(1)$. A different interpretation is that the coherence length is one Planck length because the neutrino travels in an environment which does not resemble a flat space-time in any way. We can thus compare the sensitives found in this project to this Planck scale expectation.

Similarly, the distance uncertainty resulting from lightcone fluctuations (Equation 14) can be re-expressed relative to the Planck scale as:

$$\delta L(E, L) = \delta L_{\text{Planck}} \left(\frac{L}{L_{\text{Planck}}} \right)^m \left(\frac{E}{E_{\text{Planck}}} \right)^n . \tag{37}$$

A neutrino travelling with the Planck energy is expected to have a travel distance uncertainty of one Planck length for every Planck length it travels [14]. This is true if $\delta L_{\text{Planck}} = L_{\text{Planck}}$, and can thus act as a rough quantum gravity theory prediction.

3.7 Motivations for using atmospheric neutrinos

Since the effects described in the previous sections increase with distance, they are ideally searched for in neutrinos which have traveled far. Naively, one would think that astrophysical neutrinos provide the best source for decoherence studies, because of their their extreme baselines compared to other sources. In [13] it is however argued that it is not yet possible to observe such effects in astrophysical data for several reasons. The high-energy extragalactic neutrino flux observed by IceCube [61] is diffuse and only a single point-source has been observed [62]. Due to the unknown initial flavor distributions of these sources, and their unknown and varying distances, the observed flavor composition will be the oscillation average [63]. This prediction is entirely degenerate with the phase perturbation scenario and might be indistinguishable from the state selected scenario (see e.g. Section 4.2). The observation of astrophysical neutrinos can however in itself place constraints on the ν-VBH neutrino loss model [64].

In [13] it is instead argued that atmospheric neutrinos are a compelling candidate for studies of decoherence, especially for the ν-VBH cases. The flavor composition of the atmospheric flux is well modeled and detectors like IceCube have good angular reconstruction, which in turn provides precise estimations of travel distance. In addition, the atmospheric neutrino datasets of IceCube have high statistics, which allow us to investigate the oscillation patterns and potential damping in great detail. With high statistics even small deviations from the undampened expectations can be resolved. Although the Earth diameter is small compared to astrophysical sources, even if only a small percentage of the neutrinos traversing the Earth encounter VBHs, a significant signal could be achieved. The Planck scale expectations of lightcone fluctuations are, on the other hand, not expected to cause detectable effects at such small travel distances [13, 14].

3.8 Alternative interpretations of damping effects

The models investigated here encompass many different types of damping. It is thus relevant to investigate if any of the observed damping scenarios are phenomenologically

degenerate with decoherence from non-quantum gravity sources. We here explore alternative interpretations of specific configurations of the models considered in this project.

One candidate for such an effect is called wave packet decoherence. Neutrinos are often treated as plane waves, which for instance leads to the vacuum neutrino oscillation probabilities of Equation 6. In reality however, they propagate as wave packets of the three mass states. Since the mass states have differing masses, they travel with slightly different velocities. This leads to the mass components of the wave packet spatially separating as the neutrino travels. The result of this, which is typically assumed to be negligible, is that the superposition degrades over distance and flavor oscillations are dampened [65]. The damping envelope resulting from this effect can be parameterized as [66]:

$$\exp\left\{-\left(\frac{\Delta m_{ij}^2 L}{4\sqrt{2}\sigma_x E^2}\right)^2\right\}, \tag{38}$$

and the transition probabilities converge toward the oscillation averages. The fundamental parameter of this model is σ_x, which is the spatial spread of the wave packet (assuming it is Gaussian). We see specifically that this damping is dependent on the mass splittings, L^2, and has an energy-dependence of E^{-4}. By comparing this damping envelope to the damping envelope of the lightcone fluctuations case in Equation 20 (and inserting the wavelengths $\lambda_{ij} = 4\pi E/\Delta m_{ij}^2$), we see that that wave packet decoherence is equivalent to the lightcone fluctuations case with $n = -1$ and $m = 1$. The relation between the parameters of the two models is then:

$$\sigma_x = \frac{\pi\eta L_0}{\sqrt{2}\delta L_0 E_0}. \tag{39}$$

By obtaining a bound on δL_0 for this specific case, we can thus relate it to a bound on σ_x. Note also that the parameters are inversely proportional to each other meaning that a small value for σ_x causes strong decoherence. An upper bound on δL_0 is thus a lower bound on σ_x.

Two other effects, neutrino absorption [67] and decay [68], were investigated in a similar manner, but were found not to be directly comparable to any of the models considered in this project. The damping resulting from both of these effects are expected to converge toward zero oscillation probability, and should thus be similar to the ν-VBH neutrino loss model. For neutrino absorption however, the damping is dependent on the matter density, which is not the case for the ν-VBH neutrino loss model. On the other hand, neutrino decay depends on the neutrino mass, causing it to produce mass-dependent damping which converges toward zero. This effect is not directly comparable to any of the models considered in this project and will thus not be discussed further.

4 Implementations of models

4.1 nuSQuIDS

The open quantum system formulations of neutrino oscillations with ν-VBH interactions and lightcone fluctuations have been implemented in `nuSQuIDS` [69] for this project.

`nuSQuIDS` is a C++-based code that propagates neutrinos through a given medium and calculates their oscillation probabilities. It is based on SQuIDS [70], which is a C++ framework designed to solve the time evolution of density matrices of quantum-mechanical systems. In SQuIDS, numerical integration of differential equations is performed using the GNU Scientific Library (GSL) [71].

The time evolution of neutrino states in `nuSQuIDS` is primarily performed by solving the Schrödinger equation in density matrix form, given by:

$$\dot{\rho} = -i[H, \rho]. \tag{40}$$

This is the same as Equation 22 with $\mathcal{D}[\rho] = 0$. The density matrix can be initialized as any of the neutrino flavors. The equation is solved in a $SU(N)$ basis and supports any number of neutrino states. In this project, the number of neutrinos is set to 3 and thus the basis is the Gell-Mann matrices defined in Equation 28; however in a different order. The ordinary differential equation solver in GSL evolves the state in discrete time/distance steps of varying size using a Runge-Kutta method.

In equation 40, H is the full Hamiltonian of the system, and includes both the vacuum Hamiltonian (dependent on the mass splittings) and the Hamiltonian from matter effects. `nuSQuIDS` also supports models of the Earth which specify the density of each Earth layer. In this analysis, a 12-layer version of the Preliminary Reference Earth Model [72] is used. In addition, `nuSQuIDS` has an 'atmospheric' mode which is specialized for neutrinos produced in the atmosphere and observed in IceCube, and loops over a provided E and $\cos(\theta_{\text{zenith}})$ grid. It can thus make accurate predictions of neutrino oscillation probabilities for neutrinos traveling through the Earth. An oscillogram of the survival probability of muon neutrinos produced in the atmosphere and observed in IceCube as calculated by `nuSQuIDS` is shown in Figure 13. The figure depicts the expected oscillation pattern observed by IceCube if no quantum gravity effects are present and neutrino oscillations are not dampened.

4.2 New models in nuSQuIDS

The construction of `nuSQuIDS` makes it easy to implement new physics into the calculations of neutrino oscillations. The code has been modified by T. Stuttard to subtract a decoherence matrix from the time evolution of the decoherence matrix (Equation 40). This effectively turns the Schrödinger equation into the Lindblad master equation as expressed in Equation 22.

Additionally, a piece of C++ code has been made which calculates the decoherence matrices of the ν-VBH cases: $\mathcal{D}_{\text{phase}}[\rho]$, $\mathcal{D}_{\text{state}}[\rho]$, and $\mathcal{D}_{\text{loss}}[\rho]$ of Equation 24, 25, and 26, respectively. For this calculation, the D matrix corresponding to the specific scenario at $E = E_0$, the value of E_0, and the energy-dependence parameter, n, have to be provided.

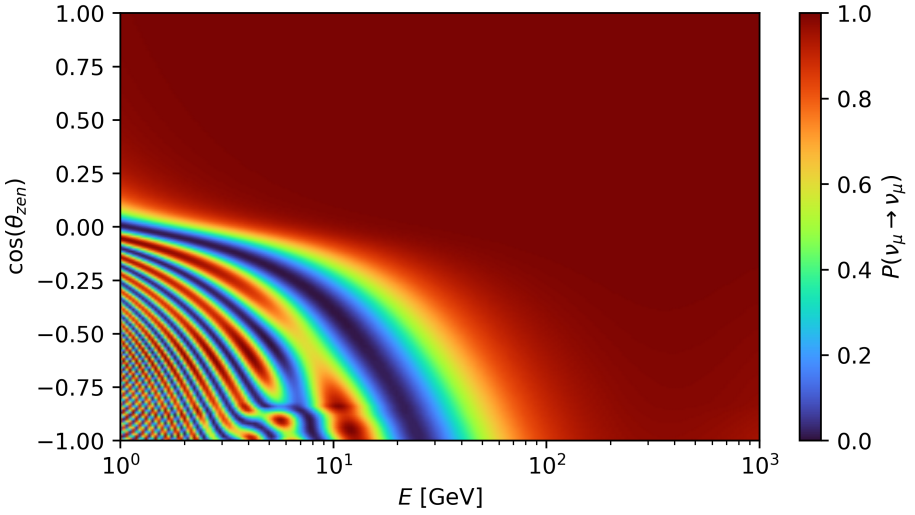

FIGURE 13: Oscillogram of standard neutrino oscillations. The survival probabilities of muon neutrinos produced in the atmosphere and observed in IceCube are shown as a function of energy and cosine to the zenith angle.

Since the $\mathcal{D}[\rho]$ matrices are energy and density matrix dependent, they are calculated for every step of the neutrino propagation.

Examples of oscillograms for each of the three ν-VBH interaction cases with $n = 1$ as calculated by `nuSQuIDS` are shown in Figure 14. Similarly, examples with $n = 0$ is shown in Figure A.1 in the appendix. The $n = 1$ case shows a slight damping of the oscillation patterns in the 10-100 GeV range and a large deficit of neutrinos above 100 GeV. Hence, for $n = 1$ (and in general positive values of n) the main signal observed if ν-VBH interactions take place is fewer neutrinos with high energies than otherwise expected. The $n = 0$ case however shows equal damping across all energies. From the figures it can also be seen that it might be especially difficult to distinguish the state selected and phase perturbation models. The neutrino loss scenario however, produces a distinct pattern.

The lightcone fluctuation model has been implemented in this thesis work in `nuSQuIDS`. The model differs from the ν-VBH models in several ways. It depends on a different set of parameters, which are δL_0, L_0, m, and η, in addition to the energy-dependence, E_0 and n. Hence, functions which can set and get these parameters have been made in `nuSQuIDS`. Additionally, a length dependence has to be taken into account when calculating the decoherence matrix.

The final important difference between lightcone fluctuations and ν-VBH interactions is that the former depends on the oscillation wavelengths. As discussed in Section 2.5, the mixing parameters of neutrinos are modified when they travel in matter, which includes the oscillation wavelengths. This effect is not fully implemented yet, but is explored in Section B in the appendix.

Since the lightcone fluctuations model has not been implemented for matter, we have chosen to proceed with it for vacuum oscillations only. This means that no matter effects will be included in the calculations of neutrinos traveling through the Earth, which

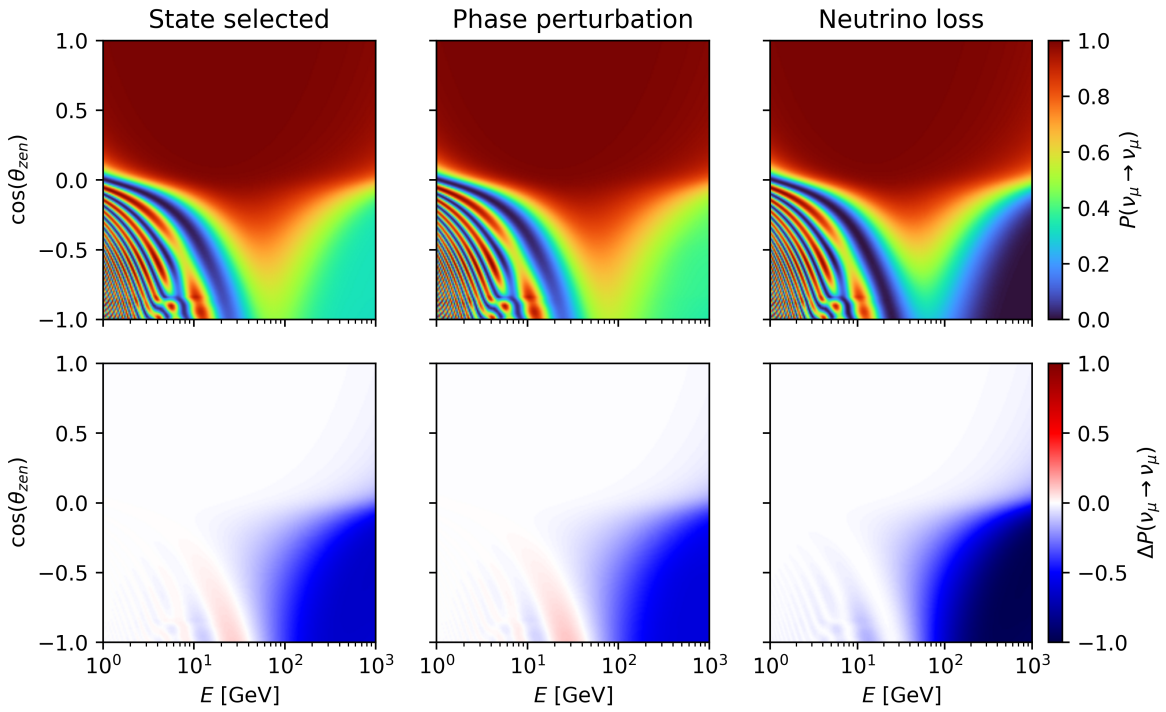

FIGURE 14: Oscillograms of neutrino oscillations with ν-VBH interactions with $L_{\text{coh}}(25GeV) = 3L_{Earth}$ (same as Section 3.4) and $n = 1$. In the bottom row the results are compared to normal oscillation by taking the difference between the oscillograms in the upper row and the oscillogram shown in Figure 13.

corresponds to that the neutrinos do not 'see' the matter in the Earth. This approach is chosen for two reasons. First, it allows us to show the analysis is possible with this model. Second, it can give order of magnitude estimates of the sensitivities.

Examples of the resulting oscillograms for uncorrelated distance fluctuations ($m = 0.5$) and velocity fluctuations ($m = 1$) with no matter effects are shown in Figure 15. The energy-dependence parameter was set to $n = 1.5$ for the $m = 0.5$ case and $n = 2$ for the $m = 1$ to obtain the same energy-dependence as the ν-VBH models shown in Figure 14. From the figure it is seen that the $m = 0.5$ case is very similar to the phase perturbation scenario. It does however have a different relative strength in the electron neutrino channel, which is not shown here. The oscillogram for $m = 1$ shows a distinct pattern from the other models.

4.3 Robustness checks

For [13] and [14], the open quantum system formulations of ν-VBH interactions and light-cone fluctuations were implemented in a code called Density Matrix Osc Solver (DMOS)[1]. In the two aforementioned papers, DMOS is shown to give results consistent with the simulations described in Section 3.4. For this project, I have had access to DMOS, and thus

[1]This code does not support an Earth model, which is why the models had to be implemented in `nuSQuIDS` for this analysis.

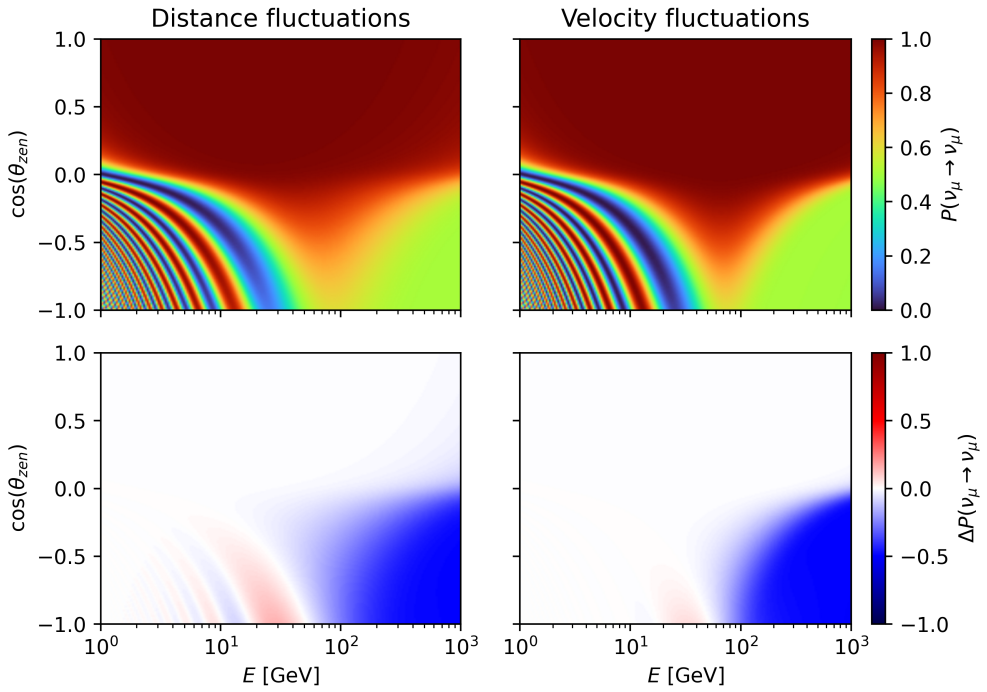

FIGURE 15: Oscillograms of neutrino oscillations in vacuum with uncorrelated distance fluctuations (left) and fully correlated distance fluctuations (right), which can be interpreted as velocity fluctuations. The decoherence parameters have been chosen so that $L_{\text{coh}}(25GeV) = 3L_{Earth}$ (same as Section 3.4) and the energy-dependence parameter is $n = 1.5$. In the bottom row the results are compared to normal oscillation in vacuum by taking the difference between the oscillograms in the upper row and an oscillogram for vacuum oscillations.

the `nuSQuIDS` implementation can be compared to it. If these two calculations agree, `nuSQuIDS` is in turn consistent with the simulations.

The first check is a 1D propagation of a 25 GeV neutrino in vacuum. The coherence length has been set to three Earth diameters (same as the simulations), and oscillation probabilities have been calculated by both `nuSQuIDS` and DMOS. The calculations were carried out for six different scenarios:

1. Neutrino oscillations without decoherence
2. ν-VBH state selected
3. ν-VBH phase perturbation
4. ν-VBH neutrino loss
5. Lightcone fluctuations with $m = 0.5$ (uncorrelated distance fluctuations)
6. Lightcone fluctuations with $m = 1$ (velocity fluctuations)

The resulting oscillation probabilities are shown in Figure 16 along with the differences bewteen the `nuSQuIDS` and DMOS calculations.

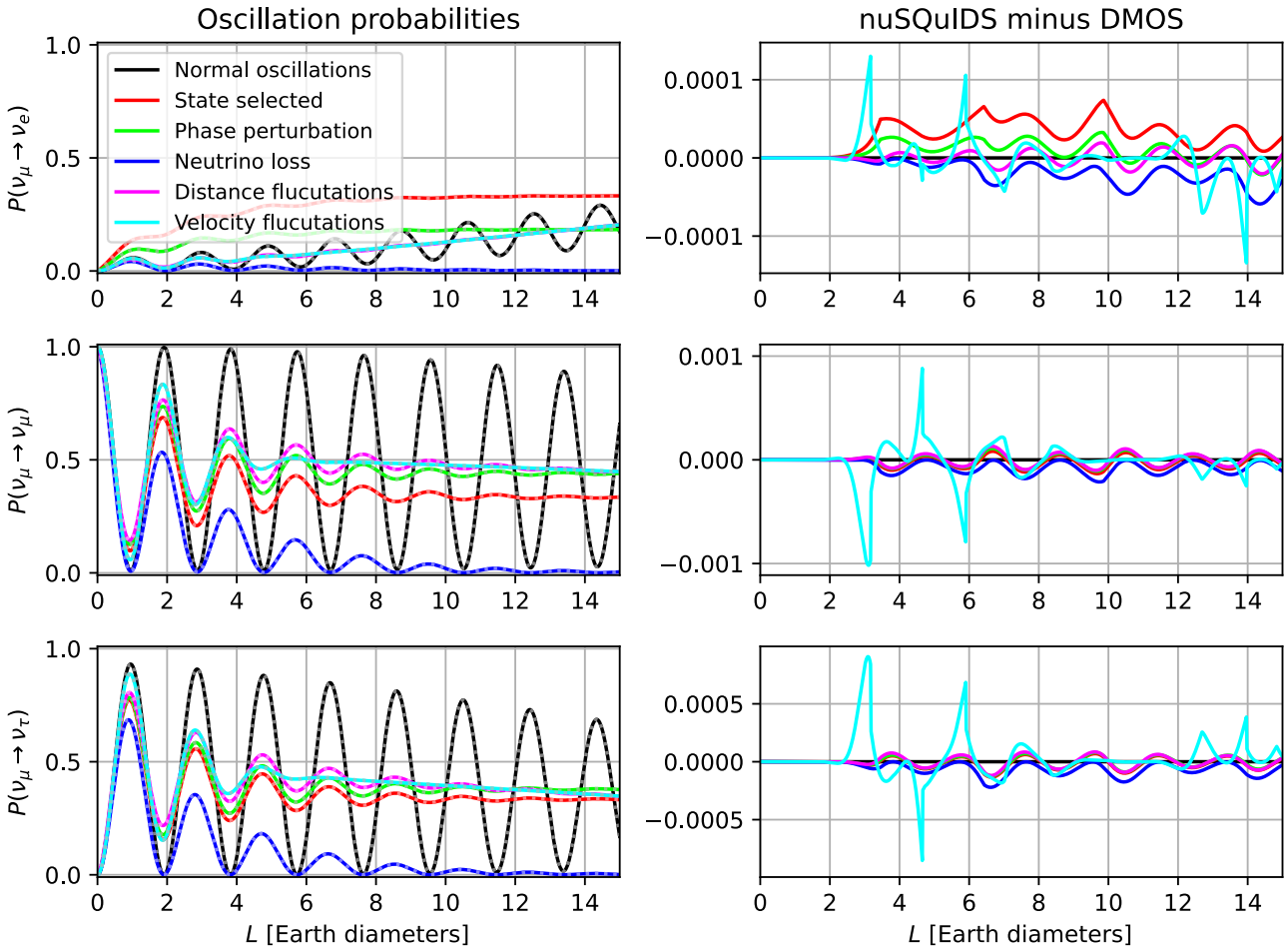

FIGURE 16: Neutrino oscillation probabilities in vacuum calculated by `nuSQuIDS` (solid lines) and DMOS (dotted lines) for the three ν-VBH scenarios and lightcone fluctuations with $m = 0.5$ (uncorrelated distance) and $m = 1$ (velocity fluctuations). Normal neutrino oscillations are calculated with both methods for reference. In the right column the difference between the respective `nuSQuIDS` and DMOS calculations are shown.

In general the two implementations agree well. Looking at the plots of the oscillation probabilities, the two calculations seem identical for all models. By investigating the differences between the corresponding results however, it can be seen that there are small discrepancies. These discrepancies have oscillation like patterns which follow the neutrino oscillations roughly. They are smallest for the normal oscillations and worst for the fully correlated lightcone fluctuations. The maximal deviation is however 0.1% oscillation probability and is thus considered to be insignificant.

A similar comparison has been carried out for propagation through a constant matter density. The density was arbitrarily set to 1.5 g/cm^3, which is roughly the density of sand, and the electron fraction was set to 0.5. As discussed in Section B.1.1, the calculations of the lightcone fluctuations do not agree with the simulations in matter. However, the implementations in `nuSQuIDS` and DMOS are the same, and they should thus agree. The results are shown in Figure A.2, with deviations larger (up to 1%) than in vacuum. The

deviation is however also present for the normal neutrino oscillations, which means it is not caused by the decoherence implementation. Instead it might be related to the constants defined in each code, since the robustness of the implementation of matter effects in DMOS has not yet been validated.

Finally, a 2D (E and $\cos(\theta_{\text{zenith}})$) comparison has been made, which uses the 'atmospheric' mode of both `nuSQuIDS` and DMOS. Since DMOS does not support an Earth model, the calculations were performed in vacuum. For this test, the energy-dependence parameter was set to $n = 1$ for the ν-VBH models and $n = 1.5$ for the lightcone fluctuation models to get the same energy-dependence. The results are shown in Figure 17. It can be seen that there is a significant disagreement of up to 5% between `nuSQuIDS` and DMOS in the atmospheric modes. This discrepancy is however present for all models including normal neutrino oscillations. The error is thus caused by the assumptions that go into the atmospheric modes of the two methods. Nevertheless, we have not been able to find any assumptions which differ. This discrepancy follows a fast oscillating pattern, and thus it will most likely average out because of the relative coarse binning chosen for this analysis (see Section 5.1).

The plots of the differences between `nuSQuIDS` and DMOS in the atmospheric modes all look the same, and not much information about the decoherence implementations can be gathered from them. However, to assess the difference between the decoherence implementations, the difference between the `nuSQuIDS` and DMOS calculations of normal neutrino oscillations can be subtracted from the other plots. This leaves us with the discrepancy between the decoherence implementations specifically, which is also shown in Figure 17. This shows some strange patterns in the deviations, but they are however less than 1% and are thus considered to be insignificant.

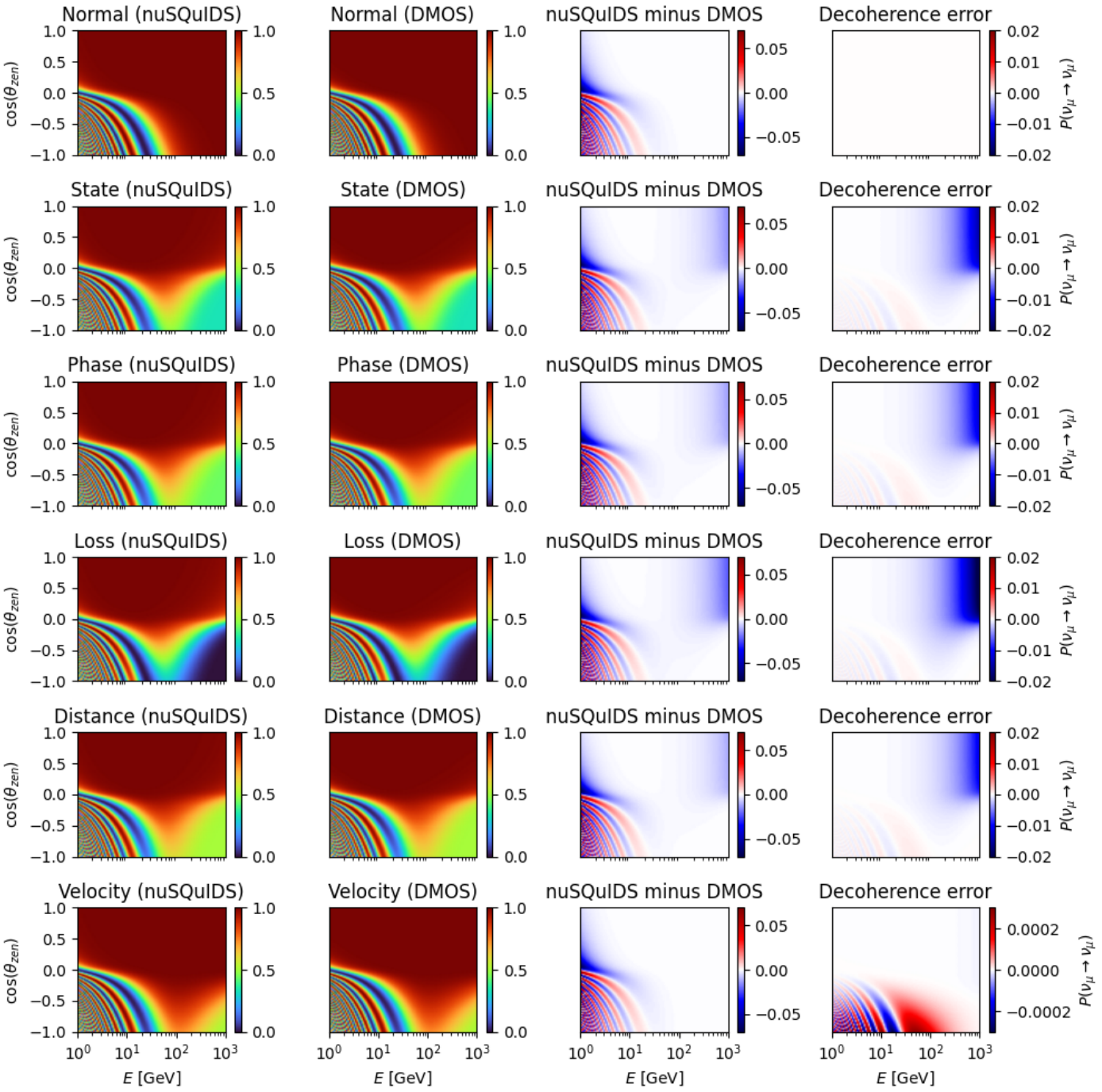

FIGURE 17: Neutrino oscillation probabilities calculated by `nuSQuIDS` (first column) and DMOS (second column) in the 'atmospheric' modes in vacuum. The results are shown for normal neutrino oscillations, the three ν-VBH scenarios, and lightcone fluctuations with $m = 0.5$ (uncorrelated distance) and $m = 1$ (velocity fluctuations). In the third column, the difference between the `nuSQuIDS` and DMOS calculations is depicted. The fourth column shows the same, but but with the normal oscillations discrepancy subtracted, to assess the uncertainty of the decoherence implementations.

5 Statistical analysis

The main objective of this project is to build a statistical data analysis using IceCube DeepCore data to search for the decoherence effects described in Section 3. The development of the considered data sample, called the oscNext sample, is underway by the IceCube collaboration and due to conclude soon. In the meantime, this analysis is carried out on pseudodata, i.e. predictions of what the data will look like based on simulations. This allows us to build and test the entire analysis. In addition, we can estimate how sensitive the data sample is to the investigated models and compare to other studies of decoherence. When the oscNext sample is finished, the analysis is ready to be carried out on the real data.

The analysis performed in this project is closely tied to a different analysis called the standard oscillations analysis. It attempts to measure the parameters of standard neutrino oscillations with the oscNext sample (Δm^2_{23} and θ_{23} are the relevant parameters in this data sample), without any physics beyond the Standard Model. The two analyzes have the same data selection, same treatment of systematic uncertainties, and use the same analysis tools. The only major addition here is decoherence resulting from quantum gravity. Many aspects of the analysis have thus been studied prior to this project, and the results apply to this analysis as well.

In addition to the decoherence analysis of the oscNext sample, the same effects are planned to be searched for in an analysis called the MEOWS decoherence analysis. The sample used for this analysis is higher energy than oscNext and contains $\mathcal{O}$(TeV) muon neutrinos from the full IceCube array. The higher energy sample is expected to perform better for damping which increases rapidly with energy (positive values of n), and the two analyses are thus complimentary to each other.

5.1 The oscNext sample

The oscNext high statistics sample consists of $\sim 210,000$ neutrino events measured by DeepCore. It is collected during 9.3 years of livetime and is ideal for measurements of atmospheric neutrino oscillations.

The raw data observed in the detector has gone through 6 levels of filtering, noise and atmospheric muon rejection, and reconstruction. The event selection stages are thus called level 2 through 7. The final level reconstruction happens at level 6, which uses `Retro Reco` for particle identification and estimations of neutrino energy and incident angle. In addition to this, a final level of cuts to remove noise and muons from the data is applied in level 7 using the reconstructed variables. The resulting data sample has a contamination of only 0.6% from muons and a negligible noise contamination.

The neutrino events are sorted into a 3D histogram in reconstructed energy, E, reconstructed zenith angle, $\cos(\theta_{\text{zenith}})$, and particle identity (PID). The binning used in this project is common with other analyses of the oscNext sample and has been thoroughly studied previously.

The reconstructed energy binning goes from 5 GeV to 300 GeV and is $\log_{10}$-spaced. Events below 5 GeV are not included, because at these energies the number of DOM hits is too low to properly reconstruct the energy. At energies above 300 GeV too much

of the event is not contained in DeepCore, which gives a very large uncertainty on the reconstructed energy.

The reconstructed $\cos(\theta_{\text{zenith}})$ bins are linearly spaced in the range -1 (directly upgoing) to 0.3 ($\sim$ 17 degrees above the horizon). The cut at $\cos(\theta_{\text{zenith}}) = 0.3$ is placed to avoid contamination of muons produced in the atmosphere directly above the detector. Additionally, for downgoing events the muon produced in the air shower may be seen in the detector at the same time as the neutrino, which causes the event to be rejected. This is known as a 'self veto' [73] which is placed because simultaneous neutrino and muon events are difficult to disentangle and reconstruct. The cut at $\cos(\theta_{\text{zenith}}) = 0.3$ thus avoids any possible self-veto effects.

PID is a quantity which represents if the event is cascade like or track like. If the PID value is close to 0, the event is cascade-like, and conversely if it is close to 1 it is track-like. The chosen binning for PID is three bins which are 0.00-0.50, 0.50-0.85, 0.85-1.00. These bins are of increasing purity of track-like events, where the first bin is a mix of tracks and cascades and the third bin has a high purity of tracks. The events in the third bin are likely to be muon neutrino CC interactions, and the PID bins thus hold the information about the observed flavor composition.

An example of a simulated expectation of what the data will look like without statistical fluctuations is shown in Figure 18.

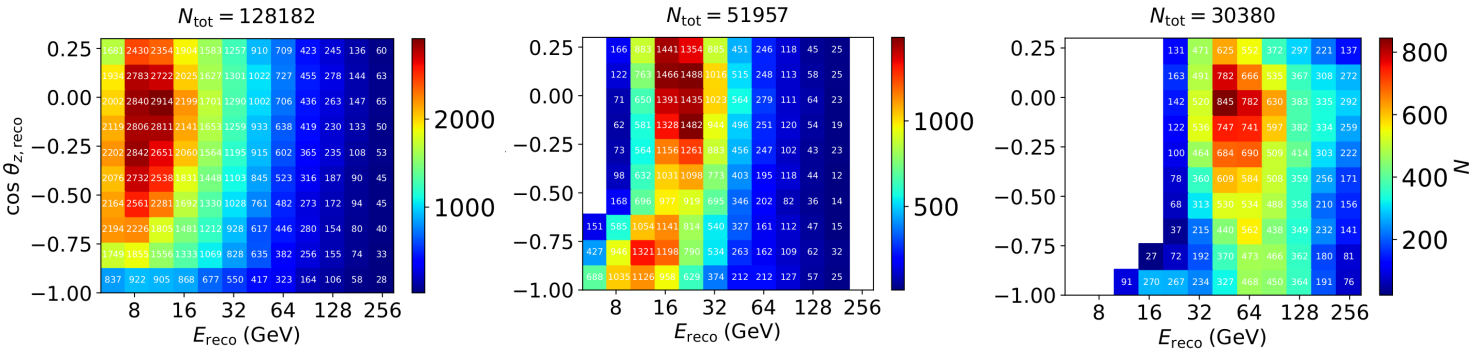

FIGURE 18: An unflucuated simulated expectation of the oscNext sample generated with the model parameters set to the nominal values (see Table 2). The leftmost histogram is the first PID bin 0.00-0.50, the middle histogram is 0.50-0.85, and the third is 0.85-1.00, with increasing track-like event purity. The white bins are masked because there are no or very few events in them.

5.2 PISA

To calculate the expected number of neutrinos observed in the oscNext sample, a Python framework named PISA [74] is used. PISA is specifically developed to analyze IceCube data and perform various statistical tests. It is therefore also used for the statistical analysis in this project.

Because of the complexity of the physics and geometry of IceCube and its detectors, we have to rely on Monte-Carlo (MC) simulations to predict the number of observed neutrino events. These simulations are based on arbitrarily chosen initial distributions of

energy and incident angle, and propagates particles through the ice. Interactions of the primary particles take place, and the generated photons are propagated through the ice. The photon propagation takes into account scattering and absorption on dust and the properties of the ice. Finally the DOM response is simulated, turning the photons into DOM hits. After this, the same levels of filtering as the oscNext sample are applied, and the event sample is stored as a file. All MC simulations used were performed prior to this project.

The input for PISA is the files generated from the MC simulations. The individual events are then re-weighted by PISA to match the real initial distributions of the incoming neutrinos, or take into account any additional physics. Any action or subsequent calculation applied to the MC events is called a 'stage' and controlled by a configuration file called a 'pipeline'. In this analysis, the stages include a data loader, re-weighting based on atmospheric flux, cross section calculations, neutrino oscillations, systematic uncertainties, and binning. The resulting histogram is called a template, which can then be compared to the data.

The PISA stage of focus in this analysis is the nuSQuIDS oscillations stage. It calls the `nuSQuIDS` functions to calculate neutrino oscillation probabilities for the parameters provided in the pipeline. The `nuSQuIDS` calculation is slow to perform for every single neutrino event in the sample. For optimization it is instead set to calculate the oscillation probabilities on an irregular grid in E and $\cos(\theta_{\text{zenith}})$. The grid has finer spacing in the core crossing region, because the oscillation patterns have a smaller structure there, and the total number of nodes is 2750. The MC events are then re-weighted by the oscillation probability of the nearest node. It has been verified that the error introduced by this method is negligible.

The implementations of the ν-VBH and lightcone fluctuation models discussed in Section 4 have been incorporated into the `nuSQuIDS` PISA stage. The specific model/scenario has to be chosen, and then the stage sets the D matrix accordingly. In addition to this it sets the parameters of the model to the provided values in the pipeline. This allows us to calculate full predictions of the number of observed neutrinos in the oscNext sample with ν-VBH interactions and lightcone fluctuation.

5.3 Model parameters

The free parameters of the ν-VBH interaction models are Γ_0, n, and E_0. For lightcone fluctuations the free prameters are δL_0, n, E_0, L_0, and m. Since E_0 and L_0 are arbitrary and only affect the interpretation of the other parameters, they can be fixed to some arbitrary reference value during a fit. Additionally, we consider lightcone fluctuations with $m = 0.5$ (uncorrelated distance fluctuations) and $m = 1$ (velocity fluctuations) as two separate cases. This leaves us with two parameters for each case; one which controls the strength of the effect (Γ_0 for ν-VBH interactions and δL_0 for lightcone fluctuations) and one which controls the shape of the energy-dependence (n for both cases). Both parameters can be free in a fit, which would be relevant if actual data is considered, and especially if a signal is observed. We have however chosen to keep n fixed and test the models for discrete values of it. By taking this approach, we obtain sensitivities of the data to the models for specific values of n.

5.3.1 Systematic parameters

In addition to the decoherence models, the calculations of the expected number of neutrinos depend on many additional parameters. These parameters are related to aspects of the detector or the theory which are not known exactly, and thus need to be kept free in a fit. Since they are not the focus of the analysis, but still have to be taken into account, they are often called nuisance parameters. They represent e.g. systematic uncertainties in the detector, calibration, and modeling of the neutrino flux and cross sections.

A full list of the parameters considered in this analysis is provided in Table 2, which all go into the various PISA stages and can be controlled by PISA itself. They can thus all potentially be varied if during a fit, but many are however kept fixed, because they have minimal impact on the analysis. The impact of having the parameters free in a fit as opposed to fixing them has been studied for the standard oscillations analysis. For the analysis in this project we have chosen to keep the same parameters free/fixed whenever we perform a fit. This should however ideally be studied again for this analysis, to reveal any unexpected correlation between the fixed nuisance parameters and the models studied here.

The 'nominal' values shown in Table 2 constitute the null hypothesis and will be used throughout the analysis. The nominal values of the oscillation parameters are set to the NuFit results, except for δ_{CP} which is set to 0. This is because the experiment is insensitive to this parameter, causing it to have limited impact on the analysis.

The first two parameters in Table 2, `delta_index`, `energy_pivot`, go into the atmospheric flux calculations and modify its energy-dependence. The analysis is especially sensitive to `delta_index`. It modifies the power-law energy-dependence of the atmospheric neutrino flux, accounting for uncertainties in the measured spectrum of primary cosmic rays that instigate the air showers.

The `pion_ratio` and all of the `barr` parameters are also part of the flux calculations. They control the rates of pion and kaon production in the air shower, accounting for uncertainties in the theoretical modeling of these hadronic processes [75].

The `Genie` parameters and `dis_csms` are related to the calculations of the cross section of neutrino interactions in the ice. The `_norm` parameters and `aeff_scale` control the normalizations of the different neutrino types and interactions. Finally, the parameters `dom_eff`, `hole_ice_p0`, `hole_ice_p1`, `bulk_ice_abs`, and `bulk_ice_scatter` are related to propagation of photons in the ice and the detection process. Here 'hole ice' refers to the ice in the drill holes at IceCube, which has different properties than the rest of the ice (the 'bulk ice'), since it was melted and frozen again. We thus have two dimensionless parameters which scale the properties of the hole ice, and two dimensionless parameters which scale the scattering and absorption of photons in the bulk ice. Finally, the DOM efficiency controls how well the PMTs converts a photon signal into an electrical signal. It thus rescales the deposited energies in the DOMs. These parameters are part of the MC simulations, and the method used to vary them without re-running the simulations is described in Section 5.3.2.

Name	Nominal value	Range	Prior	Unit	Fixed
delta_index	0.0	$[-0.5, 0.5]$	± 0.1	dimensionless	False
pion_ratio	0.0	$[-0.25, 0.25]$	± 0.05	dimensionless	True
barr_a_Pi	0.0	$[-0.5, 0.5]$	± 0.1	dimensionless	True
barr_b_Pi	0.0	$[-1.5, 1.5]$	± 0.3	dimensionless	True
barr_c_Pi	0.0	$[-0.5, 0.5]$	± 0.1	dimensionless	True
barr_d_Pi	0.0	$[-1.5, 1.5]$	± 0.3	dimensionless	True
barr_e_Pi	0.0	$[-0.25, 0.25]$	± 0.05	dimensionless	True
barr_f_Pi	0.0	$[-0.5, 0.5]$	± 0.1	dimensionless	True
barr_g_Pi	0.0	$[-1.5, 1.5]$	± 0.3	dimensionless	False
barr_h_Pi	0.0	$[-0.75, 0.75]$	± 0.15	dimensionless	False
barr_i_Pi	0.0	$[-0.61, 0.61]$	± 0.122	dimensionless	False
barr_w_K	0.0	$[-2.0, 2.0]$	± 0.4	dimensionless	False
barr_x_K	0.0	$[-0.5, 0.5]$	± 0.1	dimensionless	True
barr_y_K	0.0	$[-1.5, 1.5]$	± 0.3	dimensionless	False
barr_z_K	0.0	$[-0.61, 0.61]$	± 0.122	dimensionless	True
barr_w_antiK	0.0	$[-2.0, 2.0]$	± 0.4	dimensionless	True
barr_x_antiK	0.0	$[-0.5, 0.5]$	± 0.1	dimensionless	True
barr_y_antiK	0.0	$[-1.5, 1.5]$	± 0.3	dimensionless	True
barr_z_antiK	0.0	$[-0.61, 0.61]$	± 0.122	dimensionless	True
theta12	33.82	$[31.61, 36.27]$	Uniform	degree	True
theta13	8.61	$[8.22, 8.98]$	Uniform	degree	True
theta23	49.7	$[0, 90]$	Uniform	degree	False
deltacp	0.0	$[0.0, 360.0]$	Uniform	dimensionless	True
deltam21	7.39×10^{-5}	$[6.79, 8.01] \times 10^{-5}$	Uniform	electron_volt ** 2	True
deltam31	2.525×10^{-3}	$[1, 7] \times 10^{-5}$	Uniform	electron_volt ** 2	False
decoherence_model	randomize_flavor			dimensionless	True
gamma0	0.0	$[0.0, 1 \times 10^{-13}]$	Uniform	electron_volt	False
n	0.0			dimensionless	True
E0	1.0			gigaelectron_volt	True
Genie_Ma_QE	0.0	$[-2.0, 2.0]$	± 1.0	dimensionless	False
Genie_Ma_RES	0.0	$[-2.0, 2.0]$	± 1.0	dimensionless	False
dis_csms	0.0	$[-3.0, 3.0]$	± 1.0	dimensionless	False
livetime	9.28			common_year	True
aeff_scale	1.0	$[0.1, 2.0]$	Uniform	dimensionless	False
dom_eff	1.0	$[0.8, 1.2]$	± 0.1	dimensionless	False
hole_ice_p0	0.101569	$[-0.6, 0.5]$	Uniform	dimensionless	False
hole_ice_p1	-0.049344	$[-0.15, 0.05]$	Uniform	dimensionless	False
bulk_ice_abs	1.0	$[0.9, 1.1]$	± 0.05	dimensionless	False
bulk_ice_scatter	1.05	$[0.85, 1.25]$	± 0.1	dimensionless	False

TABLE 2: All parameters of the PISA pipeline for the ν-VBH interactions state selected model.

5.3.2 Hypersurfaces

The oscNext sample is generated from Monte Carlo simulations, which depend on the detector and ice properties, namely `dom_eff`, `hole_ice_p0`, `hole_ice_p1`, `bulk_ice_abs`, and `bulk_ice_scatter`. In the analysis we wish to treat these parameters as nuisance parameters, and thus allow them to be free in a fit. However, since the MC simulations are slow, we need a method to change the parameters without having to re-run the MC simulations every time this is done.

A solution to this problem is called hypersurfaces. The Monte Carlo simulations have been performed for a discrete set of combinations of the parameters. Specifically, 30 different simulated datasets were made, which give the predicted number of neutrinos for all bins in the dataset for many different values of the systematic parameter. If we then look at one single bin, we have the expected bin count for 30 different combinations of `dom_eff`, `hole_ice_p0`, `hole_ice_p1`, `bulk_ice_abs`, and `bulk_ice_scatter`. This can be seen as 30 points in a $5 + 1$ dimensional space, where five of the dimensions are the parameters and the sixth dimension is the bin count. If we assume that the bin count depends linearly on each parameter, the 30 points span a surface in this six dimensional space, i.e. a hypersurface. An illustration of the hypersurface for one bin is shown in Figure 19. The surface can then be fitted to the points via χ^2 minimization, which provides us with a slope of the bin count in each of the five parameters and an overall intercept/normalization. The slope can then be used to estimate how this bin changes as a function of the parameters.

The process can then be repeated for every single bin in the dataset, which gives us a hypersurface for every bin. We can thereby estimate how the entire dataset changes if the parameters that went into the Monte Carlo simulation were different. This allows us to practically vary each of these parameters without having to re-run the Monte Carlo simulation. This method has been implemented in this analysis and is applied by a PISA stage.

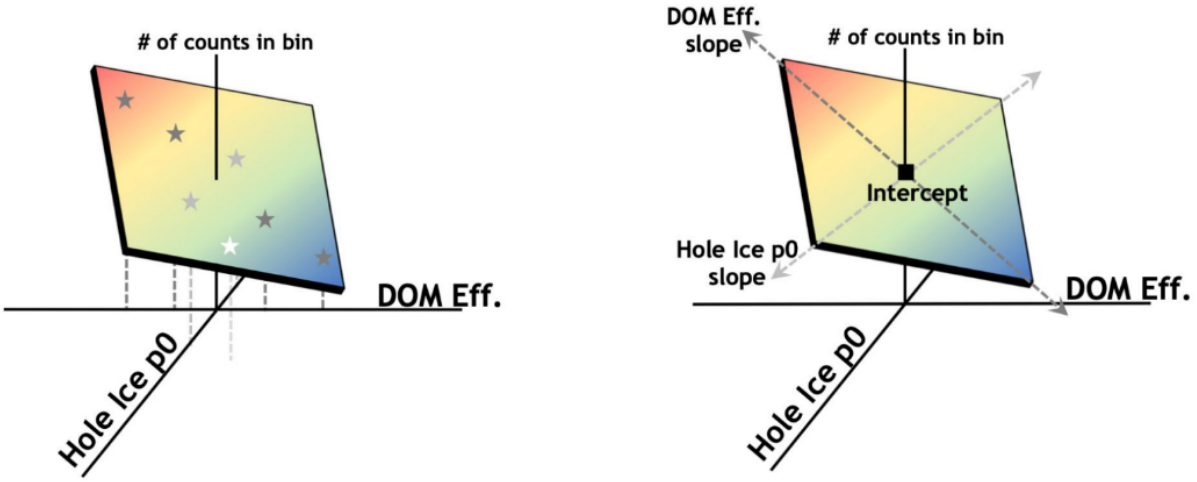

FIGURE 19: An illustration of a hypersurface for one bin. Only two of the parameters are shown for illustrative purposes. Figure provided by supervisor.

5.3.3 Priors

Most of the nuisance parameters are not completely unknown. Their values are either predicted from the theory or are measured already, for instance via calibration methods in the case of detector/ice properties. We thus have a prior knowledge of what they are and within which bounds they should lie. We call the expected value of these parameters the 'nominal' values and the confidence bands the 'priors'. They are shown in Table 2 for all the parameters. The priors are all assumed to be Gaussian and centered around the nominal values. How these are taken into account is described in Section 5.5. On the other hand, some of the nuisance parameters have no priors on them. This is either because they are unknown or because we do not want to bias the result. The latter is the case for the parameters related to the physics of neutrinos, specifically the oscillation parameters.

5.4 Pseudodata

For a statistical analysis, it is useful to be able to generate pseudodata artificially. This is especially true in a case where we do not have access to actual data. To make a pseudo dataset, a template of the expected number of neutrinos for a set of model parameters can be generated. It can be seen as data which is not statistically fluctuated. By applying statistical fluctuations to the template, we obtain a pseudo dataset which looks like an actual dataset would do, if the given model parameters were true. In the case where many particles pass a detector, and their probabilities of interacting are small, the observed bin height can be assumed to be Poisson distributed. Since this is true for neutrino data, Poisson fluctuations are applied to the templates to generate pseodudata.

The unfluctuated pseudodata is however also useful for a statistical analysis, which can be seen as the 'most representative' of repeated experiments if the chosen model parameters are true. It is know as an Asimov dataset and will be used extensively in the various statistical tests performed for this project.

5.5 Fitting procedure

The statistical analysis of this project primarily relies on comparing a histogram of experimental data to a histogram of the MC expectation for a given set of model parameters. A hypothesis can either be compared to real data, to pseudodata, or to a different hypothesis. To quantify how well one histogram agrees with another, we make use of a test statistic. For neutrino data, the bin counts of a histogram can be assumed to be Poisson distributed. If the observed number of neutrinos in a bin is y_i, the Poisson likelihood of a prediction $\lambda_i(\hat{\theta})$, where $\hat{\theta}$ is the parameters of the model, is then:

$$\mathcal{L}(\hat{\theta}, y_i) = \frac{\lambda_i(\hat{\theta})^{y_i} e^{-\lambda_i(\hat{\theta})}}{y_i!}. \tag{41}$$

The full likelihood of observing $\boldsymbol{y} = (y_1, y_2, ..., y_n)$ in all bins can then be found by taking the product of the likelihood for the individual bins:

$$\mathcal{L}(\hat{\theta}, \boldsymbol{y}) = \prod_{i=1}^{n} \frac{\lambda_i(\hat{\theta})^{y_i} e^{-\lambda_i(\hat{\theta})}}{y_i!}. \tag{42}$$

By taking the natural logarithm of the likelihood, the product is turned into a sum. We call this the log-likelihood (or simply LLH), given by:

$$\ln \mathcal{L}(\hat{\theta}, \boldsymbol{y}) = \sum_{i=1}^{n} \ln\left(\frac{\lambda_i(\hat{\theta})^{y_i} e^{-\lambda_i(\hat{\theta})}}{y_i!}\right) = \sum_{i=1}^{n} \big[\ln \lambda_i(\hat{\theta})^{y_i} - \lambda_i(\hat{\theta}) - \ln y_i!\big]. \tag{43}$$

The log-likelihood by itself does not provide any information about how well two histograms agree. However, we know that for a perfect fit $\lambda_i(\hat{\theta}) = y_i$, and thus the log-likelihood value of the perfect fit can then be subtracted to get a modified log-likelihood:

$$\ln \mathcal{L}(\hat{\theta}, \boldsymbol{y})' = \sum_{i=1}^{n} \ln\left(\frac{\lambda_i(\hat{\theta})^{y_i} e^{-\lambda_i(\hat{\theta})}}{y_i!}\right) - \ln\left(\frac{y_i^{y_i} e^{-y_i}}{y_i!}\right) \tag{44}$$

$$= \sum_{i=1}^{n} \big[\ln \lambda_i(\hat{\theta})^{y_i} - \lambda_i(\hat{\theta}) - \ln y_i! - \ln y_i^{y_i} + y_i + \ln y_i!\big] \tag{45}$$

$$= \sum_{i=1}^{n} \big[y_i \ln \lambda_i(\hat{\theta}) - \lambda_i(\hat{\theta}) - y_i \ln y_i + y_i\big], \tag{46}$$

where the last expression is how the log-likelihood is calculated in PISA. For a perfect fit the modified log-likelihood will thus be zero. This fact is useful if we want to compare unfluctuated pseudodata to a hypothesis, in which case a perfect fit can be obtained. For real data a perfect fit is however not expected, because statistical fluctuations are present. The same is true for any kind of fluctuated pseudodata.

The main test statistic used for the analysis is the modified log-likelihood. It will hence just be refered to as the log-likelihood or simply LLH. The larger the value of the log-likelihood is, the better the hypothesis agrees with the data (or pseudodata), and vice versa. The best fit of a model can thus be found by maximizing the log-likelihood as a function of the model parameters, $\hat{\theta}$. By convention, optimization algorithms usually minimize the test statistic. For this reason we choose to minimize the minus log-likelihood, to obtain the set of parameters which gives the best fit of a model to the data.

In addition to the minus log-likelihood, we also take the priors on the nuisance parameters into account. This is done by adding a penalty to the minus log-likelihood, based on how far a fitted parameter is from the nominal value. For all of the parameters which have priors on them, the priors are assumed to be Gaussian and centered around the nominal value with a standard deviation of the so called 'prior'. The penalty is then one half the χ^2 value of how far the fitted value is from the nominal value. This way we get a best fit which takes both the data and prior knowledge of the parameters into account.

The minimization algorithm has been thoroughly investigated in this project, by using Asimov tests (described in Section 5.7), minimizer stability tests (described in Section

5.8), and param ensemble tests (described in Section 5.9). The minimization strategy found to give the best trade-off between speed, stability, and precision uses the `MIGRAD` algorithm in the iminuit Python package [76]. The exact method, and why it was chosen, is discussed in Section 5.8.

5.6 Likelihood scan

The relationship between likelihood and χ^2 values is described by Wilks' theorem [77]. This theorem can be applied in the limit where the Poisson distribution is approximately Gaussian i.e. for high statistics. Since the majority of the bins in the oscNext sample have large bin counts, we will generally assume that Wilks' theorem applies, but also verify if this assumption is good. There is however an additional situation where this theorem breaks down, which is when a parameter is near a boundary [78]. This is the case for Γ_0 and δL_0 since the null hypothesis is $\Gamma_0 = \delta L_0 = 0$ and they can not take negative values. These two parameters are thus specifically investigated in 5.11.

Wilks' theorem states that two times the difference in minus log-likelihood between the best fit hypothesis and a different hypothesis is approximately the difference in χ^2, i.e.:

$$-2\Delta \ln \mathcal{L} = -2(\ln \mathcal{L}(\hat{\theta}, \boldsymbol{y}) - \ln \mathcal{L}(\hat{\theta}_{\text{best}}, \boldsymbol{y})) \simeq \Delta\chi^2. \tag{47}$$

As a result, the statistical properties of χ^2 values also apply to $-2\Delta \ln \mathcal{L}(\hat{\theta}, \boldsymbol{y})$. For instance, it is expected to be χ^2-distributed for repeated experiments, which in turn means that significance (i.e. number of sigma (σ)) for different hypotheses can be calculated. Once the best fit is found, the confidence intervals of the model parameters can thus be estimated. In Table 3 the differences in log-likelihood which correspond to a given number of sigma or percentage for different degrees of freedom (d.o.f.) are shown.

Confidence	d.o.f. = 1	d.o.f. = 2	d.o.f. = 3
1σ	0.5	1.15	1.76
90%	1.35	2.30	3.13
95%	1.92	3.00	3.91
2σ	2.0	3.09	4.01
3σ	4.5	5.91	7.08
4σ	8.0	9.67	11.03
5σ	12.5	14.37	15.91
6σ	18.0	20.04	21.73

TABLE 3: The differences in minus log-likelihood between best fit and a different hypothesis corresponding to the given significances, for different degrees of freedom.

This property can be used to estimate how sensitive the experiment is to the physics parameters of a model. For the $\nu-$VBH cases the parameter of interest is Γ_0. Since we are investigating the sensitivity of only one parameter, the d.o.f. is one. Here we find an initial proxy for the sensitivity, which does not include any fits of the nuisance parameters. It however allows us to compare the sensitivities of the models to each other, and it provides

us with reference values for later use. A full computation of the sensitivities is given later in Section 5.10 and 5.11.

First, an Asimov set is generated with all parameters set to the null hypothesis, e.g. no decoherence. Since no statistical fluctuations are applied to the Asimov set, the best fit is then a template with $\Gamma_0 = 0$. Now, templates with different values of Γ_0 can be created and their log-likelihoods can be compared to the best fit. By performing a scan in the parameter value of the template, the confidence intervals of Γ_0 if no signal is present can be calculated. This has been carried out to estimate 5σ confidence intervals of Γ_0 for values of n going from 0 to 4. The value of E_0 was specifically set to 1 GeV when performing the scan. The value of Γ_0 can however easily be converted to any other E_0 with $\Gamma_0(E_{0,\text{new}}) = \Gamma_0(E_{0,\text{old}})(E_{0,\text{new}}/E_{0,\text{old}})^n$. The result of one scan (state selected $n = 2$) is thus shown for $\Gamma_0(300\text{GeV})$ in the left panel of Figure 20, and the 5σ sensitivities for all values of n are shown in the right panel. This reference energy was chosen because 300 GeV is the highest reconstructed neutrino energy in the sample, and neutrinos around this energy contribute a lot to the sensitivity (see e.g. Figure 14).

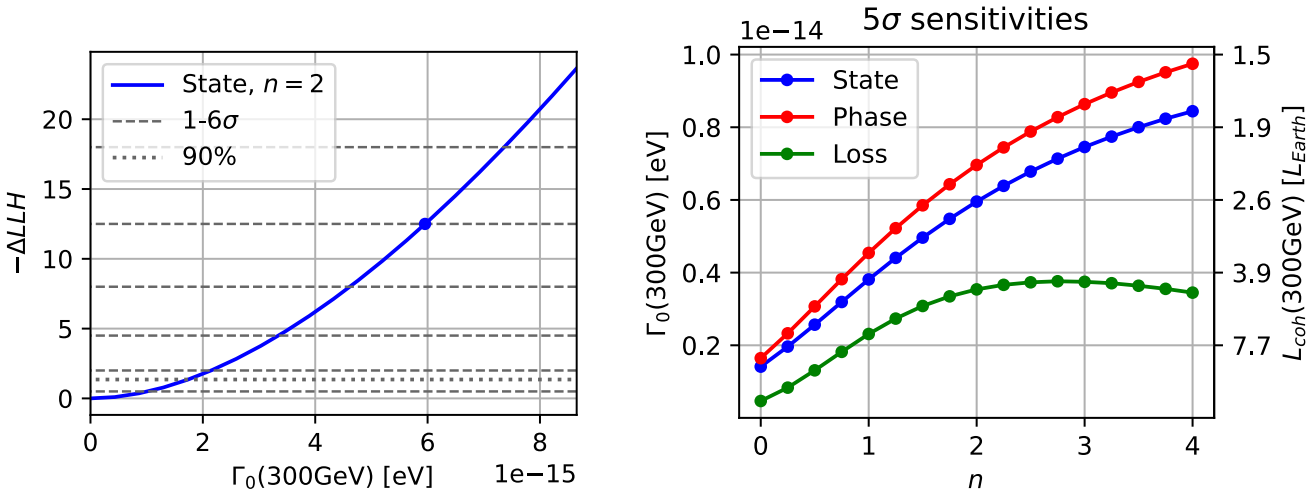

FIGURE 20: Left: The result of the log-likelihood scan for the state selected ν-VBH scenario with $n = 2$ and with $E_0 = 300$ GeV. Dashed lines are shown for the minus log-likelihood values which correspond to 1σ (bottom line) to 6σ (top line). The 5σ line is used to estimate the 5σ sensitivity of this model. Right: Estimations of 5σ sensitivities of Γ_0 with $E_0 = 300$GeV for the state selected, phase perturbation, and netrino loss $\nu-$VBH interaction models for many different values of n. For these estimates the nuisance parameters have not been fitted and the real sensitivities are thus expected to be worse (see Section 5.10).

Although the nuisance parameters have to be fitted to obtain correct sensitivity estimates, the values of Γ_0 in Figure 20 still tell us a lot about the models. The figure indicates that the experiment is most sensitive to the neutrino loss model and and least sensitive to the phase perturbation model. The state selected model lies somewhere in between but is closest to the phase perturbation model. This is consistent with the oscillograms shown in Figure 14, as the effect caused by the same value of Γ_0 is strongest for neutrino loss and weaker for the two other models. The state selected effect is also

just slightly stronger than the phase perturbation. In addition to this, the 5σ sensitivities found here define what regions of phase space should be investigated in later statistical tests. Finally, they are also used for comparison in Section 6.1 when investigating the results of the complete sensitivity tests which include fitting.

It is also important to note, that the shape of the sensitivities shown in Figure 20 is very dependent on where E_0 is, relative to the energy range of the data. If E_0 is below the energy range, the sensitivity of $\Gamma_0(E_0)$ decreases exponentially as a function of n. Conversely, if E_0 is above the energy range, the sensitivity of $\Gamma_0(E_0)$ increases exponentially as a function of n. If however E_0 is inside or close to the energy range, the sensitivities can both increase and decrease as a function of n, as seen in 20.

A similar scan for the ligthcone fluctuations models has not been carried out in systematic way and is thus not shown. Instead trial and error was used to estimate rough 5σ reference values of δL_0 for later use.

5.7 Asimov tests

One of the simplest tests to verify that the minimzation process works is called an Asimov test, also known as an 'inject-recover test'. Here an Asimov dataset is generated for a given set of 'true' values of the model parameters. The model can then be fitted to the Asimov set, which should result in a perfect fit, because no statistical fluctuations are applied. We carry out this test for a range of true values of Γ_0 and δL_0 for the different models and values of n. The chosen ranges are based on the 5σ limits found in Section 5.6. By investigating if the fit is perfect in all cases, we ensure that we can fit the physics parameter of interest regardless of where its true value is in the given range.

The result of the Asimov tests for the ν-VBH state selected case with $n = 2$ is shown in Figure 21. The left panel shows that Γ_0 seems to fit exactly at the true values in all cases. In the right panel however, the differences between the fitted and the true values are plotted, which shows a small deviation. The deviation is however expected since the precision of the minimizer is finite, and the resulting uncertainty is too small to have any significant impact on the analysis. In addition to the physics parameters, all nuisance parameters are fitted and they also converge at approximately the true values.

Many Asimov tests with different combinations of the models and values of n have been performed and visually investigated in a similar way. For the minimizer using the `MIGRAD` algorithm, they were all successful.

5.8 Minimizer stability test

When performing a fit, the minimizer is given an initial guess of the model parameters. In an ideal case the minimizer is able find the correct minimum in the minus log-likelihood space, regardless of what the initial guess was. To test this, we generate an Asimov dataset for one set of true values of the parameters which go into the calculations. The initial guess of all parameters which are free in the fit is then randomized and a fit is performed. This process is repeated for many different realizations of the randomized parameters. Like with the Asimov test, all parameters in the fit are expected to converge at the true values. In addition, the fitted template is expected to fit the asimov data almost perfectly

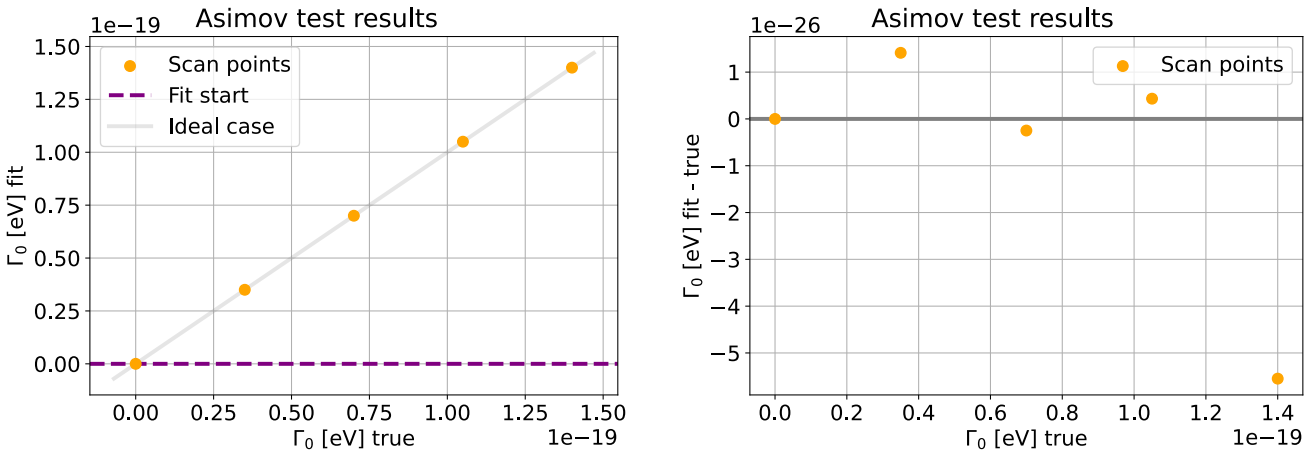

FIGURE 21: Left: Asimov tests of the ν-VBH state selected case with $n = 2$ and $E_0 = 1$ GeV. The orange points in the left plot are the fitted values of Γ_0, whereas in the right plot they represent the differences between the fits and true values.

for every trial, and the minus log-likelihood should thus be close to zero. This way the stability of the minimizer can be verified.

Initially, the minimizer used for the analysis was an implementation of an algorithm named L-BFGS-B [79] in the python library SciPy [80]. The minimizer stability test for this method however revealed a severe problem. A selection of the fitted parameters for 100 trials of the test for the ν-VBH state selected model and this minimizer is shown in Figure 22. It can be seen that the distribution of fitted values is bimodal for most parameters, and that one of these modes is away from the true parameter value. This is a clear indication that the minimization process is not working as it should.

After a thorough investigation, it was found that the problem was related to the parameter θ_{23}. The minus log-likelihood has two minima in this parameter. If neutrino oscillations are simplified to two flavors, one of the minima is at the true value of θ_{23} and the other is exactly mirrored around 45 degrees. As a result, there is a local maximum of the minus log-likelihood at 45 degrees. For three flavor neutrino oscillations however, the reflection point is only close to 45 degrees[2] and the true value is slightly preferred from the other minimum.

Parameter spaces with local minima are notoriously difficult for minimizers to navigate, because they can get stuck at local minima. An attempt at avoiding this problem was already present in the code, called an 'octants fit'. This method makes a cut at exactly 45 degrees and fits each part (octant) of the parameter space separately with L-BFGS-B and keeps the best fit. As can be seen from Figure 22, this did not ensure that the correct minimum was found. The reason is that the cut at 45 degrees is slightly different from the actual maximum of the minus log-likelihood at the reflection point[3]. An illustration of the minus log-likelihood space is shown in Figure 23. Here it can be

[2]This depends on the other mixing parameters. Specifically if θ_{13} is small, the reflection point is close to 45 degrees.

[3]The point called a reflection point here is technically not a reflection point for three flavor oscillations. It is however called that for simplicity.

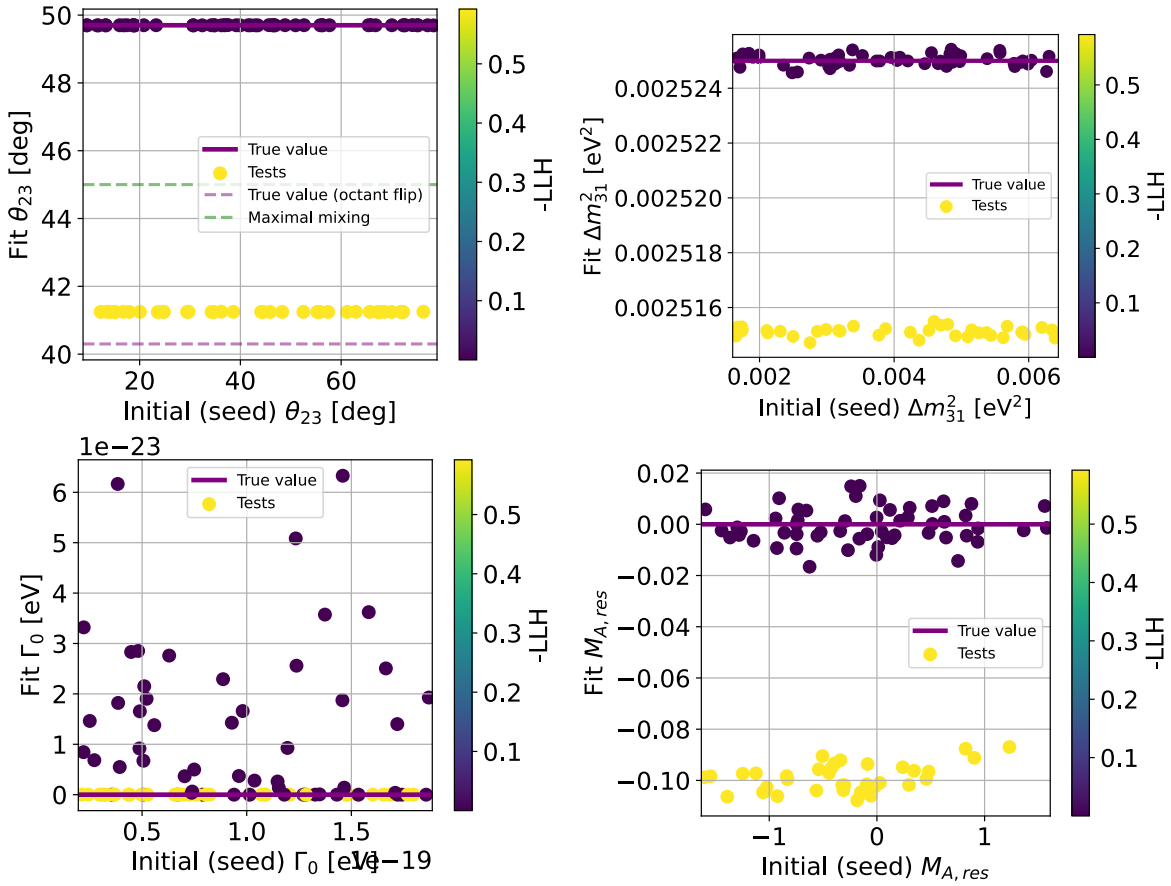

FIGURE 22: A selection of the fitted parameters for 100 trials of the minimizer stability test for the ν-VBH state selected model with $n = 2$ and $E_0 = 1$ GeV. The minimizer used is L-BFGS-B with an octants fit as described in the text.

seen that a small local minimum is created between the reflection point and 45 degrees when a cut in the parameter space is placed at 45 degrees. It thus creates an additional local minimum where the minimizer can get stuck. By investigating how the L-BFGS-B algorithm moves through the parameter space, it was seen that it has a tendency of trying out its edges. When the edge is a local minimum it is thus likely to think that it has found the correct minimum.

The first attempt at solving this problem was to tune the parameters of the L-BFGS-B algorithm to potentially increase its stability. This however, did not improve the results. Instead, a solution was reached by switching to a different minimizer. Several algorithms were tested, and the one settled on was the `MIGRAD` algorithm in the iminuit Python package [76]. It was noticed that this minimizer takes less extreme jumps in the parameter space than L-BFGS-B and is thus less likely to end at the edges of the parameter space. Additionally, a method called recursive minimization was used, where several consecutive minimizations are run, which use the result of the previous fit as the starting point for the next fit. Specifically, we chose the first fit to be low precision without the octant cut. The purpose of this fit is to roughly approach one of the minima without any risk of getting stuck at 45 degrees. Subsequently, the octants fit is used which splits the fit into

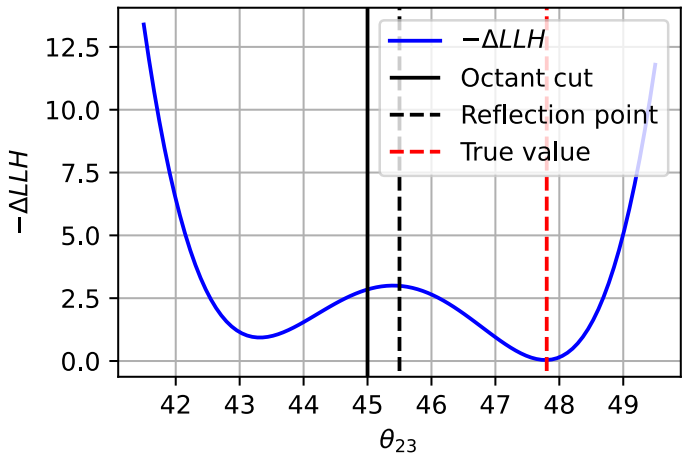

FIGURE 23: An illustration of the minus log-likelihood as a function of θ_{23} for three flavor neutrino oscillations. Its functional form is made up but resembles the actual log-likelihood.

each of two octants. It then uses the reults of the first fit (except θ is reflected around 45 degrees for one of the fits) to continue the minimization toward both minima. Since `MIGRAD` takes smaller steps in the parameter space than L-BFGS-B, and that the fit does not start from scratch when fitting each octant, the minimizer is less likely to jump to the local minimum at 45 degrees. The octant fits are then configured to be more precise than the first fit to obtain a good fit for both octants. When the two minima of the minus log-likehood space are found, the best of the two fits is kept, and the other discarded. The result of the minimizer stability test with this strategy is shown in Figure 24.

The results show a large improvement from the previous strategy, since most trials find the correct minimum. There are however still 8 out of the 100 trials where the wrong octant is found. When the fit is performed to real data, a way to circumvent this problem would be to repeat the fit several times with different initial guesses of the parameters and keep only the best fit. The risk of all fits finding the wrong octant will then be negligible.

Furthermore, a third minimizer strategy was tried, which also uses recursive minimization and a combination of `MIGRAD` and two algorithms called `CRS2` [81, 82, 83] and `Subplex` [84], both from the python library NLopt [85]. First, a fit with no octant cut is performed using `CRS2`. It is then split into the two octants, and in each a low precision `Subplex` fit is then performed. Finally, a high precision `MIGRAD` fit is used to find the best fit in each octant, only keeping the best. This strategy has even better performance than the previous method in the minizer stability test, with almost no octant flips. The fitting time was however significantly increased, and the strategy was thus deemed too impractical for the early stages of this analysis, where trouble-shooting and trial and error are common. Instead, the strategy with recursive `MIGRAD` fits is used for the rest of this thesis. It is however worth considering using the more robust strategy in the future, once the entire analysis is in place and real data will be considered.

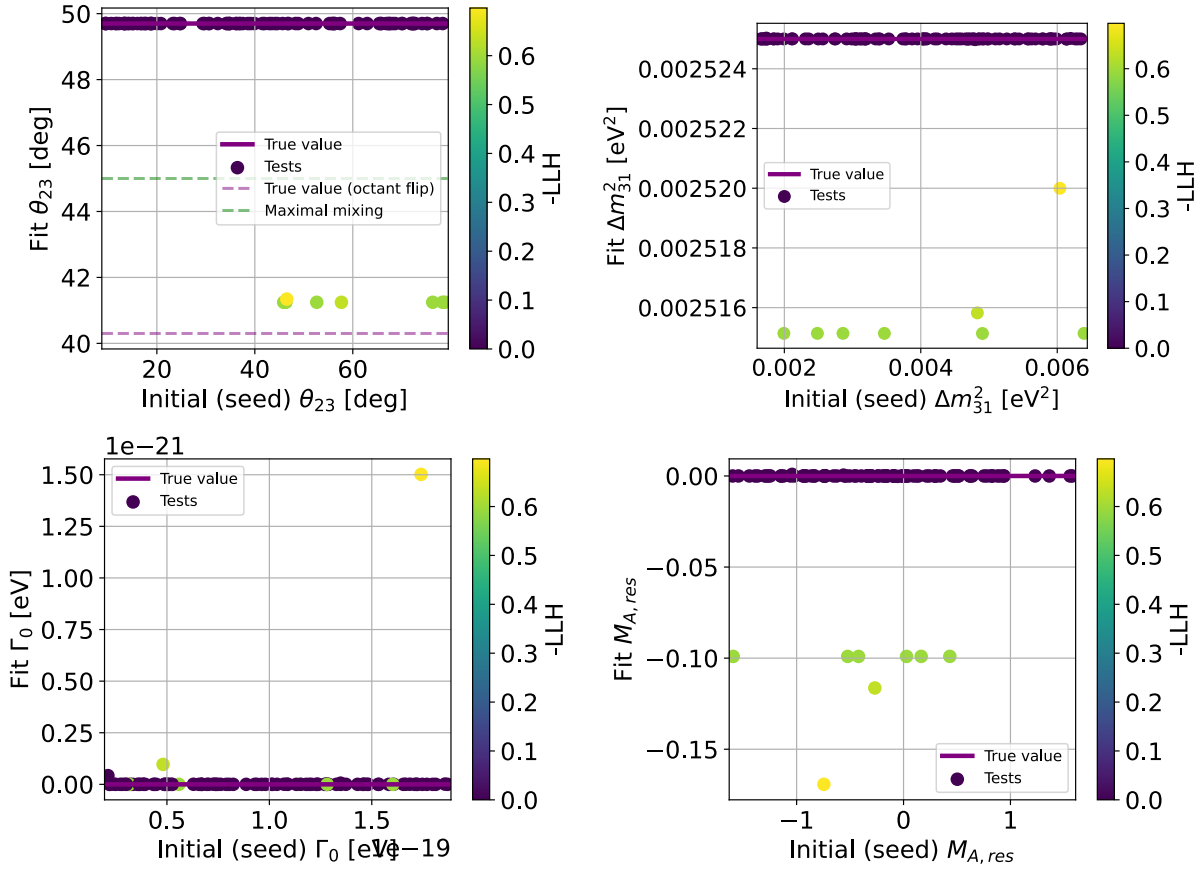

FIGURE 24: A selection of the fitted parameters for 100 trials of the minimizer stability test for the ν-VBH state selected model with $n = 2$ and $E_0 = 1$ GeV. The minimizer used here is a recursive iminuit fit which is described in the text. This figure is the same as Figure 22 but with an improved minimizer strategy.

5.9 Param ensemble test

The param ensemble test takes a different approach to testing the robustness of the minimizer. In this test, the true values of the free parameters are randomized and an asimov set is generated with this set of parameters. A fit is then performed which should return the true values of the parameters which do not have a prior on them. Since the priors are kept at the nominal values and not at the true values, the fit will get a penalty if it moves a parameter too far away from its nominal value. The optimal value of the test statistic is thus obtained somewhere between the nominal and the true value of that parameter. This process is repeated for many different realizations of the randomized true parameter values, and can be seen as a more thorough version of the asimov tests performed in Section 5.7. It allows us to verify that the minimizer can find the correct minimum, regardless of what the true values of the parameters are. A selection of the fitted parameters from param ensemble test is shown in Figure 25 for 100 trials of the ν-VBH state selected model with $n = 2$.

The figure shows that for the important physics parameters, θ_{23}, Δm_{31}, and Γ_0, almost all of the fits return the true values of the parameters. There is one point however which

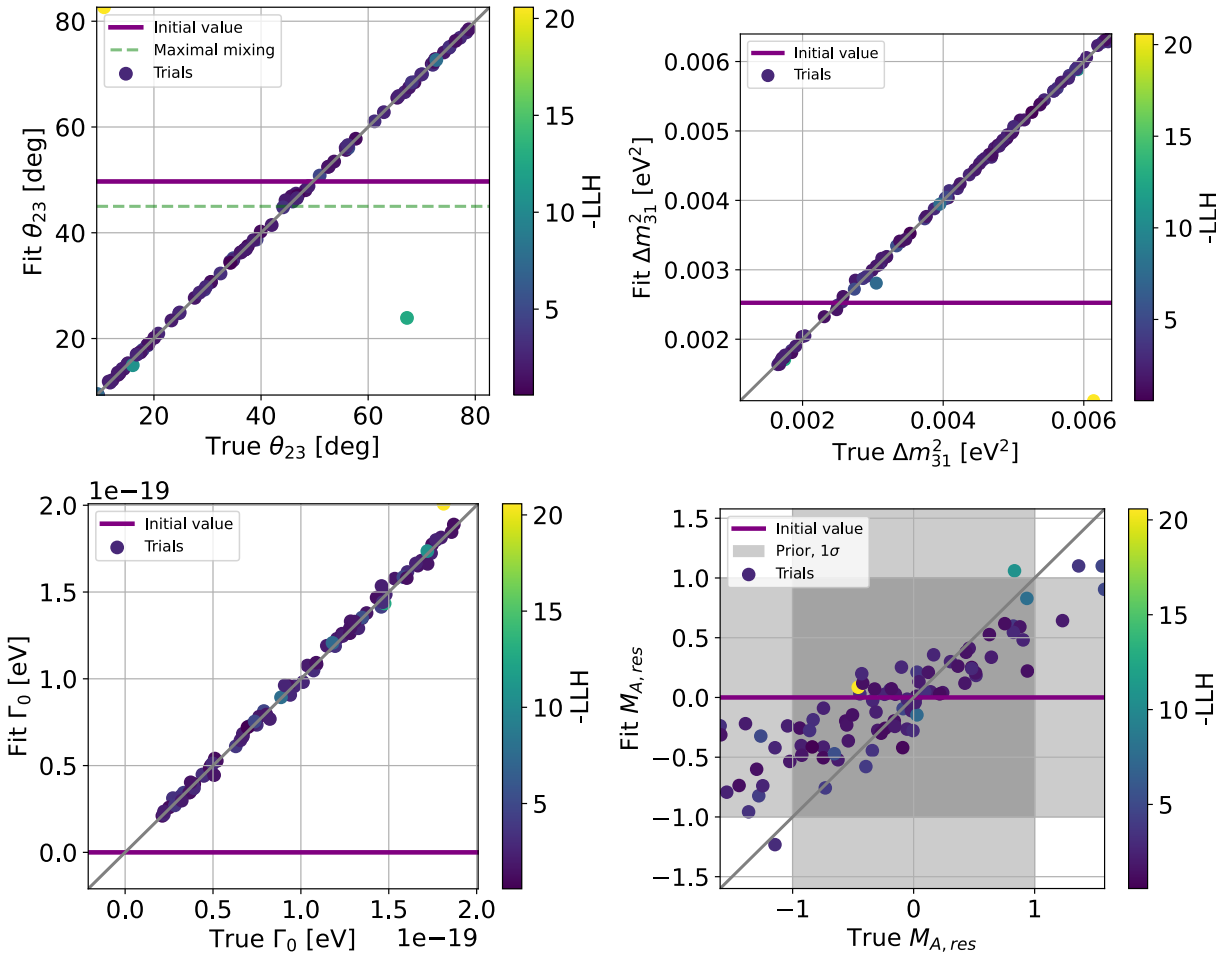

FIGURE 25: A selection of the fitted parameters for 100 trials of the parameter ensemble test for the ν-VBH state selected model with $n = 2$ and $E_0 = 1$ GeV.

is off in the θ_{23} plot. This is a fit which has found the wrong octant and is thus consistent with the problems seen in the minimizer stability test. Note that there is also one yellow point which is completely off in both the θ_{23} and Δm_{23} plot. Since this has only happened one out of 100 times, it is not considered a problem.

The plot of fitted values of the systematic parameter $M_{A,\text{res}}$ shows a much wider distribution. It is however characteristic for many of the nuisance parameters in a test like this. It indicates that the analysis has very limited sensitivity to this parameter. In this case the prior has a influences the fit, and the optimal parameter value is found between the nominal and true value (to within minimizer precision). Additionally, the minus log-likelihood is not expected to be zero in this test. Since the best fit of the parameters are not at the nominal values, the priors add substantial penalties to the minus log-likelihood. This can be seen from the colors of the dots not being in the deep blue region.

This test shows that the minimizer generally works well. It will thus used in the following tests to estimate the sensitivities of the oscNext sample to the models considered in this project.

5.10 Sensitivity test

Now that the we have have a minimizer that works, the sensitivity of the oscNext sample to the model parameters can be estimated including fits of the nuisance parameters. This provides more realistic sensitivities than the log-likelihood scans performed in Section 5.6. Just like described in that section, an Asimov set is generated with all nuisance parameters set to the nominal values and the physics parameters (Γ_0 and δL_0) set to zero. The specific physics parameter is then pulled to a given value in the template, and a fit is performed with this parameter fixed. The obtained minus log-likelihood can then be compared to a fit where the physics parameter is free (which for an Asimov set should give a perfect fit to within minimizer), which provides a significance for the given value of the physics parameter. The process is repeated for 10 linearly spaced values of the physics parameter, which gives a minus log-likelihood curve like the left panel of Figure 20, but with fitted nuisance parameters. By using interpolation, the value of the parameter which results in a given significance can then be found. The result of the sensitivity test for the ν-VBH state selected model with $n = 2$ is shown in Figure 26. The test shows for instance that the 90% confidence limit of this scenario is $\Gamma_0(1\text{ GeV}) \sim 2.1 \times 10^{-20}$ and the 5σ confidence limit is $\Gamma_0(1\text{ GeV}) \sim 8 \times 10^{-20}$.

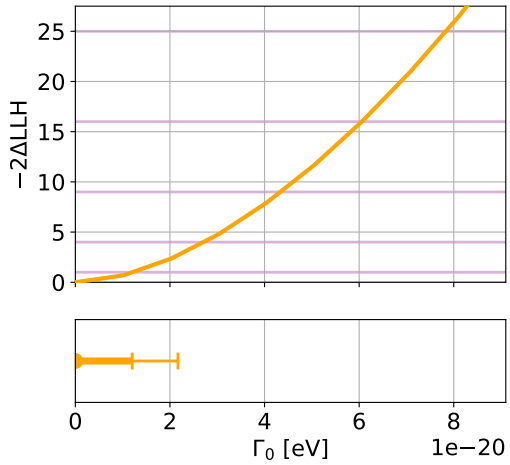

FIGURE 26: Sensitivity test for the ν-VBH state selected model with $n = 2$. The value of Γ_0 shown is for $E_0 = 1$ GeV. Horizontal lines have been added which correspond to 1σ (bottom) to 5σ (top, exactly on $-\Delta LLH = 25$). The bottom panel shows the 1σ and and 90% confidence limits.

As stated all of the nuisance parameters have been fitted for all 10 values of $\Gamma_0(1\text{ GeV})$ in the scan. We can thus investigate what values the nuisance parameters have pulled to, which reveals the parameters that can compensate for Γ_0 being fixed away from the true value, i.e. how correlated they are with Γ_0. Two of the nuisance parameters are shown in Figure 27. The plots indicate that the parameters Barr, y_{K^-} and DIS are correlated with Γ_0, and thus have a significant impact on the sensitivity. These two parameters change the high E upgoing muon neutrino flux, which is where the decoherence signal is for $n > 0$ (see e.g. Figure 14). The pulls are generally expected to grow somewhat linearly as a function of Γ_0. They are however pulled toward nominal values by the priors, and

this effects increases the further the parameter is away from the nominal value. This is consistent with what is seen in the figure.

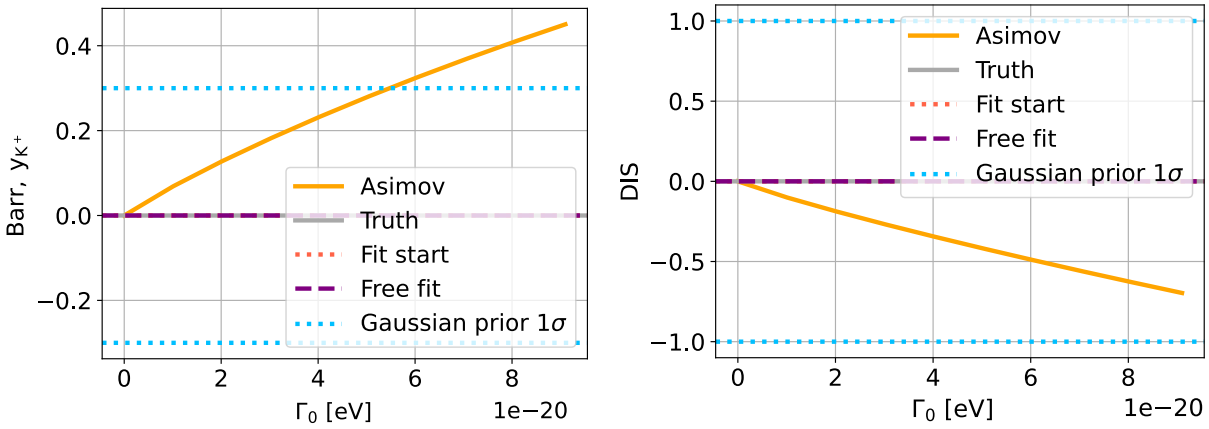

FIGURE 27: The pulls of two of the nuisance parameters for the sensitivity test of the ν-VBH state selected model with $n = 2$. These are some of the strongest pulls of all the nuisance parameters in this test.

The sensitivity test has been systematically performed for the ν-VBH state selected, phase perturbation, and neutrino loss models, and lightcone fluctuations with $m = 0.5$ (uncorrelated distance) and $m = 1$ (velocity fluctuations). The values of n range from -2 to 4 in integer steps for the ν-VBH cases and -1 to 3 for the lightcone fluctuations cases. The lightcone fluctuation cases with $n = -2$ and $n = 4$ was left out because the calculations took too long to run. This gives a total of 31 sensitivity tests and their results are discussed in Section 6.

5.11 Ensemble test

Up until now, we have only considered asimov data, i.e. data where a perfect fit can be obtained. The ensemble test however introduces statistical fluctuations to the pseudo-data. In this test a given true set of parameter values are chosen and an asimov dataset is generated with those parameters. By assuming that the bin counts are Poisson distributed, we can statistically fluctuate every bin in the dataset. This is done by pulling a random value from a Poisson distribution centered around the bin count for every bin in the asimov set. The statistically fluctuated pseudo dataset then gives a realistic example of what a real data could look like. If a fit is performed, we do not expect to obtain the true parameters, because the statistical fluctuations can shift where the minimum in the minus log-likelihood space is. By repeating this process, we can thus simulate carrying out the experiment many times. The method is also called bootstrapping, and it tells us what the distributions of the fitted parameters and the test statistic would be, if the experiment was to be repeated many times. When a fit to real data is performed, these distributions then tell us if the result is consistent with the null hypothesis.

The test has been performed for 500 realizations (trials) of the statistically fluctuated pseudodata for the ν-VBH state selected model with $n = 2$. A selection of the distributions

of the fitted parameters is shown in Figure 28. These are expected to be approximately Gaussian, which can be seen is the case for Δm^2_{23} and $M_{A,res}$ as shown in the figure. Similarly, it has been checked that the rest of the nuisance parameters, not shown in the figure, are also approximately Gaussian. There are however two exceptions to this expectation; the distributions of θ_{23} and Γ_0 which are shown in the top left and bottom left panel of Figure 28. The shape of the distribution of the fitted θ_{23} values has two distinct peaks, and one of them is on the 'wrong' side of 45 degrees. As discussed in Section 5.8, the minus log-likelihood has two distinct minima in θ_{23} (see 23). The statistical fluctuations change the shape of the minus log-likelihood space and can result in the minimum in the wrong octant being a better fit than the one at close to the true value of θ_{23}. It is thus expected that some of the best fit values are in the wrong octant when statistical fluctuations are applied.

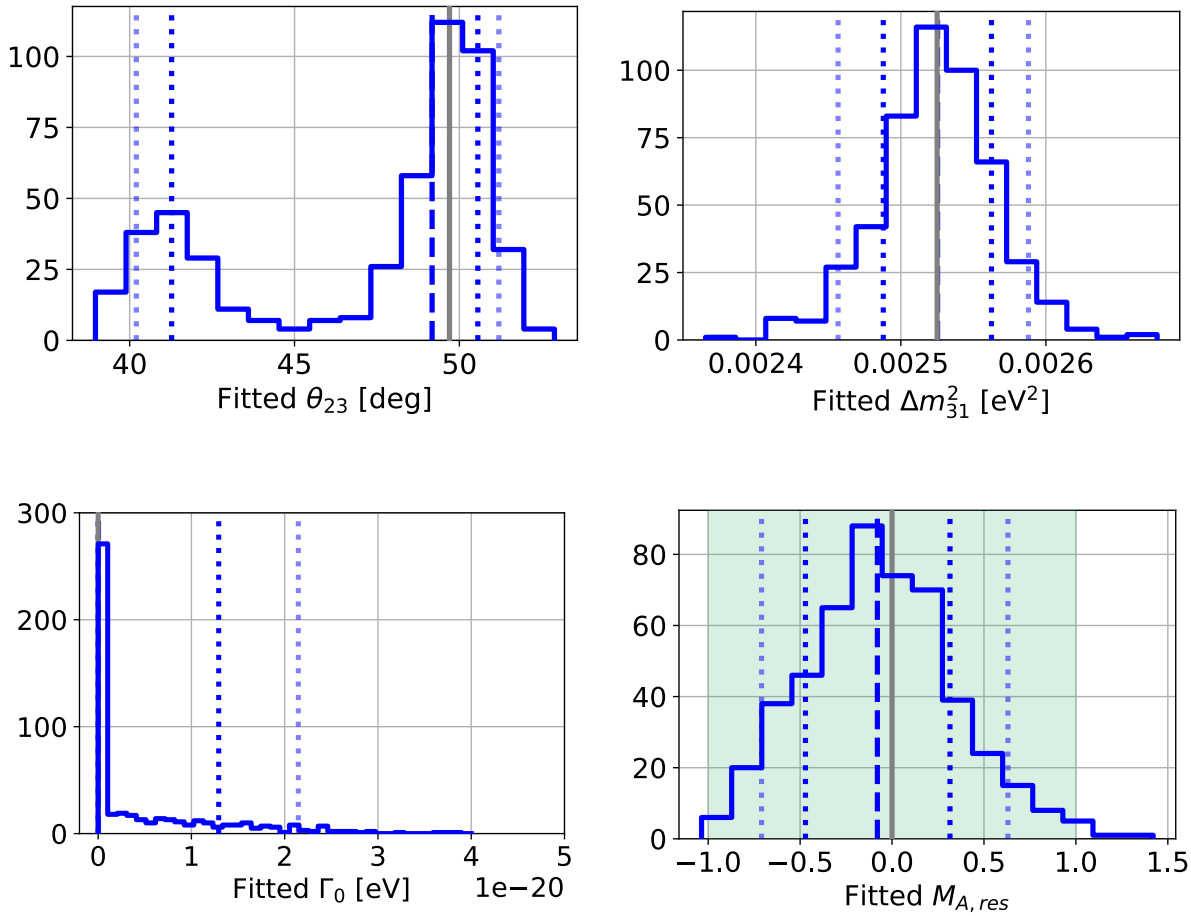

FIGURE 28: A selection of the fitted parameters for 500 trials of the ensemble ensemble test for the ν-VBH state selected model with $n = 2$ and $E_0 = 1$ GeV. The vertical lines show the true (solid), mean (dashed), 1σ (dotted blue), and 90% (dotted gray) values.

5.11.1 Distribution of Γ_0

Since Γ_0 is the main parameter being measured in this analysis, it is important that we investigate its distribution in more detail. From the lower left panel of Figure 28, it can be seen that close to half of the 500 trials are at $\Gamma_0 = 0$. This feature is caused by a combination of several things. In the fit, we do not allow Γ_0 to go below 0, because negative decoherence is unphysical. However, the statistical fluctuations might cause a value of $\Gamma_0 < 0$ to actually fit the pseudodata best, e.g. if the statistical fluctuations have resulted in a small excess of upgoing neutrinos. If this is the case, the minimizer will end at $\Gamma_0 = 0$, because it is the closest it can get to the actual best fit. Having a cut in the parameter space can thus result in a pile up. Additionally, if we assume that the actual best fits are symmetrically distributed around the true value, which in this case is $\Gamma_0 = 0$, then exactly half of the fits (to within statistical uncertainty) will pile up at $\Gamma_0 = 0$. This is what we see for Γ_0 in Figure 28, and it is not a problem if treated correctly.

We can now investigate if Wilk's theorem applies to this parameter, and if the sensitivity tests are consistent with the ensemble test. The sensitivity test assumes that Wilk's theorem applies and gives a 'confidence' for any value of Γ_0 in the scan range. The confidence is the probability of measuring this parameter inside the given value of Γ_0 when a fit to data is performed (assuming the parameters used to generate the pseudodata are true). The 'confidence limit' is then the value of Γ_0 which corresponds to a given confidence, e.g. 90%, 95%, e.t.c. We can then compare the sensitivity test to the ensemble test, since the ensemble test gives the actual distribution of the parameter. This is done by counting how many of the fitted values are below a given Γ_0 and divide it by the total number of trials. The resulting fraction should agree (if Wilk's theorem applies) with the confidence of the same value of Γ_0 obtained in the sensitivity test. The 90% confidence limits found in the sensitivity test and ensemble tests are shown in Figure 29 as vertical lines on a zoom in of the distribution of fitted values of Γ_0. Here it can be seen that the confidence limits from the sensitivity and ensemble test do not agree.

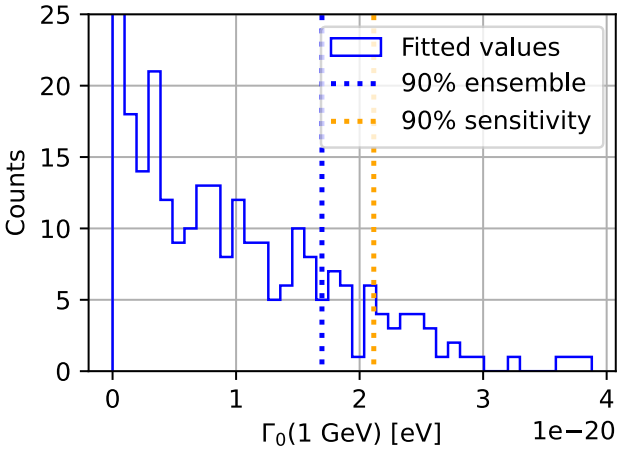

FIGURE 29: The fitted values of Γ_0 for 500 trials of the ensemble test for the ν-VBH state selected model with $n = 2$. This is the same as the bottom left of Figure 28 but zoomed in and shown alongside the 90% confidence limits from the ensemble and sensitivity test.

To investigate why the two tests do not agree, a more thorough comparison of the confidence obtained from the sensitivity and ensemble tests can be made. By going through a finely spaced grid of Γ_0 values, we can get the confidence the entire range according to both methods. The result is shown in the left panel of Figure 30, which we can use to assess what is going on. It can be seen that the blue line (ensemble test) jumps immediately to 50%, which makes sense because half of the fits are at $\Gamma_0 = 0$. The orange line (sensitivity test) on the other hand does not have this feature. Adittionally, the orange line grows faster toward 100% than the blue line. The reason for this is that the sensitivity test does not take into account that half of the fits are at $\Gamma_0 = 0$. Additionally, the sensitivity test assumes that we are looking at both sides of the distribution, i.e. both negative and positive Γ_0. In this case however, everything below 0, even what would normally be outside a confidence interval, gets placed inside the confidence interval at $\Gamma_0 = 0$. The distribution is thus one-sided and not two-sided as assumed in the sensitivity test. The conversion from a log-likelihood to a confidence is then:

$$c_{\text{corrected}} = \frac{1}{2} + \frac{1}{2}\text{cdf}(-2\Delta \ln \mathcal{L}), \tag{48}$$

where $c_{\text{corrected}}$ is the 'corrected' confidence and cdf is the cumulative distribution function of a χ^2 distribution, which is what normally is used to calculate a confidence from a log-likelihood. The first 1/2 in Equation 48 comes from half of the distribution being at $\Gamma_0 = 0$, and the second 1/2 takes into account that we only look at one side of the distribution. The corrected confidence is shown in the right panel of Figure 30 and gives a good agreement with the ensemble test. It will thus be applied to the sensitivity tests in the rest of this thesis to estimate the sensitivity of the oscNext sample to the models.

The robustness of the approach discussed here has been investigated in Section C. The results indicate the method works well for most cases, except only partially for lightcone fluctuations with $m = 0.5$. It is however still an improvement and have thus been chosen to be applied (see C for details).

5.11.2 Goodness of fit

Finally, the ensemble test can be used to estimate the how well a fit agrees with the data. By repeating the experiment we have obtained 500 values of the minus log-likelihood. The distribution for the 500 trials is shown in Figure 31. It is generally considered to be approximately Gaussian, which we can see is the case here. If it is assumed that the parameters used for the Asimov set are true, then a fit to real data should give a minus log-likelihood within this distribution. If the minus log-likelihood is larger than the distribution, the hypothesis does not fit the data well. If however it is smaller, the model fits the data too well. By counting the number of values above a certain minus log-likelihood and dividing by the number of trials (500), we get a p value corresponding to that minus log-likelihood. This way the goodness of fit of the fitted hypothesis can be quantified. The p-value at which a hypothesis is rejected has to be decided upon before the fit performed. The exact value is arbitrary, but often a few percent is chosen.

As stated, the distribution of minus log-likelihood values depends on the assumed true values of the parameters used for the pseudodata. When a fit to real data has been performed, the ensemble test should thus be run again, this time with the best

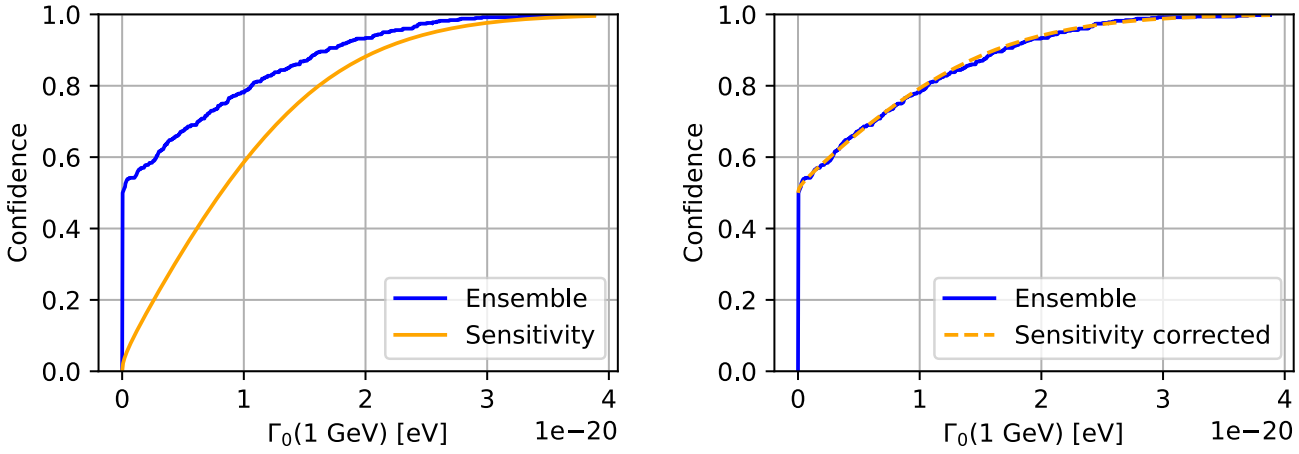

FIGURE 30: Left: The confidence for a range of $\Gamma_0(1\text{ GeV})$ according to both the ensemble and sensitivity tests. The confidence is the probability of finding $\Gamma_0(1\text{ GeV})$ below a given value, if a fit is performed to statistically fluctuated data. Right: Same as Left but with the modified confidence for the sensitivity test, which is discribed in the text.

fit parameters as the assumed true values. This approach then gives a more accurate estimation of the goodness of fit.

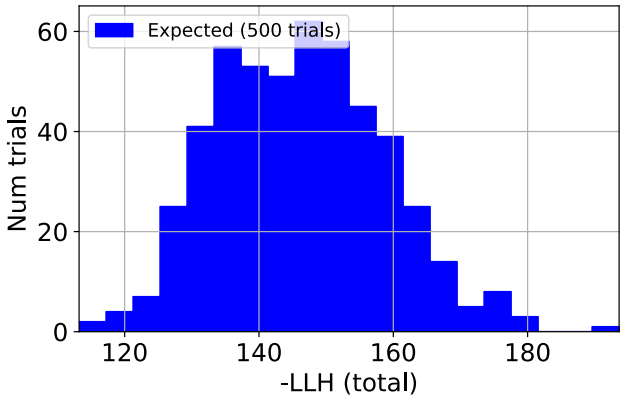

FIGURE 31: The distribution of minus log-likelihood (-LLH) values for 500 trials of the ensemble ensemble test for the ν-VBH state selected model with $n = 2$.

6 Results and discussion

The sensitivity of the oscNext sample to the decoherence models considered in this project has been found for many different values of the energy-dependence parameter, n. We can now assess the results and compare the sensitivity of each model to each other. Additionally, the sensitivities found here can be compared to limits set by previous studies of decoherence.

6.1 Comparisons of model sensitivities to each other

In Figure 32 the 90% confidence limits of the ν-VBH models are shown expressed as $\Gamma_0(100\text{GeV})$ and $\Gamma_0(300\text{GeV})$. The significance of 90% is chosen for consistency with later figures, and the values of E_0 make it easy to visually compare the results.

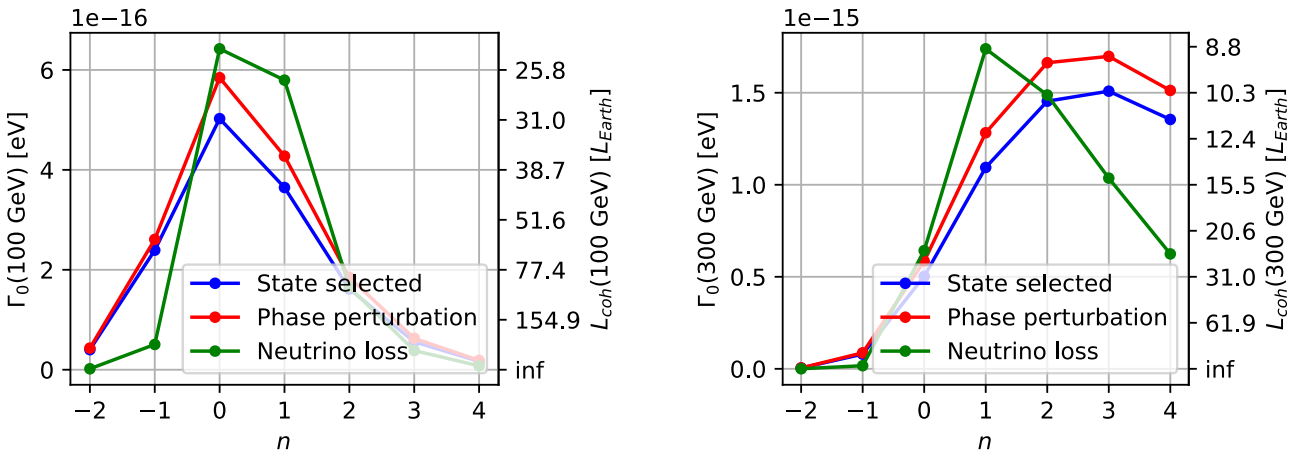

FIGURE 32: 90% confidence limits for the ν-VBH interaction models expressed as $\Gamma_0(E_0)$ for two different E_0. On the second y-axis of each plot, the corresponding coherence lengths are shown in earth diameters.

For high values of n we see that the sensitivities of the three models are ordered like they were in the scan without fitting (Figure 20). The sensitivity is thus strongest for the neutrino loss model and weaker for the state selected and phase perturbation models.

For $n = 0$ and 1 however, the sensitivity to the neutrino loss model is weaker than the other models. The neutrino loss model results in a deficit in upgoing neutrinos across all energies, whereas the other two models gives both excesses and deficits. For $n = 0$ and 1 the neutrino loss scenario is thus correlated with some of the nuisance parameters which can counteract the deficit. By looking at the nuisance parameter pulls of the $n = 0$ sensitivity tests, it was found that the overall neutrino normalization and the flux spectral index ($\Delta\gamma_\nu$, which can be seen as a energy-dependent normalization) were being pulled (shown in Figure A.3). It is therefore surprising that the sensitivity to this model is significantly decreased for $n = 0$ and 1.

For negative values n the sensitivity is again best for the neutrino loss model, which can also be explained. When n is negative, the damping is strong at low energies. The

state selected and phase perturbation models only dampen neutrino oscillations (see e.g. Figure A.1), which might be a difficult signal detect at low energies where the energy reconstruction is imprecise and the binning is coarse compared to the oscillation patterns. On the other hand, the neutrino loss model causes a deficit of neutrinos at low energies for negative n, which is an easy signal to detect, since the statistics is very high at low energies. This results in a strong sensitivity to the neutrino loss scenarios with negative n.

Figure 32 also shows the coherence lengths corresponding to the sensitivities of $\Gamma_0(E_0)$. For instance, in the $n = 2$ case the sensitivity to the coherence length of a 300 GeV neutrino is around 10 Earth diameters for all three models. In the ν-VBH cases the coherence length is equal to the mean free path of a neutrino interacting with a VBH. The oscNext sample will thus be able to 'see' if a 300 GeV neutrino on average interacts with a virtual black hole once every 10 Earth diameters.

A similar comparison is difficult to make for the lightcone fluctuations models. The same value of δL_0 produce extremely different damping strengths for different values of m. In addition, the energy-dependence of the coherence lengths depend on both n and m, and can not easily be compared.

6.2 Sensitivity to Planck scale physics

As discussed in Section 3.7, the fundamental parameters of the considered models, Γ_0 and δL_0, can be re-expressed relative to the Planck scale and compared to 'natural' expectations. The sensitivities (at 90% confidence) of the oscNext sample to the parameters ζ_{Planck} and δL_{Planck} for the tested scenarios are shown in Figure 33. Here we have chosen not to include negative values of n, because quantum gravity theories generally predict effects which increase with energy.

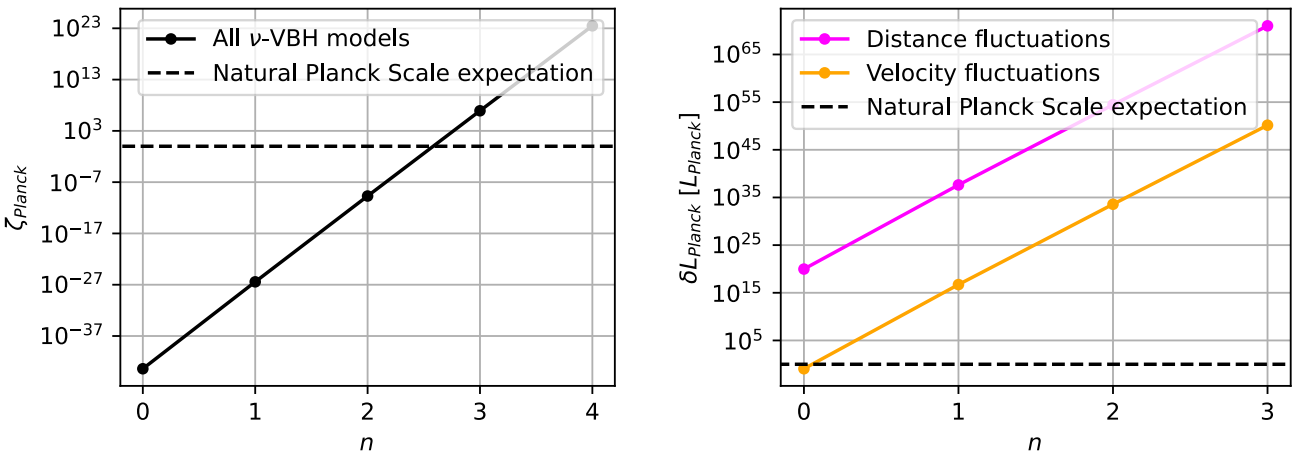

FIGURE 33: The sensitivities (90%) of the oscNext sample to the ν-VBH (left) and lightcone fluctuation (right) models expressed as ζ_{Planck} and δL_{Planck} compared to the natural Planck scale expectations. The analysis is sensitive to values of the parameters above the lines, which result in stronger damping. The ν-VBH models are shown as one line, because the lines for the individual models would otherwise appear to be exactly on top of each other.

For the ν-VBH models with $n \leqq 2$, the oscNext sample is sensitive to effects far weaker than the Planck scale expectations. When real data is analyzed, these predictions can thus either be measured or strongly excluded if no signal is detected. For $n = 3$ and 4 the Planck scale predictions are not reached and can not be detected or excluded by the oscNext sample. The MOEWS decoherence analysis is however expected to improve the sensitivity at high n, and can potentially exclude the natural expectations for $n > 2$.

Consequently, the ability to probe the Planck scale heavily depends on the assumed energy-dependence of the considered effects. By applying linear interpolation (in $\log_{10}(\zeta_{\text{Planck}})$), the value of n where the sensitivity of the oscNext sample to ζ_{Planck} becomes weaker than what is needed to measure the natural expectation is found to be $n \sim 2.58$. This value can be seen as a sensitivity (90% confidence) of the oscNext sample to the value of n for the natural expectation of ν-VBH models. It is remarkable that the oscNext sample is able to probe quantum gravity effects which are suppressed by a factor of $(E/E_{\text{Planck}})^{2.58}$.

For the lightcone fluctuation cases however, the effects have to be far stronger than the natural Planck scale expectations for the oscNext sample to be able to detect them. Nevertheless, there is one exception, which is velocity fluctuations with $n = 0$. The specific case implies that the velocity uncertainty of any neutrino, regardless of its energy, is equal to the velocity itself. This is however not meaningful since neutrinos would then travel with a velocity close to the speed of light with an uncertainty of the speed of light. The point is thus only kept in the figure for completeness.

The difference in the sensitivity to the natural expectations of the ν-VBH and lightcone fluctuation models is caused by several things. The main reason is that damping becomes large, only when the accumulated distance uncertainty is comparable to the oscillation wavelength. The wavelengths are macroscopic distances, whereas the predicted fluctuations are microscopic. In the ν-VBH cases however, a neutrino is fully decohered with an ensemble after only one interaction with a VBH. A detectable signal can thus be reached even if the interactions happen only very rarely.

We have to keep in mind, that the predictions discussed here are based on very broad assumptions about the nature of quantum gravity. As a result, the scale of quantum gravity effects is not necessarily the Planck scale. It is thus important to search for potential signals which are both weaker and stronger than what is expected from the Planck Scale. Additionally, it is also possible that decoherence could result from other new physics apart from quantum gravity.

6.3 Comparisons to other studies

6.3.1 Previous IceCube senstivity study

A study of decoherence effects in IceCube has previously been carried out in [53], which was made by theorists external to the IceCube collaboration, using public data. In the study, both a DeepCore sample with three years of live-time and an IceCube sample with one year of live-time were analyzed. The energy bins of the histograms of the two samples go from 6 GeV to 56 GeV and 0.4 TeV to 20 TeV, respectively. The DeepCore sample in particular has significantly less events and lower considered energies than the oscNext sample. The sensitivity is thus expected to be weaker. However, the treatment of

systematics is less thorough than in this project and the sensitivities are thus considered to be optimistic for the samples used.

How the models tested in [53] relate to the models of this thesis has been investigated in Section D. We find that one of the scenarios tested (referred to 'atmospheric ($\gamma_{31} = \gamma_{32}$)' in the paper) is approximately comparable to the lightcone fluctuations model with $m = 0.5$. The tested values of n in the paper correspond to $n = 0$, 0.5, 1, 1.5, and 2 of the lightcone fluctuations model (the latter will be denoted $n_{\text{lightcone}}$). This study finds that for all of the tested scenarios, the data is consistent with no decoherence, and thus upper bounds (at 95% confidence) are derived. Since the fundamental parameters of the models, which we compare here, are not the same, we have chosen to express the bounds/sensitivities as the coherence length of a 1 GeV neutrino. The bounds found in [53] for IceCube and DeepCore are thus shown alongside the sensitivities of the oscNext sample to the lightcone fluctuations model with $m = 0.5$ in Figure 34.

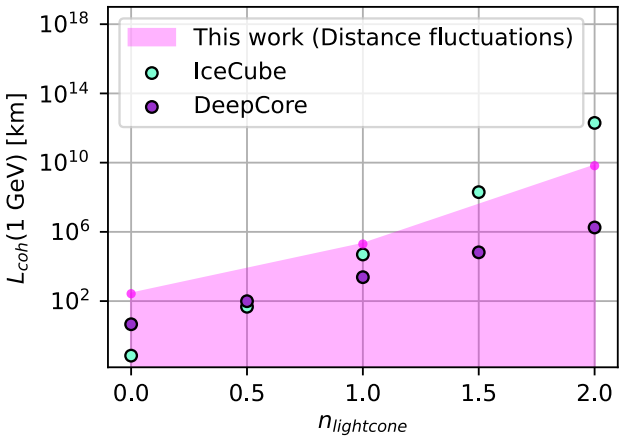

FIGURE 34: DeepCore/IceCube 95% confidence limits on L_{coh}(1 GeV) obtained in [53] assuming normal mass ordering ($m_1 < m_2 < m_3$) compared to the sensitivity of the oscNext sample to the lightcone fluctutuations model with $m = 0.5$ from this project. The area beneath the curve is shaded, because this is the coherence lengths that the oscNext sample is sensitive to. The subscript of n (x-axis) is included to denote that this is the energy-dependence parameter of lightcone fluctuations model specifically (see Section D for details).

The sensitivity of the oscNext sample to this model is ~ 2 to ~ 4 orders of magnitude better than the DeepCore sample analyzed in [53]. This difference is mainly caused by the increased number of events and energy range of the oscNext sample. At high values of n, the IceCube sample outperforms oscNext. We however expect the MEOWS decoherence analysis to provide the best sensitivities at this range of n. By complimenting the oscNext and MEOWS decoherence analyses with each other, we expect to obtain the most sensitive measurement of decoherence with IceCube atmospheric neutrino data.

6.3.2 Neutrino beam experiments

Some of the most stringent limits found on decoherence of neutrino oscillations in previous studies are from long baseline (beam) experiments. In [51] an analysis is performed using

data from the MINOS [86] and T2K [87, 88] neutrino beam experiments. The MINOS experiment has two detectors along the beam. The Near Detector is located 1.04 km from the production of the beam, and the Far Detector is located 735 km away. The detectors observe muon neutrinos (through charged current interactions) with an energy spectrum that goes from 1 GeV to 14 GeV and peaks at $\sim$ 2.9 GeV. The T2K experiment has several near detectors located $\sim$ 280 m along the beam. At a distance of 295 km away from the beam production, the neutrinos are detected by the Super-Kamiokande 50-kilotonne water Cherenkow detector [89, 90]. The detector is situated at an angle of 2.5 degrees from the beam axis, which gives a narrow energy spectrum of the observed neutrinos, peaking around 0.6 GeV. These experiments are thus low-energy and test single baselines but have much better resolution, calibration, and knowledge of the initial flux compared to DeepCore.

The study tests three cases of decoherence of neutrino oscillations, which are not designed to specifically target quantum gravity phenomena. However, 'case 1' from the paper produces the same damping as the ν-VBH randomize flavor scenario considered in this thesis. Similarly, 'case 2' can be directly compared to the ν-VBH phase perturbation model. The third case, 'case 3', is however the same as the 'atmospheric ($\gamma_{31} = \gamma_{32}$)' case from the previous IceCube sensitivity study [53] discussed in Section 6.3.1. It is thus comparable to the lightcone fluctuations model with $m = 0.5$ in this thesis (see Section D for details). The tested values of the energy-dependence parameter are $n = -2$, 0, and 2. For all the tested scenarios it is found that the data from both MINOS and T2K is consistent with no decoherence and upper bounds (at 90% confidence) are derived. The results are shown in Figure 35 alongside the sensitivities of the oscNext sample found in this thesis and other bounds, which will be discussed in Section 6.3.3 and 6.3.4.

The figure shows that the bounds obtained by MINOS and T2K are stronger for damping which decreases with energy ($n = -2$ for ν-VBH cases and $n = 0$ for lightcone fluctuations) than the sensitivity of the oscNext sample. The difference here is a result of the beam experiments having access to lower energy neutrinos, and that the effects grow at low energies. Conversely, for damping which increases with energy ($n = 0$ and 2 for ν-VBH cases and $n = 1$ and 2 for lightcone fluctuations) the oscNext sample is several orders of magnitude more sensitive than the beam experiments. This increase in sensitivity at high n is caused by the neutrinos in the oscNext sample being of much higher energy than the beam experiments. The oscNext sample is thus suitable for probing damping effects which increase with energy, which is generally expected for quantum gravity effects.

6.3.3 Super-Kamiokande atmospheric neutrino experiment

Decoherence of atmospheric neutrino oscillations has been studied in [49] which analyses atmospheric neutrino data from the Super-Kamiokande detector [89, 90]. The data sample consists of ν_e and ν_μ events and is divided into two energy bins; sub-GeV and multi-GeV neutrinos, and five $\cos\theta_{\text{zenith}}$ bins. The total number of neutrino events in the sample is 3210 and is thus lower statistics than the oscNext sample, and it contains lower energies.

In this study the neutrino oscillations are simplified to two flavors ($\nu_\mu \leftrightarrow \nu_\tau$). The considered decoherence does not target any specific quantum gravity scenario, but causes the neutrino oscillations to dampen toward the oscillation average. It is thus most accurate to compare the results from this study to the ν-VBH phase perturbation model from this

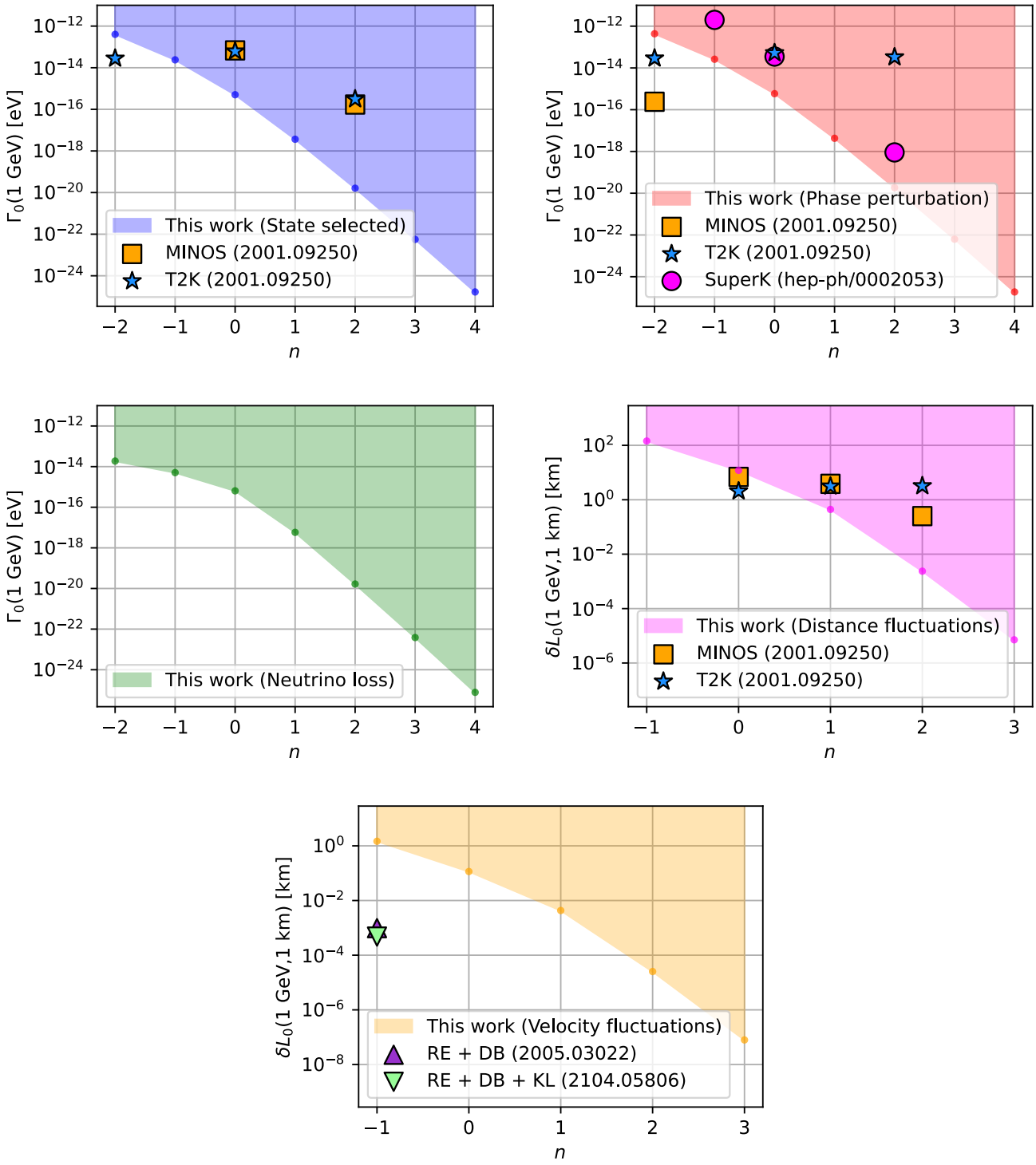

FIGURE 35: The sensitivities (at 90% confidence) of the oscNext sample to the models considered in this thesis. The shaded areas are the regions of the parameter space that the data is sensitive to. Bounds obtained from previous studies of beam experiments (MINOS and T2K, see Section 6.3.2), atmospheric neutrinos (Super-Kamiokande (SuperK), see Section 6.3.3), and reactor experiments (RENO (RE), Daya Bay (DB), and KamLAND (KL), see Section 6.3.4) are shown for reference.

thesis. Three different values of the energy-dependence parameter are tested: $n = -1$, 0, and 2. In all cases it is found that the data is consistent with no decoherence. The derived upper bounds (at 90% confidence) are shown in the upper right panel of Figure 35 alongside the sensitivity of the oscNext sample to the phase perturbation and the bounds found by MINOS and T2K are discussed in Section 6.3.2.

It can be seen that the bounds follow the same pattern as the oscNext sample sensitivity, which is however more than one order of magnitude stronger. The difference in sensitivity is mainly a result of the large increase in statistics for the oscNext sample.

6.3.4 Wave packet decoherence with reactor experiments

Wave packet decoherence of neutrino oscillations has been studied with reactor experiments in [91], which combines data from Reno [92] and Daya Bay [93], and in [94], which combines data from RENO, Daya Bay, and KamLAND [95]. Reactor neutrino experiments detect electron antineutrinos produced by nuclear reactors at several distances from the production point, which allows them to observe neutrino oscillations. The energy ranges of the experiments are MeV scale neutrinos, but the numbers of events are $\sim$ 2,000 for KamLAND, $\sim$ 700,000 for RENO, and $\sim$ 1,500,000 for Daya Bay. Combining these experiments thus gives statistics far exceeding the oscNext sample.

The type of decoherence searched for in these studies is wave packet decoherence. As discussed in Section 3.8, wave packet decoherence results in damping, which is equal to the lightcone fluctuations model with $m = 1$ and $n = -1$ considered in this thesis. The results of the two analyses can thus be compared. In the two studies it is found that the data is consistent with no wave packet decoherence. The lower bounds (at 90% confidence) derived on the spatial spread of neutrino wave packet are $\sigma_x > 1.02 \times 10^{-4}$ nm and $\sigma_x > 2.1 \times 10^{-4}$ nm, respectively. These are lower bounds since smaller σ_x results in more decoherence, and the parameter is inversely proportional to δL_0 as derived in Section 3.8. The bounds on σ_x have thus been re-expressed as limits on δL_0 (through Equation 39) and are shown in the bottom panel of Figure 35 alongside the sensitivity of the oscNext sample to the lightcone fluctuations model with $m = 1$. Similarly, the sensitivity of the oscNext sample to δL_0 has been recast as a sensitivity to wavepacket decoherence, which gives $\sigma_x > 6.7 \times 10^{-8}$ nm. We thus see that the oscNext sample has very limited sensitivity to wavepacket decoherence compared to the reactor experiments. This is a result of the reactor experiments having access to lower energy neutrinos, and the wave packet decoherence increasing at low energies. Additionally, the high statistics of the reactor data increases its sensitivity significantly.

Reactor experiments are however not ideal for seaching for quantum gravity induced decoherence. As discussed, such effect are generally expected to decrease at low energies and increase at high energies. They are thus preferably searched for in higher energy neutrinos, which DeepCore can measure.

6.3.5 Potential further comparisons

From Figure 35 it can be seen that no studies have been found which can be directly compared to the ν-VBH neutrino loss scenario. In Section 3.8, it was discussed that damping from neutrino absorption and decay is similar to neutrino loss, but the models are

not directly comparable. If the right assumptions or approximations are made however, it might be possible to interpassumptionsret limits on neutrino absorption and decay as limits on the neutrino loss scenario, or vice versa.

In [96] data from KamLAND is combined with solar neutrino data [97] to search for decoherence. The low energies observed here, and the long baseline traveled by neutrinos from the sun, may give leading bounds on scenarios which increase at low energies.

Finally, fluctuations of space-time have been studied in propagation of photons from astrophysical sources in [57] and [58]. Here image degradation and arrival time spread is searched for in X-rays and gamma-rays observed from quasars, blazars, and gamma-ray bursts. The results from these studies can potentially be interpreted as bounds on the lightcone fluctuation cases from this thesis.

6.4 Sensitivities expressed as coherence lengths

Finally, we can investigate what coherence lengths of neutrino oscillations the oscNext sample is sensitive to. Here we have chosen to look at the sensitivities to the coherence length of a 1 GeV neutrino for the ν-VBH models with the different assumed energy-dependencies (values of n). Note that the analysis measures decoherence across many energies, and here the sensitivity is thus extrapolated to 1 GeV. The result is shown in Figure 36 along with many reference distance, including beam experiments, astrophysical distances, and the natural Planck scale expectation.

This figure gives a qualitative indication of the power of the oscNext decoherence analysis compared to beam experiments, which operate at $\mathcal{O}(1\text{ GeV})$. For simplicity, we assume that such experiments are sensitive to decoherence when $L_{\text{coh}}(1\text{ GeV})$ is of the same order of magnitude as the baseline. We can then look at a single value of n in the Figure; for instance $n = 2$, which is predicted by quantum gravity. If a neutrino beam experiment is to have roughly the same sensitivity to the ν-VBH models as the oscNext sample, then the total baseline of the experiment would have to be the distance between the Sun and Jupiter. The coherence lengths probed by DeepCore at this energy for the assumed n are thus astrophysical in scale, and are thus out of reach of any terrestrial beam experiment at this energy scale.

This example highlights the importance of using high-energy neutrinos when searching for quantum gravity effects which, are expected to increase with energy. The oscNext sample is thus very powerful, and the MEOWS decoherence analysis is expected to improve the sensitivity at high n further by orders of magnitude.

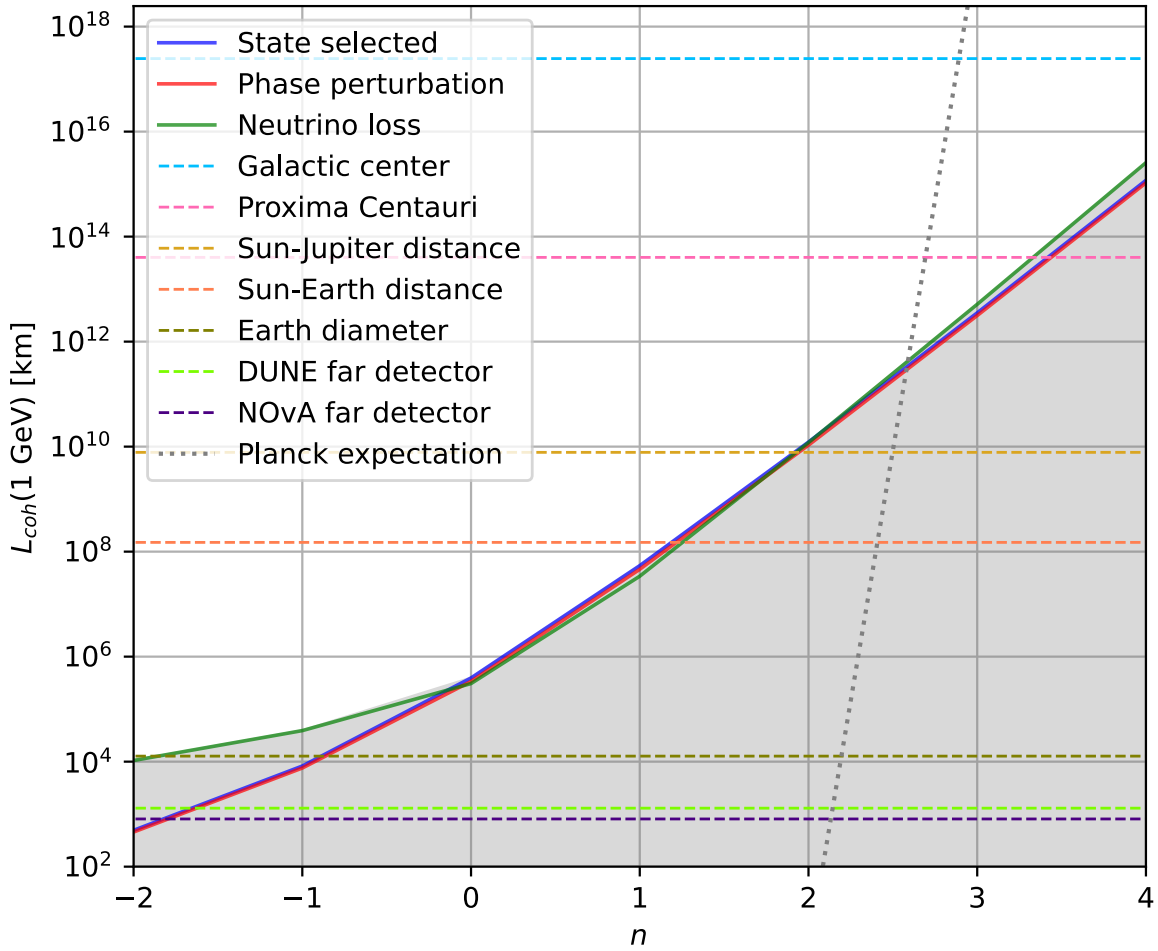

FIGURE 36: The 90% confidence limits for the ν-VBH models expressed as $L_{\text{coh}}(1\text{ GeV})$ along with various reference distances. The area underneath the lines has been grayed out, because this is the part of the parameter space the oscNext sample is sensitive to. The lines for the randomize flavor and phase perturbation models appear to be exactly on top of each other when expressed as $L_{\text{coh}}(1\text{GeV})$. NOvA [98] and DUNE [99, 100, 101, 102] are the current and upcoming longest baseline neutrino beam experiments, respectively.

7 Conclusion and future work

By invoking heuristic models of quantum gravity, neutrinos provide us with a way to probe effects often predicted by quantum gravity theories. Through simulations, it has been shown that neutrinos interacting with VBHs or traveling in a fluctuating space-time results in damping of the neutrino oscillations, which would otherwise be observed. The phenomenology developed in [13] and [14] allows the observed damping to be related to parameters of underlying quantum gravity phenomena. Additionally, these effects can be described as decoherence in an open quantum system. The open quantum system formulations are implemented in `nuSQuIDS`, which makes us able to accurately calculate oscillation probabilities of neutrinos, while taking VBH interactions and lightcone fluctuations into account. This allows us to search for the considered phenomena in atmospheric neutrino data.

The considered data consists of nine years of atmospheric neutrinos observed by IceCube DeepCore, called the oscNext sample. It is a high statistics sample which has good energy and angular reconstruction. In addition to the parameters related to decoherence and neutrino oscillations, a full set of nuisance parameters describing various systematics are taken into account. How the models are fitted to the data has been thoroughly studied, which allows us to estimate the sensitivity of the oscNext sample to the considered models.

We find that the oscNext sample is sensitive to 'natural' Planck scale expectations of ν-VBH interactions for values of the energy-dependence parameter $n < 2.58$ (at 90% confidence). For instance in the $n = 2$ case, the sensitivity of the oscNext sample to the ν-VBH state selected model is $\zeta_{\text{Planck}} > 2.25 \times 10^{-10}$ (at 90% confidence), which surpasses the natural Planck scale expectation of $\zeta_{\text{Planck}} = 1$ by many orders of magnitude. For the lightcone fluctuation models however, the oscNext sample does not have sensitivity to the natural Planck scale expectations.

The results obtained here have been compared to bounds on decoherence found in previous studies of reactor experiments, beam experiments, and atmospheric neutrino experiments. The reactor and beam experiments perform better for effects which are strong at low energies, whereas the atmospheric neutrino data has better sensitivity to scenarios which increase with energy. Additionally, the oscNext and MEOWS decoherence analyses are expected to improve on bounds obtained from previous atmospheric neutrino studies. IceCube is thus currently the best experiment to search for decoherence of neutrino oscillations caused by quantum gravity effects.

The next major step of the analysis is to make it ready to be applied to real data. Some aspects of the analysis however, need to be investigated in more detail. These include:

- If the lightcone fluctuations scenarios are to be searched for in the data, it should be investigated how to properly calculate the resulting damping when matter effects are present. The correct treatment of this scenario should be implemented in `nuSQuIDS`, so that oscillation probabilities of neutrinos traveling through the Earth can be calculated, including both matter effects and lightcone fluctuations. The sensitivity of the oscNext sample to lightcone fluctuations should be derived again with matter effects taken into account.

- The impact of the nuisance parameters on the analysis has been studied for the standard oscillations analysis, but not specifically for this analysis. Some of the nuisance parameters which were fixed during the fits might have unexpected correlations with the physics parameters, Γ_0 and δL_0. This can be investigated by running a test named the 'systematic impact test', which has not been performed for this analysis yet. It should however be done before real data is considered.

When these tasks have been carried out, the full statistical analysis can be applied to the real data of the oscNext sample. Together with the MEOWS decoherence analysis, this will be the most sensitive measurement to date on neutrino decoherence resulting from quantum gravity predictions.

References

[1] S. W. Hawking. The unpredictability of quantum gravity. *Communications in Mathematical Physics*, 87:395–415, 1982.

[2] John Archibald Wheeler. Geons. *Phys. Rev.*, 97:511–536, Jan 1955.

[3] Y. Jack Ng. Holographic Quantum Foam. In *12th Marcel Grossmann Meeting on General Relativity*, pages 2435–2437, 1 2010.

[4] Charles W. Misner, K. S. Thorne, and J. A. Wheeler. *Gravitation*. W. H. Freeman, San Francisco, 1973.

[5] John Ellis, N.E. Mavromatos, and D.V. Nanopoulos. String theory modifies quantum mechanics. *Physics Letters B*, 293(1):37–48, 1992.

[6] L. H. Ford. Gravitons and light cone fluctuations. *Phys. Rev. D*, 51:1692–1700, Feb 1995.

[7] Hongwei Yu, N. F. Svaiter, and L. H. Ford. Quantum light-cone fluctuations in compactified spacetimes. *Phys. Rev. D*, 80:124019, Dec 2009.

[8] S. W. Hawking. Virtual black holes. *Phys. Rev. D*, 53:3099–3107, 1996.

[9] Gerard 't Hooft. Virtual Black Holes and Space–Time Structure. *Foundations of Physics*, 48:1134–1149, 2018.

[10] Y. Fukuda et al. Evidence for oscillation of atmospheric neutrinos. *Phys. Rev. Lett.*, 81:1562–1567, 1998.

[11] Q. R. Ahmad et al. Measurement of the rate of $\nu_e + d \rightarrow p + p + e^-$ interactions produced by ^{8}B solar neutrinos at the Sudbury Neutrino Observatory. *Phys. Rev. Lett.*, 87:071301, 2001.

[12] Q. R. Ahmad et al. Direct evidence for neutrino flavor transformation from neutral current interactions in the Sudbury Neutrino Observatory. *Phys. Rev. Lett.*, 89:011301, 2002.

[13] Thomas Stuttard and Mikkel Jensen. Neutrino decoherence from quantum gravitational stochastic perturbations. *Physical Review D*, 102(11), Dec 2020.

[14] Thomas Stuttard. Neutrino signals of lightcone fluctuations resulting from fluctuating spacetime. *Physical Review D*, 104(5), Sep 2021.

[15] Standard Model, `https://www.physik.uzh.ch/en/researcharea/lhcb/outreach/StandardModel.html`, Last visited Mar 10, 2022.

[16] Sheldon L. Glashow. Partial-symmetries of weak interactions. *Nuclear Physics*, 22(4):579–588, 1961.

[17] Y. et al. Abe. Indication of reactor $\overline{\nu}_e$ disappearance in the double chooz experiment. *Phys. Rev. Lett.*, 108:131801, Mar 2012.

[18] F. P. An et al. Observation of electron-antineutrino disappearance at Daya Bay. *Phys. Rev. Lett.*, 108:171803, 2012.

[19] J. K. Ahn et al. Observation of Reactor Electron Antineutrino Disappearance in the RENO Experiment. *Phys. Rev. Lett.*, 108:191802, 2012.

[20] K. Anderson et al. The NuMI Facility Technical Design Report. 10 1998.

[21] G. Acquistapace et al. The CERN neutrino beam to Gran Sasso (NGS). 5 1998.

[22] K. Abe et al. The t2k experiment. *Nuclear Instruments and Methods in Physics Research Section A: Accelerators, Spectrometers, Detectors and Associated Equipment*, 659(1):106–135, 2011.

[23] G. J. Feldman, J. Hartnell, and T. Kobayashi. Long-Baseline Neutrino Oscillation Experiments. *Advances in High Energy Physics*, vol. 2013:Article ID 475749, 2013.

[24] P. Meszaros. Astrophysical Sources of High Energy Neutrinos in the IceCube Era. *Ann. Rev. Nucl. Part. Sci.*, 67:45–67, 2017.

[25] Ziro Maki, Masami Nakagawa, and Shoichi Sakata. Remarks on the unified model of elementary particles. *Prog. Theor. Phys.*, 28:870–880, 1962.

[26] Ivan Esteban, M. C. Gonzalez-Garcia, Alvaro Hernandez-Cabezudo, Michele Maltoni, and Thomas Schwetz. Global analysis of three-flavour neutrino oscillations: synergies and tensions in the determination of θ_{23}, δ_{CP}, and the mass ordering. *JHEP*, 01:106, 2019.

[27] NuFit 4.0 (2018), `nu-fit.org`, Last visited May 3, 2022.

[28] Takaaki Kajita. Atmospheric neutrinos. *New Journal of Physics*, 6:194, 12 2004.

[29] Mark Thomson. *Modern particle physics*. Cambridge University Press, New York, 2013.

[30] Particle Data Group and P A Zyla. Review of Particle Physics. *Progress of Theoretical and Experimental Physics*, 2020(8), 08 2020. 083C01.

[31] L. Wolfenstein. Neutrino oscillations in matter. *Phys. Rev. D*, 17:2369–2374, May 1978.

[32] Daniela Lietti and Michela Prest. The electron muon ranger for the mice experiment. 03 2022.

[33] Aartsen et al. Measurement of atmospheric tau neutrino appearance with icecube deepcore. *Physical Review D*, 99(3), Feb 2019.

[34] J. A. Formaggio and G. P. Zeller. From ev to eev: Neutrino cross sections across energy scales. *Rev. Mod. Phys.*, 84:1307–1341, Sep 2012.

[35] Konstantia Balasi, Christos Markou, K. Tzamarioudaki, P. Rapidis, Evangelia Drakopoulou, K. Pikounis, and C. Begatelas. The response of an autonomous underwater telescope to high energy neutrinos for the observation of gamma-ray bursts (grbs). *HNPS Proceedings*, 22:88, 03 2019.

[36] M. G. Aartsen et al. The IceCube Neutrino Observatory: Instrumentation and Online Systems. *JINST*, 12(03):P03012, 2017.

[37] IceCube, `https://icecube.wisc.edu/science/icecube/`, Last visited Mar 16, 2022.

[38] B. R. Martin. *Nuclear and particle physics: An introduction. 2nd ed.* John Wiley & Sons Ltd, 2009.

[39] Robert Stokstad. Design and Performance of the IceCube Electronics. 2005.

[40] R. Abbasi et al. The Design and Performance of IceCube DeepCore. *Astropart. Phys.*, 35:615–624, 2012.

[41] R. Abbasi et al. Low Energy Event Reconstruction in IceCube DeepCore. 3 2022.

[42] M. G. Aartsen et al. Multimessenger observations of a flaring blazar coincident with high-energy neutrino IceCube-170922A. *Science*, 361(6398):eaat1378, 2018.

[43] et al. Aartsen. Measurement of atmospheric neutrino oscillations at 6–56 gev with icecube deepcore. *Physical Review Letters*, 120(7), Feb 2018.

[44] S. W. Hawking. Breakdown of predictability in gravitational collapse. *Phys. Rev. D*, 14:2460–2473, Nov 1976.

[45] Ling-Fong Li. *Introduction to Renormalization in Field Theory*, pages 465–491. 2013.

[46] Michael B. Green, John H. Schwarz, and Edward Witten. *Superstring Theory: 25th Anniversary Edition*, volume 1 and 2 of *Cambridge Monographs on Mathematical Physics*. Cambridge University Press, 2012.

[47] Carlo Rovelli. Loop quantum gravity. *Living Rev. Rel.*, 1:1, 1998.

[48] D. J. Bird et al. Detection of a cosmic ray with measured energy well beyond the expected spectral cutoff due to cosmic microwave radiation. *Astrophys. J.*, 441:144–150, 1995.

[49] E. Lisi, A. Marrone, and D. Montanino. Probing possible decoherence effects in atmospheric neutrino oscillations. *Phys. Rev. Lett.*, 85:1166–1169, Aug 2000.

[50] G. L. Fogli, E. Lisi, A. Marrone, D. Montanino, and A. Palazzo. Probing nonstandard decoherence effects with solar and kamland neutrinos. *Phys. Rev. D*, 76:033006, Aug 2007.

[51] A. L. G. Gomes, R. A. Gomes, and O. L. G. Peres. Quantum decoherence and relaxation in neutrinos using long-baseline data. 1 2020.

[52] Luis A. Anchordoqui, Haim Goldberg, M. C. Gonzalez-Garcia, Francis Halzen, Dan Hooper, Subir Sarkar, and Thomas J. Weiler. Probing Planck scale physics with IceCube. *Phys. Rev. D*, 72:065019, 2005.

[53] Pilar Coloma, Jacobo Lopez-Pavon, Ivan Martinez-Soler, and Hiroshi Nunokawa. Decoherence in Neutrino Propagation Through Matter, and Bounds from IceCube/DeepCore. *Eur. Phys. J. C*, 78(8):614, 2018.

[54] E. S. Perlman, S. A. Rappaport, W. A. Christiansen, Y. J. Ng, J. DeVore, and D. Pooley. NEW CONSTRAINTS ON QUANTUM GRAVITY FROM x-RAY AND GAMMA-RAY OBSERVATIONS. *The Astrophysical Journal*, 805(1):10, may 2015.

[55] Ryan Cooke, Louise Welsh, Michele Fumagalli, and Max Pettini. A limit on Planck-scale froth with ESPRESSO. *Mon. Not. Roy. Astron. Soc.*, 494(4):4884–4890, 2020.

[56] Richard Lieu and Lloyd W. Hillman. The Phase coherence of light from extragalactic sources - direct evidence against first order quantum gravity fluctuations in time and space. *Astrophys. J. Lett.*, 585:L77–L80, 2003.

[57] A. A. et al. Abdo. A limit on the variation of the speed of light arising from quantum gravity effects. *Nature*, 462(7271):331–334, Nov 2009.

[58] Vlasios Vasileiou, Jonathan Granot, Tsvi Piran, and Giovanni Amelino-Camelia. A planck-scale limit on spacetime fuzziness and stochastic lorentz invariance violation. *Nature Physics*, 11(4):344–346, Apr 2015.

[59] G. Lindblad. On the generators of quantum dynamical semigroups. *Communications in Mathematical Physics*, 48(2):119 – 130, 1976.

[60] Luis A. Anchordoqui, Haim Goldberg, M. C. Gonzalez-Garcia, Francis Halzen, Dan Hooper, Subir Sarkar, and Thomas J. Weiler. Probing Planck scale physics with IceCube. *Phys. Rev. D*, 72:065019, 2005.

[61] M. G. Aartsen et al. Evidence for High-Energy Extraterrestrial Neutrinos at the IceCube Detector. *Science*, 342:1242856, 2013.

[62] M. G. Aartsen et al. Neutrino emission from the direction of the blazar TXS 0506+056 prior to the IceCube-170922A alert. *Science*, 361(6398):147–151, 2018.

[63] Markus Ahlers, Mauricio Bustamante, and Siqiao Mu. Unitarity bounds of astrophysical neutrinos. *Phys. Rev. D*, 98:123023, Dec 2018.

[64] Kevin J. Kelly and Pedro A.N. Machado. Multimessenger astronomy and new neutrino physics. *Journal of Cosmology and Astroparticle Physics*, 2018(10):048–048, oct 2018.

[65] S. Nussinov. Solar neutrinos and neutrino mixing. *Physics Letters B*, 63(2):201–203, 1976.

[66] C. Giunti and C. W. Kim. Coherence of neutrino oscillations in the wave packet approach. *Phys. Rev. D*, 58:017301, 1998.

[67] Mattias Blennow, Tommy Ohlsson, and Walter Winter. Damping signatures in future neutrino oscillation experiments. *JHEP*, 06:049, 2005.

[68] John N. Bahcall, Nicola Cabibbo, and Amos Yahil. Are neutrinos stable particles? *Phys. Rev. Lett.*, 28:316–318, Jan 1972.

[69] Carlos A. Argüelles, Jordi Salvado, and Christopher N. Weaver. nuSQuIDS: A toolbox for neutrino propagation. 12 2021.

[70] Carlos A. Argüelles Delgado, Jordi Salvado, and Christopher N. Weaver. A Simple Quantum Integro-Differential Solver (SQuIDS). *Comput. Phys. Commun.*, 196:569–591, 2015.

[71] GNU Scientific Library, `https://www.gnu.org/software/gsl/`, Last visited Apr 19, 2022.

[72] Adam M. Dziewonski and Don L. Anderson. Preliminary reference earth model. *Physics of the Earth and Planetary Interiors*, 25(4):297–356, 1981.

[73] Thomas K. Gaisser, Kyle Jero, Albrecht Karle, and Jakob van Santen. Generalized self-veto probability for atmospheric neutrinos. *Phys. Rev. D*, 90(2):023009, 2014.

[74] M. G. Aartsen et al. Computational techniques for the analysis of small signals in high-statistics neutrino oscillation experiments. *Nucl. Instrum. Meth. A*, 977:164332, 2020.

[75] G. D. Barr, T. K. Gaisser, S. Robbins, and Todor Stanev. Uncertainties in Atmospheric Neutrino Fluxes. *Phys. Rev. D*, 74:094009, 2006.

[76] Hans Dembinski and Piti Ongmongkolkul et al. scikit-hep/iminuit. Dec 2020.

[77] S. S. Wilks. The Large-Sample Distribution of the Likelihood Ratio for Testing Composite Hypotheses. *The Annals of Mathematical Statistics*, 9(1):60 – 62, 1938.

[78] Gary J. Feldman and Robert D. Cousins. A Unified approach to the classical statistical analysis of small signals. *Phys. Rev. D*, 57:3873–3889, 1998.

[79] Dong C Liu and Jorge Nocedal. On the limited memory BFGS method for large scale optimization. *Mathematical Programming*, 45(1):503–528, August 1989.

[80] Pauli et al. Virtanen. SciPy 1.0: Fundamental Algorithms for Scientific Computing in Python. *Nature Methods*, 17:261–272, 2020.

[81] P. Kaelo and Montaz Ali. Some variants of the controlled random search algorithm for global optimization. *Journal of Optimization Theory and Applications*, 130:253–264, 01 2006.

[82] Eligius M T Hendrix, P M Ortigosa, and I García. On success rates for controlled random search. *Journal of Global Optimization*, 21(3):239–263, November 2001.

[83] W. l. price,.

[84] T. Rowan. Functional stability analysis of numerical algorithms, ph.d. thesis, department of computer sciences, university of texas at austin, 1990.

[85] Steven G. Johnson, The NLopt nonlinear-optimization package, `http://github.com/stevengj/nlopt`.

[86] P. Adamson et al. Measurement of Neutrino and Antineutrino Oscillations Using Beam and Atmospheric Data in MINOS. *Phys. Rev. Lett.*, 110(25):251801, 2013.

[87] K. Abe et al. Updated T2K measurements of muon neutrino and antineutrino disappearance using 1.5×10^{21} protons on target. *Phys. Rev. D*, 96(1):011102, 2017.

[88] K. Abe et al. Combined Analysis of Neutrino and Antineutrino Oscillations at T2K. *Phys. Rev. Lett.*, 118(15):151801, 2017.

[89] S. Fukuda et al. The super-kamiokande detector. *Nuclear Instruments and Methods in Physics Research Section A: Accelerators, Spectrometers, Detectors and Associated Equipment*, 501(2):418–462, 2003.

[90] K. Abe et al. Calibration of the super-kamiokande detector. *Nuclear Instruments and Methods in Physics Research Section A: Accelerators, Spectrometers, Detectors and Associated Equipment*, 737:253–272, 2014.

[91] Andre de Gouvea, Valentina de Romeri, and Christoph Andreas Ternes. Probing neutrino quantum decoherence at reactor experiments. *JHEP*, 08:018, 2020.

[92] RENOCollaboration, J. Yoo, 'Recent results from reno experiment' `https://indico.fnal.gov/event/43209/contributions/187886/attachments/130339/158753/Neutrino2020YooRENO.pdf`, July 2020.

[93] D. Adey et al. Measurement of the Electron Antineutrino Oscillation with 1958 Days of Operation at Daya Bay. *Phys. Rev. Lett.*, 121(24):241805, 2018.

[94] André de Gouvêa, Valentina De Romeri, and Christoph A. Ternes. Combined analysis of neutrino decoherence at reactor experiments. *JHEP*, 06:042, 2021.

[95] A. Gando et al. Constraints on θ_{13} from A Three-Flavor Oscillation Analysis of Reactor Antineutrinos at KamLAND. *Phys. Rev. D*, 83:052002, 2011.

[96] G. L. Fogli, E. Lisi, A. Marrone, D. Montanino, and A. Palazzo. Probing non-standard decoherence effects with solar and KamLAND neutrinos. *Phys. Rev. D*, 76:033006, 2007.

[97] G. L. Fogli, E. Lisi, A. Marrone, and A. Palazzo. Global analysis of three-flavor neutrino masses and mixings. *Prog. Part. Nucl. Phys.*, 57:742–795, 2006.

[98] M. A. Acero et al. An Improved Measurement of Neutrino Oscillation Parameters by the NOvA Experiment. 8 2021.

[99] R. Acciarri et al. Long-Baseline Neutrino Facility (LBNF) and Deep Underground Neutrino Experiment (DUNE): Conceptual Design Report, Volume 1: The LBNF and DUNE Projects. 1 2016.

[100] R. Acciarri et al. Long-Baseline Neutrino Facility (LBNF) and Deep Underground Neutrino Experiment (DUNE): Conceptual Design Report, Volume 2: The Physics Program for DUNE at LBNF. 12 2015.

[101] James Strait et al. Long-Baseline Neutrino Facility (LBNF) and Deep Underground Neutrino Experiment (DUNE): Conceptual Design Report, Volume 3: Long-Baseline Neutrino Facility for DUNE June 24, 2015. 1 2016.

[102] R. Acciarri et al. Long-Baseline Neutrino Facility (LBNF) and Deep Underground Neutrino Experiment (DUNE): Conceptual Design Report, Volume 4 The DUNE Detectors at LBNF. 1 2016.

[103] V. Barger, K. Whisnant, S. Pakvasa, and R. J. N. Phillips. Matter effects on three-neutrino oscillations. *Phys. Rev. D*, 22:2718–2726, Dec 1980.

A Additional figures

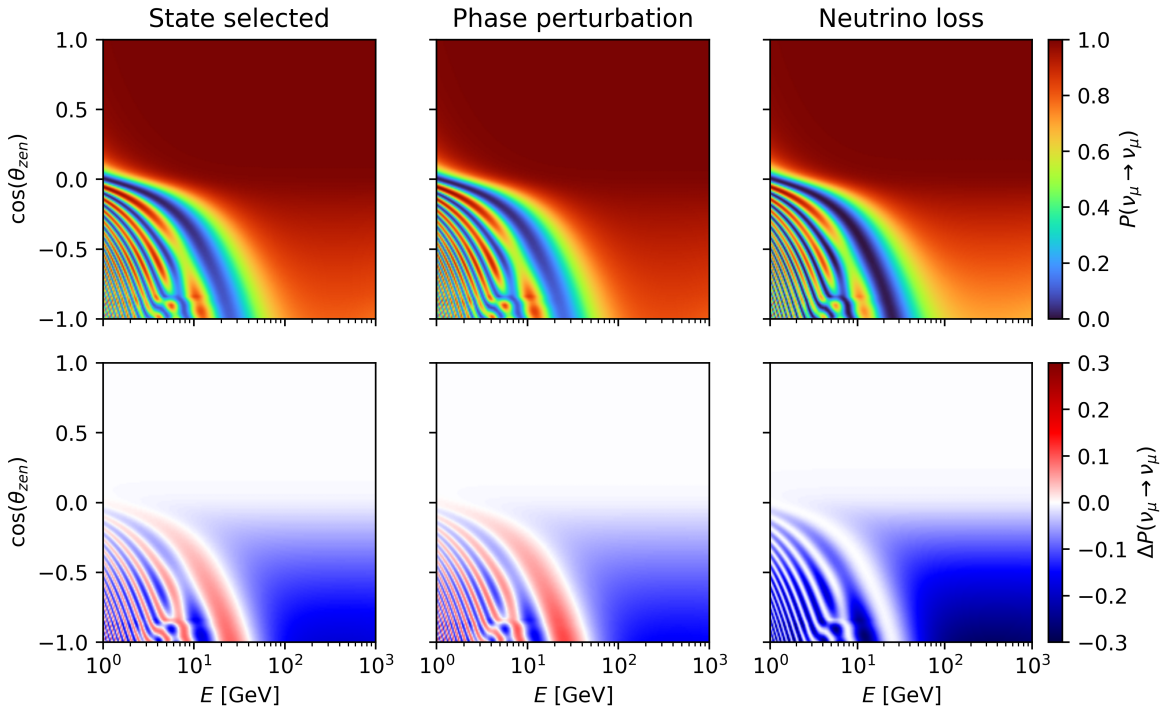

FIGURE A.1: Oscillograms of neutrino oscillations with ν-VBH interactions with $L_{\text{coh}}(25GeV) = 3L_{Earth}$ (same as Section 3.4) and $n = 0$. In the bottom row the results are compared to normal oscillation by taking the difference between the oscillograms in the upper row and the oscillogram shown in Figure 13.

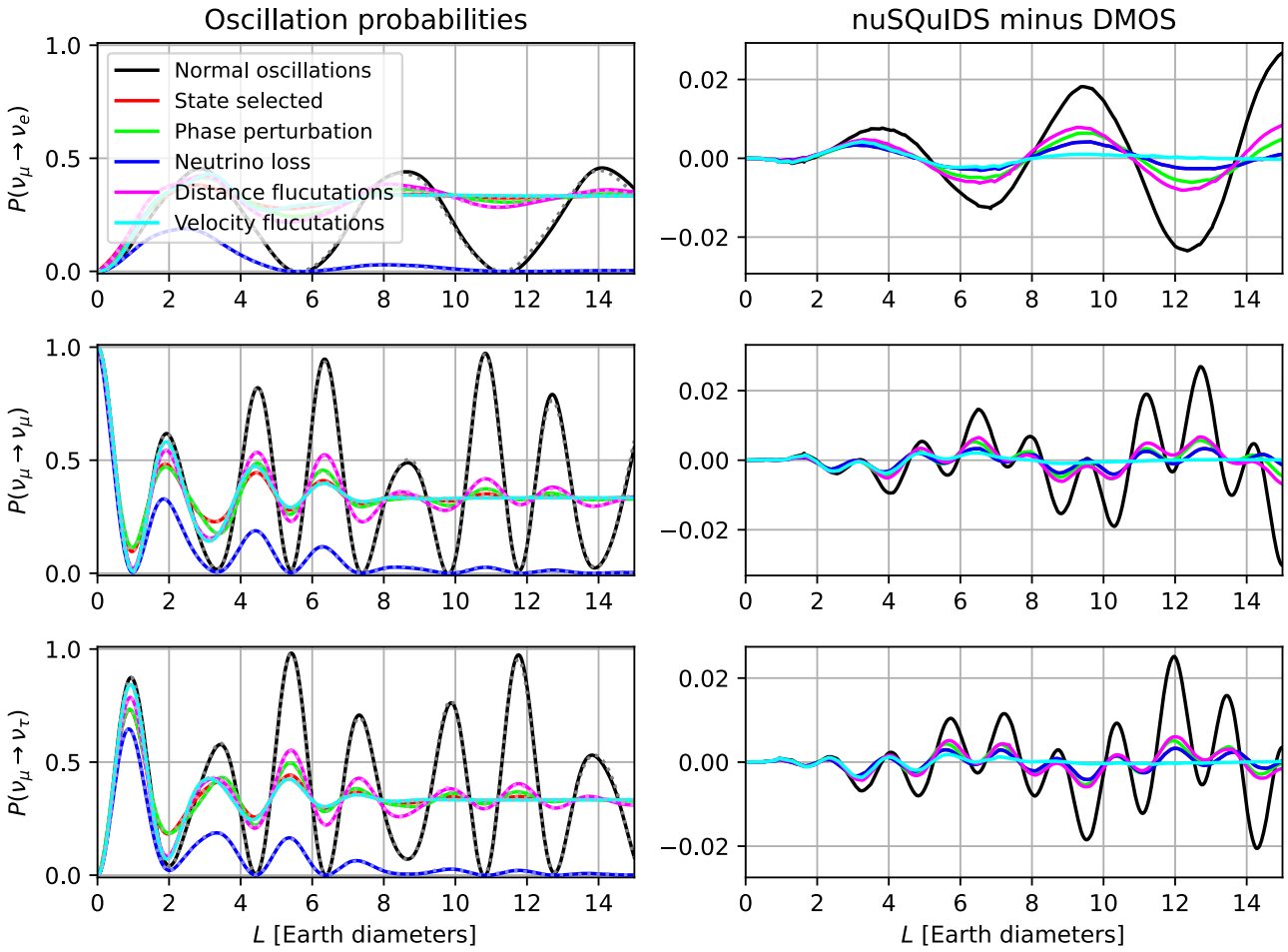

FIGURE A.2: Neutrino oscillation probabilities in constant matter density of 1.5g/cm^3 and an electron fraction of 0.5. These have been calculated by both `nuSQuIDS` (solid lines) and DMOS (dotted lines) for the three ν-VBH scenarios and lightcone fluctuations with $m = 0.5$ (uncorrelated distance) and $m = 1$ (velocity fluctuations). Normal neutrino oscillations are calculated with both methods for reference. In the right column the difference between the respective `nuSQuIDS` and DMOS calculations are shown.

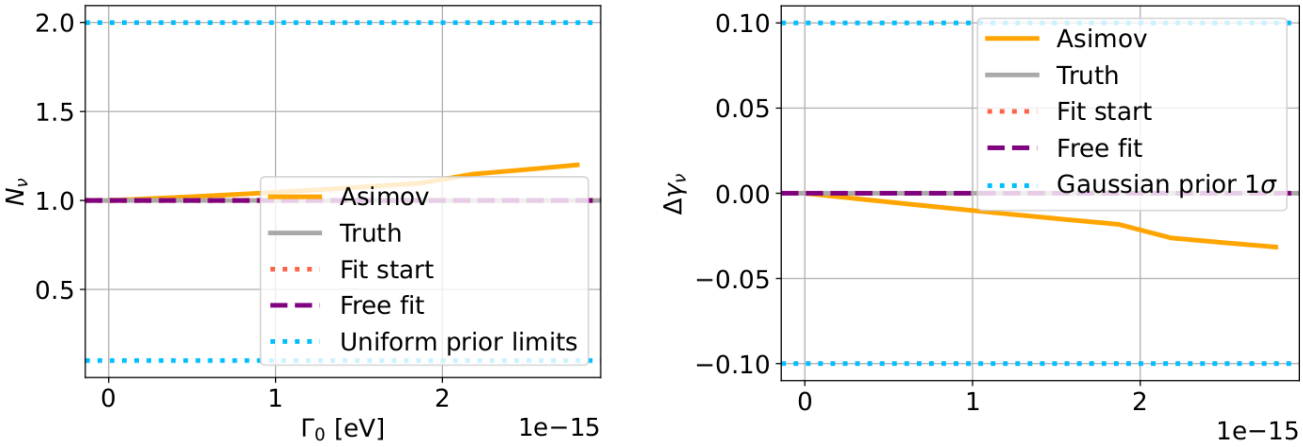

FIGURE A.3: Parameter for the ν-VBH neutrino loss $n = 0$ sensitivity test. The parameters shown are the overall neutrino normalization and the flux spectral index.

B Lightcone fluctuations in matter

One of the most crucial differences between the lightcone fluctuation models and ν-VBH interaction model, is that the is that the decoherence matrices for lightcone flutuation depend on the oscillation wavelengths. We know that the wavelengths of neutrino oscillations depend on matter effects, and thus special treatment is needed for lightcone fluctuations in matter. In this section we explore how this might be taken into account, some issue which arise with it, and why we ultimately have not been able to implement a solution.

B.1 Oscillation wavelengths in matter

The oscillation wavelengths of neutrinos are determined by the differences between the eigenvalues of the Hamiltonian:

$$\lambda_{ij} = \frac{2\pi}{(E_i - E_j)} \tag{49}$$

The vacuum Hamiltonian is diagonal in mass basis, and thus its eigenvalues can be read off from the diagonal. In the highly relativistic limit, these are $E_i = E + \frac{m_i^2}{2E}$, where E is the overall neutrino energy. This gives the vacuum oscillation wavelengths $\lambda_{ij} = 4\pi E/\Delta m_{ij}^2$.

In matter however, determining the wavelengths is not as simple. As stated in Section 2.5, a potential which is diagonal in the flavor basis is added to the Hamiltonian for a neutrino traversing a medium. This means that the full Hamiltonian of the system is neither diagonal in the mass nor flavor basis. In turn, the eigenvalues can not be read off from the diagonal of the Hamiltonian expressed in the mass basis. Instead a different approach needs to be taken.

We know that the Hamiltonian is hermitian, and that for a hermitian matrix a basis always exists in which it is diagonal[4]. Hence, a third basis (in addition to the mass and flavor basis) can be introduced, which diagonalizes the Hamiltonian. We call this the matter basis, which can also be seen as an effective mass basis. The transformation between the flavor and matter basis is then represented by an effective PMNS matrix $\tilde{U}$:

$$H_f = \tilde{U}\tilde{H}_m\tilde{U}^\dagger, \tag{50}$$

where $\tilde{H}_m$ is the Hamiltonian expressed in the effective mass basis. If this basis is found, the effective oscillation parameters can be determined. An exact analytical solution can be derived if neutrino oscillations are simplified to two flavors [31]. Taking this approach, the effective mass splittings can then be expressed:

$$\Delta\tilde{m}^2 = \Delta m^2\sqrt{[\cos(2\theta) - 2EV_{\mathrm{CC}}/\Delta m^2]^2 + \sin^2(2\theta)}, \tag{51}$$

where θ is the mixing angle of the two flavor/mass states. This gives the oscillation wavelengths $\lambda_{ij} = 4\pi E/\Delta\tilde{m}^2$. For three flavors however, this basis is theoretically possible to find analytically [103], but the results are extremely complex and thus not used in

[4]This is the same as saying that the eigenvalues are real.

this project. We instead rely on numerical methods to determine the eigenvalues of the Hamiltonian.

The C++ library which `nuSQuIDS` is built on, GSL, has built-in functions that can treat complex matrices and calculate eigenvalues and eigenvectors of hermitian matrices. These functions have been utilized to determine the eigenvalues of the Hamiltonian, and hence the oscillation wavelengths, of neutrinos in matter. This calculation has to be done for every time step the solver in GSL takes, because the matter density changes as the neutrino propagates through the Earth.

It is important to note the energy-dependence of the damping caused by lightcone fluctuations when matter effects are present. Although the effective mass splitting of Equation 51 is only for two neutrino flavors, it can be used to investigate the rough behavior of the system. This equation shows that the effective mass splittings depend non-trivially on the energy and can both increase and decrease as a function of it. In turn, the oscillation wavelengths do not grow strictly as E^1 as they do in vacuum. The energy-dependence of the damping caused by lightcone fluctuations in matter is thus expected to be different than E^{2n-2}, which is the expectation for vacuum.

B.1.1 Basis of the lightcone fluctuations decoherence matrix

This then leaves us with one more question which needs to be answered; what basis is the lightcone fluctuations decoherence matrix expressed in? Is it in the mass basis, the effective mass basis, or something else? If we look at its shape as expressed in Equation 27:

$$\mathcal{D}_{\text{lightcone}}[\rho] \propto \begin{pmatrix} 0 & \frac{\rho_{21}}{(\eta\lambda_{21})^2} & \frac{\rho_{31}}{(\eta\lambda_{31})^2} \\ \frac{\rho_{21}}{(\eta\lambda_{21})^2} & 0 & \frac{\rho_{32}}{(\eta\lambda_{32})^2} \\ \frac{\rho_{31}}{(\eta\lambda_{31})^2} & \frac{\rho_{32}}{(\eta\lambda_{32})^2} & 0 \end{pmatrix}, \tag{52}$$

we see that this matrix is dependent on the oscillation wavelengths λ_{ij}, and that they are placed on the respective (i, j) entries. This matrix makes sense in the mass basis in vacuum where the Hamiltonian diagonal and λ_{ij} are based on the differences between the i'th and j'th diagonal elements of the Hamiltonian in that basis. I was however concerned that expressing this matrix in the mass basis is wrong when matter effects are present, because the Hamiltonian is then no longer diagonal in this basis. It was unclear to me, if it was true in the effective mass basis instead, or an entirely different approach should be taken.

The easiest way investigate if the decoherence matrix for lightcone fluctuations is correct in matter, is to re-do the simulations in Section 3.4.2 but with matter effects included. To do this the code used for neutrino oscillations was switched out for DMOS, which can calculate neutrino oscillations without decoherence in matter. The simulations can then be checked against the implementations of the open quantum system formulations of lightconefluctuations in DMOS while having matter turned on. The DMOS implementation uses the decoherence matrix for lightcone fluctuations (e.g. Equation 52) in the mass basis. This way we can verify if the formulation is valid in matter.

The specific model I chose to test with this method is the lightcone fluctuation scenario with $m = 0.5$, i.e. uncorrelated distance fluctuations. First, it was verified that performing the simulation in vacuum, the observed damping agrees with the DMOS implementation

lightcone fluctuations (which was already done in [14]). This test is shown in Figure A.4, which shows good agreement between the average of the individual simulated neutrinos and the open quantum system calculation of lightcone fluctuations in DMOS.

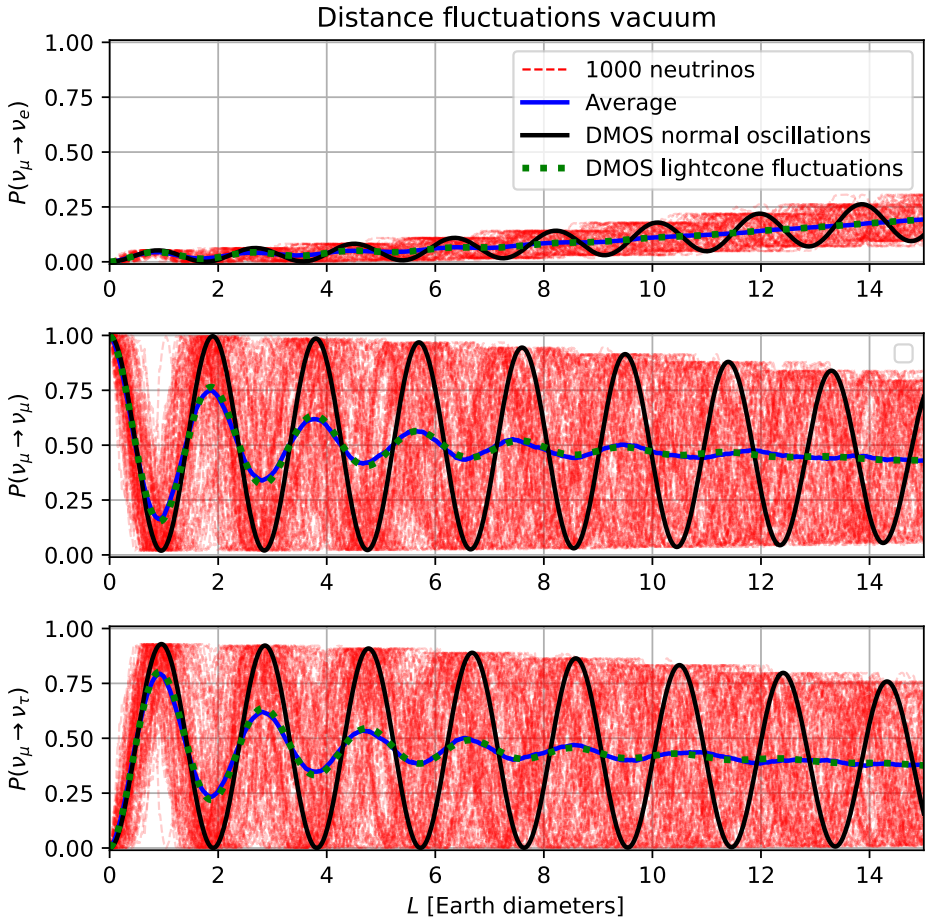

FIGURE A.4: Simulations of neutrino oscillations in vacuum with lightcone fluctuations with $m = 0.5$ (uncorrelated distance fluctuations) for a 25 GeV neutrino starting as a muon neutrino. The normal neutrino oscillations are calculated by DMOS. The average of the individually simulated neutrinos are shown in blue alongside alongside the calculation from the open quantum system formulation of lightcone fluctuations in DMOS.

We then go on to investigate if the simulations and lightcone fluctuations calculation in DMOS still agree when matter effects are turned on. The matter density was arbitrarily set to 1.5 g/cm^3 with an electron fraction of 0.5, and the simulation of 1000 neutrinos was performed. The result is shown in Figure A.5 alongside the DMOS calculation of lightcone fluctuations which does take the modifications to the wavelengths discussed in Section B.

This shows a large disagreement between the average of the individual neutrinos and the DMOS calculation. It indicates that the decoherence matrix for lightcone fluctuations is not correct when matter effects are present. Despite several attempts, we have not been able to find a solution to this problem. It has to be looked into further in the future if

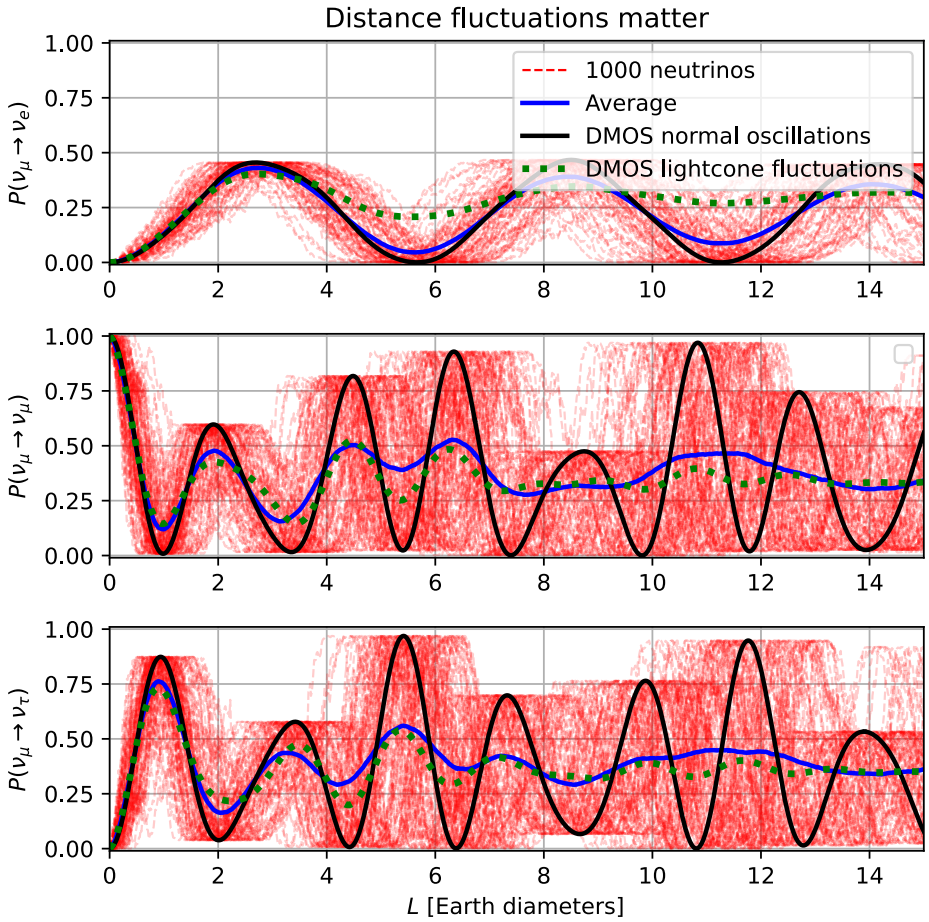

FIGURE A.5: Simulations of neutrino oscillations in vacuum with lightcone fluctuations with $m = 0.5$ (uncorrelated distance fluctuations) for a 25 GeV neutrino starting as a muon neutrino. The mean free path is chosen to be three Earth diameters. This is similar to the simulations carried out in [14]. In beginning of the simulation ($L = 0$), all the 1000 red lines (individual neutrinos) are behind the black line (normal oscillations). The average of the individually simulated neutrinos are shown in blue alongside a simplified version of the damping envelope.

a full statistical analysis is done for this model. To find a solution one would have to go back and see how the decoherence matrix was derived in the first place. This might provide some insight into how matter effects can be taken into account. How we have chosen to proceed with this analysis with lightcone fluctuations only in vacuum.

C Parameter distributions of Γ_0 and δL_0

In section 5.11 we have seen that a correction needs to be applied to the confidence found in the sensitivity tests. The model tested in that section is the ν-VBH interactions state selected model with $n = 2$. To verify the method applied, the ensemble test has been performed for 250 trials of three additional cases: state selected with $n = 0$, neutrino loss with $n = 0$, and lightcone fluctuations with $m = 0.5$ and $n = 2$. The resulting parameter distributions of Γ_0 and δL_0 are shown in Figure A.6 alongside the confidence curves from both the ensemble and sensitivity (corrected) test.

The figure shows good agreement between the corrected confidence of the sensitivity and the ensemble test for the state selected model with $n = 0$ and neutrino loss model with $n = 0$. In these tests the distributions of Γ_0 thus have the same shape as the selected model with $n = 2$ discussed in Section 5.11.1. The distribution of fitted δL_0 values however has a different shape than the physics parameter of the other models. Specifically, there is a gap between the fits which pile up at $\delta L_0 = 0$ and the rest of the distribution. This was discovered very late in the process of writing this thesis, and has thus not been studied in detail. We however know that the difference from the other models is related to that the bin counts depend linearly on Γ_0 and on δL_0^2 when $m = 0.5$. A gap in the parameter value distributions can occur when the derivative of the bin count as a function of the parameter goes from a finite value to zero. This is the case when δL_0 is close to zero and not the case for Γ_0 [5], which can explain why the gap is present only for the former.

By looking at the bottom right plot of Figure A.6, we see if the correction to the confidence can be applied in this case. The plot shows a discrepancy between the corrected confidence from the sensitivity test, which can not be explained by statistical fluctuations. However, the corrected confidence is closer to the ensemble test than if the correction was not applied. Additionally, the corrected confidence from the sensitivity test is on the 'conservative' side of of the ensemble test. This means that a confidence limit will be weaker using the corrected confidence from the sensitivity test, than the more correct confidence which can be obtained from the ensemble test. The estimated sensitivity is thus conservative, which is preferable to the opposite. We have thus chosen to apply the correction to the lightcone fluctuation sensitivities in this analysis.

[5] A similar gap is seen in the distribution of θ_{23} if the true value is close to 45 degrees.

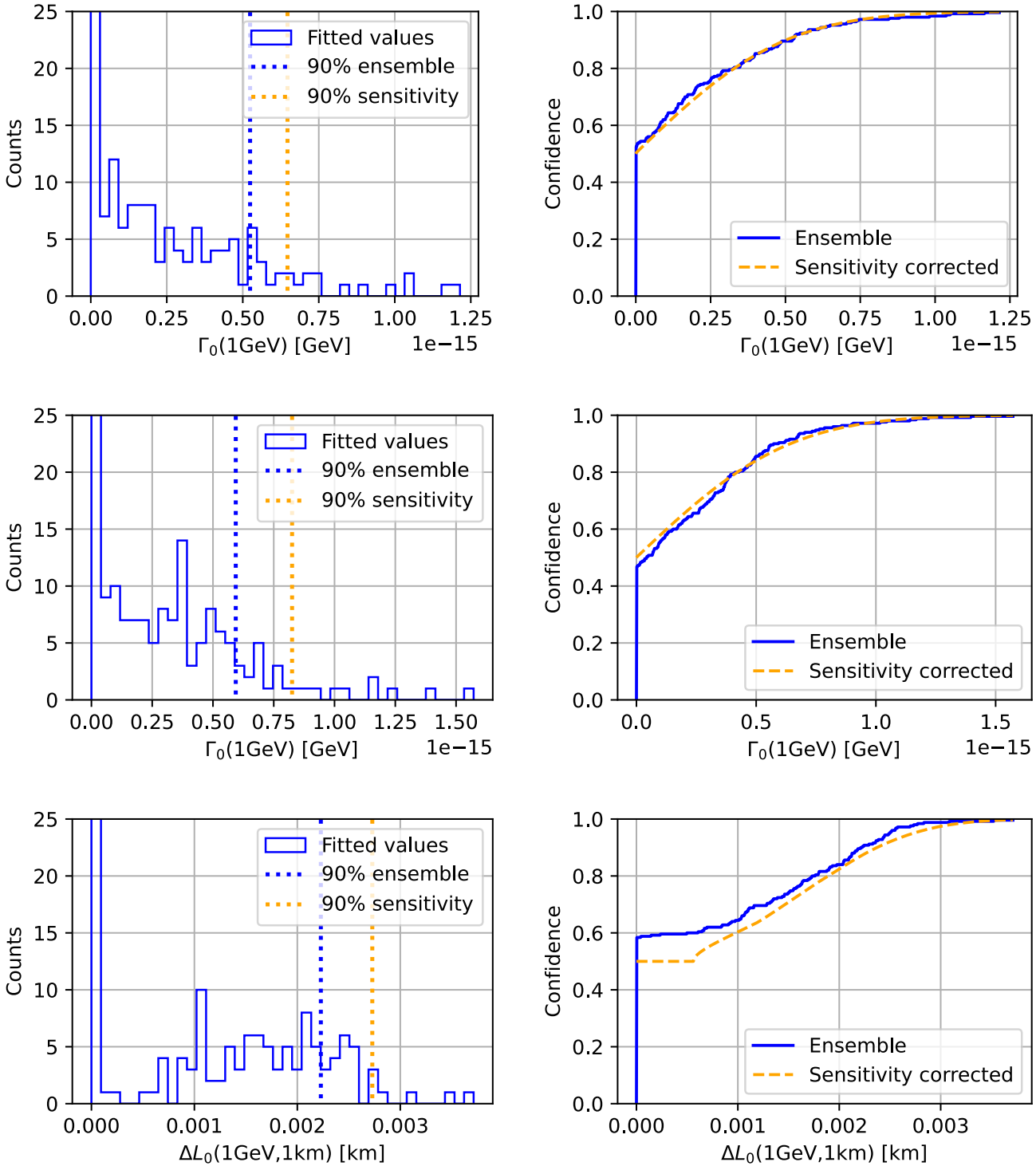

FIGURE A.6: The left column is the parameter distributions from 250 trials of the ensemble test of the models: state selected with $n = 0$ (top row), neutrino loss with $n = 0$ (middle row), and lightcone fluctuations with $m = 0.5$ and $n = 2$ (bottom row). The 90% confidence limits without the correction is shown for both methods as vertical dashed lines. The right column shows the confidence of all values of the physics prameter according to the ensemble test and the sensitivity test with the corrected calculation of the confidence.

D Comparison to models in previous IceCube study

The decoherence matrices of the models tested in [53] study are of the form:

$$\mathcal{D}[\rho] = \left(\frac{E}{E_0}\right)^{n_\gamma} \begin{pmatrix} 0 & \gamma^0_{21}\rho_{21} & \gamma^0_{31}\rho_{31} \\ \gamma^0_{21}\rho_{21} & 0 & \gamma^0_{32}\rho_{32} \\ \gamma^0_{31}\rho_{31} & \gamma^0_{32}\rho_{32} & 0 \end{pmatrix}. \tag{53}$$

Here the subscript of the energy-dependence parameter is included to keep it distinguishable from the model it will be compared to. The considered values of n_γ in the study were -2, -1, 0, 1, and 2. If $\Gamma_{21} = \Gamma_{32} = \Gamma_{31}$ this would be equivalent to the phase perturbation model considered in this thesis. However, to simplify the analysis one of the parameters were set to zero and the other two equal. The decoherence matrices (ignoring energy-dependence) for the three tested scenarios were then:

$$\begin{pmatrix} 0 & \gamma^0\rho_{21} & 0 \\ \gamma^0\rho_{21} & 0 & \gamma^0\rho_{32} \\ 0 & \gamma^0\rho_{32} & 0 \end{pmatrix}, \quad \begin{pmatrix} 0 & \gamma^0\rho_{21} & \gamma^0\rho_{31} \\ \gamma^0\rho_{21} & 0 & 0 \\ \gamma^0\rho_{31} & 0 & 0 \end{pmatrix}, \quad \begin{pmatrix} 0 & 0 & \gamma^0\rho_{31} \\ 0 & 0 & \gamma^0\rho_{32} \\ \gamma^0\rho_{31} & \gamma^0\rho_{32} & 0 \end{pmatrix}. \tag{54}$$

None of these decoherence matrices are directly comparable to the models tested in this project. However, if we look at the decoherence matrix for the lightcone fluctuations case with $m = 0.5$ (derived from Equation 27):

$$\mathcal{D}_{\text{lightcone}}[\rho] = \frac{(\delta L_0)^2}{L_0}\left(\frac{E}{E_0}\right)^{2n_{\text{lightcone}}} \begin{pmatrix} 0 & \frac{\rho_{21}}{(\eta\lambda_{21})^2} & \frac{\rho_{31}}{(\eta\lambda_{31})^2} \\ \frac{\rho_{21}}{(\eta\lambda_{21})^2} & 0 & \frac{\rho_{32}}{(\eta\lambda_{32})^2} \\ \frac{\rho_{31}}{(\eta\lambda_{31})^2} & \frac{\rho_{32}}{(\eta\lambda_{32})^2} & 0 \end{pmatrix}, \tag{55}$$

we see that the entries of the matrix depend on the wavelengths. The oscillation wavelengths in vacuum are $\lambda_{ij} = 4\pi E/\Delta m^2_{ij}$ and the mass splittings from NuFit are $\Delta m_{12} = 7.4 \times 10^{-5}$ eV and $\Delta m^2_{23} \approx \Delta m^2_{13} = 2.53 \times 10^{-3}$ eV. The λ_{21} wavelength is thus a factor of ~ 30 times larger than the other two wavelength, and in turn the corresponding entry of the matrix is suppressed by a factor of ~ 1000. We can thus approximate this entry with 0 and the remaining wavelengths can be assumed $\lambda_{32} = \lambda_{31}$, which reduces the matrix of Equation 55 to the same shape as the third matrix of Equation 54:

$$\mathcal{D}_{\text{lightcone}}[\rho] = \frac{1}{L_0}\left(\frac{\Delta m^2_{23}\delta L_0}{4\pi\eta}\right)^2\left(\frac{E}{E_0}\right)^{2n_{\text{lightcone}}-2} \begin{pmatrix} 0 & 0 & \rho_{31} \\ 0 & 0 & \rho_{32} \\ \rho_{31} & \rho_{32} & 0 \end{pmatrix}, \tag{56}$$

where the wavelength has been inserted. Now the two models are the same except for the energy-dependence. If we however set the values of n_γ and $n_{\text{lightcone}}$ so that the energy-dependencies match, $n_{\text{lightcone}} = (n_\gamma + 2)/2$, the two scenarios become equal with the relation between the fundamental parameters of the models:

$$\delta L_0 = \frac{4\pi\eta}{\Delta m^2_{23}}\sqrt{L_0\gamma^0} \tag{57}$$

It is thus reasonable to compare the bounds of this scenario from [53] with the distance fluctuations case considered in this project. Since the sensitivity of the lightcone fluctuations model was found for integer values of $n_{\text{lightcone}}$, we can compare $n_{\text{lightcone}} = 0$, 1, and 2 to $n_\gamma = -2$, 0, and 2, respectively.

It is however important to note that this comparison can not be made once matter effects have been properly implemented for the lightcone fluctuations case. Matter effects introduce a dependency on the matter density in the decoherence matrix, which is not present in for instance Equation 53. In this case, it might be best to compare the third matrix of Equation 54 to the phase perturbation model. This can be argued for if we assume the sensitivity to the damping of the 21 oscillation is limited, since the θ_{23} mixing angle is small. This has however not been studied in detail.